Topographic coding principles in olfactory systems

Inaugural-Dissertation
to obtain the academic degree
Doctor rerum naturalium (Dr. rer. nat.)

submitted to the Department of Biology, Chemistry and Pharmacy
of Freie Universität Berlin

by
Jan Ansgar Sölter
from Haan, Germany

September, 2014

This dissertation was carried out between October 2009 and August 2014
under the supervision of Dr. Michael Schmuker and Prof. Dr. Martin P. Nawrot
at the group for Theoretical Neuroscience & Neuroinformatics,
Department of Biology, Freie Universität Berlin.

1st Reviewer: Prof. Dr. Martin P. Nawrot - Freie Universität Berlin
2nd Reviewer: Prof. Dr. Giovanni Galizia - Universität Konstanz

Date of defense: 11.05.2015

Acknowledgements

A really big thank you goes to my supervisor Michael Schmuker, who took care of my problems and kept this research on track, but at the same time allowed me the freedom to pursue my own path.
Also a great deal of thanks goes to my collaborators Jan Schumacher and Antonia Strutz who did all the hard work in the wet lab, and constantly provided me with biological support. Of course, this also applies to their supervisors Hartwig Spors and Silke Sachse.
Finally I would like to thank all the Neuroinformatics people of FU Berlin for all the good times we spent together. Especially I would like to thank Martin Nawrot for his intellectual and motivational support, Evren Pamir and Joachim Haenicke for providing valuable feedback all throughout my research and Thomas Rost for a constant insight into state of the art of Kaggle competitions.

Zusammenfassung

Die topographische Repräsentation von Stimulusfeature in sensorischen Arealen ist ein generelles Prinzip neuronaler Codierung. Auch für olfaktorische Systeme gibt es zahlreiche Hinweise auf eine topographische Organisation. Jedoch hat sich bis jetzt noch keine endgültiges Prinzip einer funktionellen Topographie herauskristallisiert.
Die vorliegende Arbeit trägt zu einem erweiterten Verständnis topographischer Prinzipien in olfaktorischen Systemen bei. Zum einen wird in dieser Arbeit die Topographie des ersten olfaktorischen Verschaltungszentrums von Mäusen, des olfaktorischen Bulbus, untersucht, zum anderen jene von einem sekundären olfaktorischen Zentrum in Drosophila, des Lateralen Horns. Dabei stützt diese Arbeit insbesondere die Hypothese, dass räumlich benachbarte rezeptive Felder im olfaktorischen Bulbus eine Überschneidung in ihren Antwortspektren aufweisen. Im Weiteren wird auch gezeigt, dass ein topographisches Auslesen des Antennallobus, des olfaktorischen Verschaltungszentrum in Drosophila, zu lokalen, mit Verhalten assozierten Antwortarealen im Lateralen Horn führt. Insgesamt hebt diese Arbeit die funktionelle Bedeutung einer topographischen Organisation in olfaktorischen Systemen hervor.
Entlang dieser biologischen Fragestellung werden in der vorliegenden Arbeit zwei algorithmische Methoden eingeführt und optimiert. Dies ist zum einen „regularized nonnegative Matrix Factorization“ zur automatischen Extraktion von Antwortregionen in Zeitreihen funktioneller Bildgebung. Und zum anderen sind es Quantitative Struktur-Wirkungs-Beziehungs (QSAR) Modelle, die eine quantitative physikalisch-chemische Beschreibung von olfaktorischen rezeptiven Feldern ermöglichen.

Summary

Topographic representation of stimuli features along the neural sheet is a commonly observed paradigm in sensory coding. Although there is growing evidence of such a topographic arrangement in olfactory systems, no definite functional topographies have yet been established. To this end this thesis contributes towards establishing topographic coding principles in olfactory systems.

This thesis investigates both functional topography in the olfactory relay centre of mice, the olfactory bulb, as well as in a secondary olfactory centre of drosophila, the lateral horn. Thereby it provides additional evidence to the hypothesis that receptive fields in the olfactory bulb are spatially grouped according to their response spectra overlap. Furthermore it shows that a topographic readout of the olfactory relay centre in drosophila, the antennal lobe, yields local response areas in the lateral horn associated with innate valence. All in all this thesis emphasizes the functional role of topography in olfactory systems.

Within this biological question two computational methods are introduced and refined that assist olfactory research. First regularized non-negative matrix factorization is introduced as a tool to automatically disaggregate functional imaging measurements into response domains. And second quantitative structure-activation relationship (QSAR) models are employed to obtain a quantitative physico-chemical description of olfactory receptive fields.

Overview of manuscripts

Chapter 2

Automatic segmentation of odour maps in the mouse olfactory bulb using regularized non-negative matrix factorization

Jan Soelter[1], Jan Schumacher[3], Hartwig Spors[3], Michael Schmuker[1,2]

Status: Published in Neuroimage 2014, Volume 98, pages 279-288
Link: http://dx.doi.org/10.1016/j.neuroimage.2014.04.041

Author contributions:
MS and JS conceived the study, JS developed the rNMF variant and performed data analysis, JSch and HS performed biological measurements. JS and MS wrote the paper.

Chapter 3

Physicochemical vs. Vibrational Descriptors for Prediction of Odor Receptor Responses

Stephan Gabler[1,2], Jan Soelter*[1], Taufia Hussain[4], Silke Sachse[4] and Michael Schmuker[1,2]*

* These authors contributed equally to this work

Status: Published in Molecular Informatics 2013, Volume 32, pages 855-865
Link: http://dx.doi.org/10.1002/minf.201300037

Author contributions:
MS and JS conceived the study, SG and JS performed computational experiments and analyzed data, TH and SS performed biological measurements. JS, SG and MS wrote the paper. In particular JS performed data analysis with regard to Fig. 2c&d, Fig. 5-7 and supplemental figures S1, S3-S8.

Chapter 4

Profiling the role of receptor MOR18-2 in the olfactory code

Jan Soelter[1], Jan Schumacher[2], Hartwig Spors[2], Michael Schmuker[1,2]

Status: To be submitted to a peer reviewed journal

Author contributions:
MS, HS and JS conceived the study, JS performed data analysis, JSch and HS performed biological measurements. JS wrote the paper.

Chapter 5

Decoding Odor Attraction and Intensity in the Drosophila brain

Antonia Strutz[4], Jan Soelter[1] , Amelie Baschwitz[4], Abu Farhan[4], Veit Grabe[4], Jürgen Rybak[4,] Markus Knaden[4], Michael Schmuker[1,2], Bill S. Hansson[4] & Silke Sachse[4]

Status: Revised manuscript published at eLife 2014, Volume 3
Link: http://dx.doi.org/10.7554/eLife.04147

Author Contributions:
AS and SS together conceived the study. AS planned all experiments, carried out functional imaging of iPNs, generated transgenic fly line and performed immunohistochemistry with help of JR and AB. VG performed functional imaging of OSNs and analyzed glomerular innervation patterns. AB performed PA-GFP experiments and neuronal reconstructions of iPNs. AF performed behavioral experiments. JS analyzed the imaging data using rNMF. MK supervised AF and MS supervised JS. BSH provided intellectual and financial support. AS and SS interpreted the results, prepared the figures and wrote the paper.
In particular JS performed data analysis with regard to Fig. 3e&f, Fig. 5d and Fig.7.

Author affiliations:
1 Theoretical Neuroscience, Institute of Biology, Dept. of Biology, Freie Universität Berlin
2 Bernstein Center for Computational Neuroscience Berlin
3 MPI for Biophysics, Frankfurt am Main
4 Department of Evolutionary Neuroethology , MPI for Chemical Ecology , Jena

Contents

4 Profiling the role of receptor MOR18-2 in the olfactory code

5 Decoding Odor Attraction and Intensity in the Drosophila brain

6 General discussion

Introduction

1.1 Neural maps in sensory coding

Sensory systems serve organisms to link themselves with their environment. They create sensations of relevant environmental stimuli which form the basis of behavioural decisions and/or higher cognitive processes. Ultimately sensory systems provide an organism with an efficient sensation that facilitates adaptation to the environment.

Therefore in studying a sensory system two major questions arise: Which are the relevant stimuli encoded and how does this encoding facilitate neuronal processing? For many organisms and sensory systems the receptive fields of individual neurons have been extensively characterized. Furthermore the subsequent emergence of receptive fields of upstream neurons, that is the subsequent extraction of more and more complex stimulus features, has been elucidated.

For example a well studied sensory system is the mammalian visual system [Hoffman and Wehrhan, 2001]. Mammals sense light stimuli with photoreceptor cells whose receptive fields are characterized by wavelength and visual field position of the light source. Intrinsically, by the eye's physical design, neighbouring photoreceptors in the retina are activated by neighbouring points in the visual field. Based on this topography, retinal ganglion cells (RGCs) provide a contrast enhanced read-out as they are excited by their corresponding central receptors and laterally inhibited from surrounding receptors [Kuffler et al., 1953]. A second population of RGCs provides an inverse read-out by central inhibition and surround excitation. These two instances of the visual field map (retinotopic map) are relayed onwards to the corpus geniculatum laterale. A local topographic read-out of those two maps then results in orientation sensitive receptive fields of neurons in visual cortex V1 [Jin et al., 2011], which are arranged in pinwheels according to their orientation preference. A subsequent local topographic read-out of V1 by neurons of visual cortex V4 [Motter, 2009] then facilitates the emergence of curvature sensitive receptive fields [Carlson et al., 2011; David et al., 2006].

In general the visual system provides numerous examples of neural maps which are arranged according to stimulus properties. In many cases they are converted to higher order receptive fields by topographic read-outs [Nauhaus and Nielsen, 2014]. Such topographic maps are not only observed in visual but also in many other sensory systems [Fitzpatrick and Ulanovsky, 2014]. Amongst others this includes tonotopic maps of frequency sensitivity in auditory sys-

tems [Ehret, 2001], somatotopic maps of body position in somatosensory systems [Vanderhaeghen et al., 2000] or gustotopic maps of taste quality of gustatory systems [Chen et al., 2011]. Therefore feature maps seem to be a fundamental principle of sensory neural coding although some consider them little more than epiphenomena of neural development [Fitzpatrick and Ulanovsky, 2014].

For olfactory systems the current knowledge of neural feature maps is still very basic. To a large extend this is because already our knowledge about receptive fields of olfactory sensory neurons (OSNs) is still very incomplete [Peterlin et al., 2014]. For this reason I elaborate on those two topics in this thesis. First this chapter provides an introduction of the current knowledge about topography in the olfactory systems. Then Chapter 2 and 3 introduce two methods for enhancing the capability to determine olfactory receptive fields. Utilizing these methods chapter 4 elaborates on principles of topographic organization at the relay center of olfactory information. Chapter 5 provides an example for the emergence of subsequent receptive fields by topographic read-out of an upstream olfactory map. And finally chapter 6 summarizes and discusses the findings of neural feature maps in olfaction.

This thesis resorts to two extensively studied animal models: the common fruit fly, *Drosophila melanogaster*, and the house mouse, *Mus musculus*. Both species provide the advantage that there is a large array of genetic tools available to visualize and manipulate neural activity [Zhang et al., 2007; Hadjantonakis et al., 2003; Keene and Waddell, 2007]. Furthermore both species exhibit both innate [Mandiyan et al., 2005; Semmelhack and Wang, 2009] and learned behaviour [Abraham et al., 2004; Quinn et al., 1974] to odour stimuli. Thus both are suitable to study the neural substrates of these phenomena. Due to a considerably lower complexity it is more tractable to follow chemosensory information processing in the *Drosophila* brain. Conversely the mouse brain is suitable for studying the neural adjustments responsible for a larger behavioural repertoire and extended abilities of learning.

1.2 The olfactory system of *Drosophila*

Drosophila heavily relies on chemosensation in its behaviour. Chemosensation helps to locate and identify food and to asses its quality and nutritious value. Furthermore it triggers avoidance of toxins and pathogens and governs courtship, aggression and oviposition. To this end *Drosophila* possesses an olfactory system to detect airborne chemicals together with a gustatory system for contact chemosensation. The next sections will introduce the neuroanatomy and functional organization of the olfactory system with a special emphasize on its topographical layout.

1.2.1 Neuroanatomy

Olfactory sensing

In *Drosophila* airborne chemosensation is performed by two different classes of receptors: odorant receptors (ORs) and ionotropic receptors (IRs).Usually an olfactory sensory neuron (OSN)

expresses one of these receptors together with a co-receptor, but a few receptors are co-expressed in designated pairs or triples [Vosshall and Stocker, 2007; Rytz et al., 2013]. As a result there are ≈ 50 distinct OSN types, defined by their receptor composition.

Most OSNs are housed in specialized hairs, called sensilla. Based on their morphology the sensilla can be grouped into three categories (basiconic, coeloconic, trichoid) [Shanbhag et al., 1999], with the basiconic sensilla being further subdivided into large anntenal, small anntenal and palp basiconic sensilla. Each category of sensilla is located at distinct but strongly overlapping zones on the antennae, except the palp basiconic sensilla which are, as their name implies, located at the maxillary palps. Each sensillum houses one to four OSNs in fixed combinations, such that sensilla can be categorized into 21 groups based on their specific OSN composition: 10 antenna basonic OSNs (ab1-ab10), 3 palp basonic OSNs (pb1-pb3), 4 antenna trichoid OSNs (at1-at4) and 4 antenna coeloconic OSNs (ac1-ac4) [Couto et al., 2005]. The ac sensilla are predominantly occupied by OSNs containing IRs [Rytz et al., 2013] whereas the OSNs of the remaining sensilla express almost only ORs [Vosshall and Stocker, 2007]. Besides this differentiation there is no further relationship between genetic OR similarity and sensillum category or group [Couto et al., 2005].

Finally there is a last type of OSNs (expressing IR64a) which is not housed in sensilla, but located on the sacculus, a special structure atop the antenna [Rytz et al., 2013].

Olfactory relay

The basic perception of the sensory neurons is collected, modulated and redistributed in the antennal lobes (AL). The ALs are spherical structures filled with distinct spherical neuropil, called glomeruli.

In the AL all of the OSNs of each type converge into a single glomerulus. Conversely each glomerulus is only innervated by one type of OSNs [Martin et al., 2013]. Therefore there are in total ≈ 50 glomeruli which are stereotypically placed across animals.

In this general topographic arrangement glomeruli are clustered according to their sensilla type: ab-type-glomeruli at the medial region, at-type glomeruli at the lateral anterior region, pb-type glomeruli at the central-medial region, and ac-type glomeruli at the posterior region [Couto et al., 2005]. Notably, while ac-type IR-expressing coeloconic OSNs and OR-expressing basiconic and trichoid OSNs are intermingled in the antenna, their corresponding glomeruli are fully spatial segregated [Rytz et al., 2013]. Furthermore, within the basiconic domain the glomerular arrangement reflects genetic sequence distance. The smaller the sequence divergence between the corresponding receptors the more likely the glomeruli are located close to each other [Couto et al., 2005].

Olfactory projections

From the AL projection neurons (PNs) project the olfactory sensation further on to the mushroom body calyx (MBc), the lateral horn (LH) and to a minor extend to other higher brain areas like the ring neuropil, the posterior lateral protocerebum (plP) and the ventro lateral

protocerebum (vlP) [Tanaka et al., 2012b]. The majority of these projections occur within three different tracts [Stocker et al., 1990; Tanaka et al., 2012a]: (1) Via the medial antennal lobe tract (mALT; formerly inner antennocerebral tract, iACT) excitatory PNs project first to the MBc and then further to the LH. (2) Via the medial lateral antennal lobe tract (mlALT; formerly middle antennocerebral tract, mACT) inhibitory PNs project to the LH. (3) Via the lateral antennal lobe tract (lALT; formerly outer antennocerebral tract, oACT) excitatory PNs project first to the LH and then to the MBc.

The PNs of the mALT are mostly uniglomerular, i.e. they arborize into a single glomerulus, whereas the dendrites of mlALT and lALT PNs arborize into multiple glomeruli. This involves both arborizations into local areas of the AL as well as panglomerular arborizations that span the entire AL [Tanaka et al., 2012a].

Both uniglomerular mALT-PNs as well as multiglomerular mlALT-PNs transfer en gross the topography of the AL to the LH. PNs originating from the medial glomeruli tend to terminate in the dorsal LH, whereas those from the dorsolateral glomeruli mostly innervate the ventral LH. The same topographic transformation of the AL's medial-dorsolateral axis to a dorsal-ventral axis is also observed in the projection pattern of the uniglomerular mALT PNs in the MBc [Tanaka et al., 2012a]. Given the topographic organization of the AL according to sensilla types this directly induces also a rough compartmentalization of LH and MBc according to sensilla types [Jefferis et al., 2007].

Interestingly although the AL topography is roughly kept by second order neurons that project to both higher olfactory centres, it only persists in third order neurons of the LH [Fişek and Wilson, 2013] whereas third order neurons of the MBc seem to establish synaptic connections ignoring this topography [Caron et al., 2013].

Olfactory modulation

In the AL olfactory information is not only relayed further on, but also modulated laterally by local interneurons and via centrifugal feedback neurons from various brain regions [Tanaka et al., 2012b].

The AL interneurons display a large diversity in terms of electrophysiolgical, morphological and neurochemical characteristics, though their main effect is inhibitory [Wilson, 2013]. In general there is no topographic restriction of lateral modulation as most interneurons exhibit panglomerular innervations patterns across the whole AL. Nevertheless some interneurons show locally confined multiglomerular innervations [Chou et al., 2010].

Also the innervation patterns of centrifugal neurons are mostly panglomerular [Tanaka et al., 2012b; Hu et al., 2010], indicating rather a global feedback modulation than a local refinement.

Synopsis

The AL is a topographic sensory array in the sense that it allocates the activation of olfactory receptors on a stereotypic map. Its glomerular arrangement reflects en gross the peripheral

arrangement of receptors. In addition the layout adheres even more strongly to the genetic distance of the corresponding receptors than to the arrangement of OSNs at the periphery.

There is no clear anatomical evidence that this topography governs modulations within the AL, but the feed-forward projections, especially those to the LH, conserve the AL topography. That is, the topography of the AL also governs local circuits in higher olfactory centres.

1.2.2 Functional organization

Olfactory pathway

In a simple functional view of the olfactory pathway, the AL provides a preprocessed olfactory sensation which both facilitates olfactory learning in the mushroom body calyx [Heisenberg et al., 1985] and builds a substrate for innate behaviours in the lateral horn [Heimbeck et al., 2001].

Thereby the preprocessing of the AL includes an enhancement of the signal-to-noise ratio and therefore an increased dynamic range of the odour sensation. This is mainly achieved by the strong convergence of OSNs to PNs at the glomeruli [Wilson, 2013]. Additionally the inhibitory lateral network provides a gain control mechanism to adjusts glomerular sensitivity to the global input level, such that odour representations become more concentration invariant [Olsen et al., 2010].

Antennal lobe

As the AL provides topographic input into higher olfactory centres the receptive fields of individual glomeruli and their spatial relations are of special interest, yet not fully deciphered. The available information on glomerular input, i.e. OSN odour activations, ranges from only a handful to about two hundred measured molecules [Galizia et al., 2010]. Some of the OSNs are sharply tuned to pheromones or relevant ecological signals [Ruta et al., 2010; Stensmyr et al., 2012] whereas most are broadly tuned to diverse odours with different chemical groups [Hallem and Carlson, 2006]. Notably most odours are not only encoded by a single glomerulus, but each odour activates a specific combination of glomeruli. As a result the receptive fields of glomeruli are strongly overlapping.

With a fragmentary knowledge of the receptive fields of individual glomeruli there comes an uncertainty about the functional relation between proximal glomeruli. Nonetheless some weak trends have been observed: (1) broadly tuned glomeruli are located rather dorso-medial [Fishilevich and Vosshall, 2005], (2) glomeruli tuned to aromatic molecules cluster in the central-ventral region, (3) chain-length preference of glomeruli increases along the posterior-anterior axis [Couto et al., 2005] and (4) there is a weak tendency of glomeruli with correlated receptive fields to lie spatially close to one another [Galizia et al., 2010].

Lateral horn

Whereas there is no clear functional compartmentalization of the AL, in the LH a subdivision into a posterior-dorsal fruit odour region and an anterior-ventral mating odour region has been observed [Jefferis et al., 2007; Grosjean et al., 2011]. Additionally an anterior-medial region of acidity responsiveness also has been described [Min et al., 2013].

1.3 The olfactory system of mice

Similar to flies, chemosensation in mice provides means to locate and identify food and to asses its quality and nutritious value. It also triggers avoidance of toxins, pathogens and predators and governs intra species communication. But compared to flies chemosensation in mice has to provide extended functionality. First, as mice are omnivores, the range of possible food sources to be evaluated is both larger and more diverse. Second, social interaction of mice is much more versatile than in flies. It involves a considerably lager array of specific pheromones. But it also includes the social transmittance of hedonic values for odours, such as socially transmitted food preferences [Arakawa et al., 2013].

To fulfil those demands mice posses an array of chemosensory systems. That involves for one a gustatory system that detects five qualities of taste: umami, sweetness, bitterness, sourness and saltiness [Chandrashekar et al., 2006]. Second there is the trigeminal system, which exhibits chemosensitivity besides its responsiveness to thermal and mechanical stimuli. It innervates most of the face including the nasal cavities and is mainly triggering protective reflexes in response to irritating chemical vapors [Keverne et al., 1986; Tizzano and Finger, 2013]. Third there are four olfactory subsystems originating at distinct locations in the nose (see also Fig. 1.1): the Main Olfactory Epithelium (MOE), the Vomeronasal Organ (VNO), the Gruenberg Ganglion (GG) and the Septal Organ of Masera (SO). The following sections will give a description of their neuroanatomy and function.

1.3.1 Neuroanatomy

Olfactory sensing

In all subsystems sensory neurons detect olfactory stimuli by means of chemical receptors. These comprise of five multigene families of G-protein coupled receptors (GPCRs): canonical olfactory receptors (ORs), vomeronasal receptors type 1 and 2 (V1Rs, V2Rs), trace amine-associated receptors (TAARs) [Nei et al., 2008] and formyl peptide receptors (FPRs) [Liberles et al., 2009; Rivière et al., 2009]. The largest of those families, canonical ORs, are commonly sub-grouped into class 1 ORs ('fish type') and class 2 ORs ('terrestrial type') [Glusman et al., 2000]. Furthermore some sensory neurons express receptor guanylyl cyclase type D (GC-D) and type G (GC-G) [Yu et al., 1997; Fleischer et al., 2009], but it is unclear if they act as receptors or are modulated by an unidentified GPCR activation [Munger et al., 2009].

For most sensory neurons it holds the one neuron - one receptor rule: Each neuron only

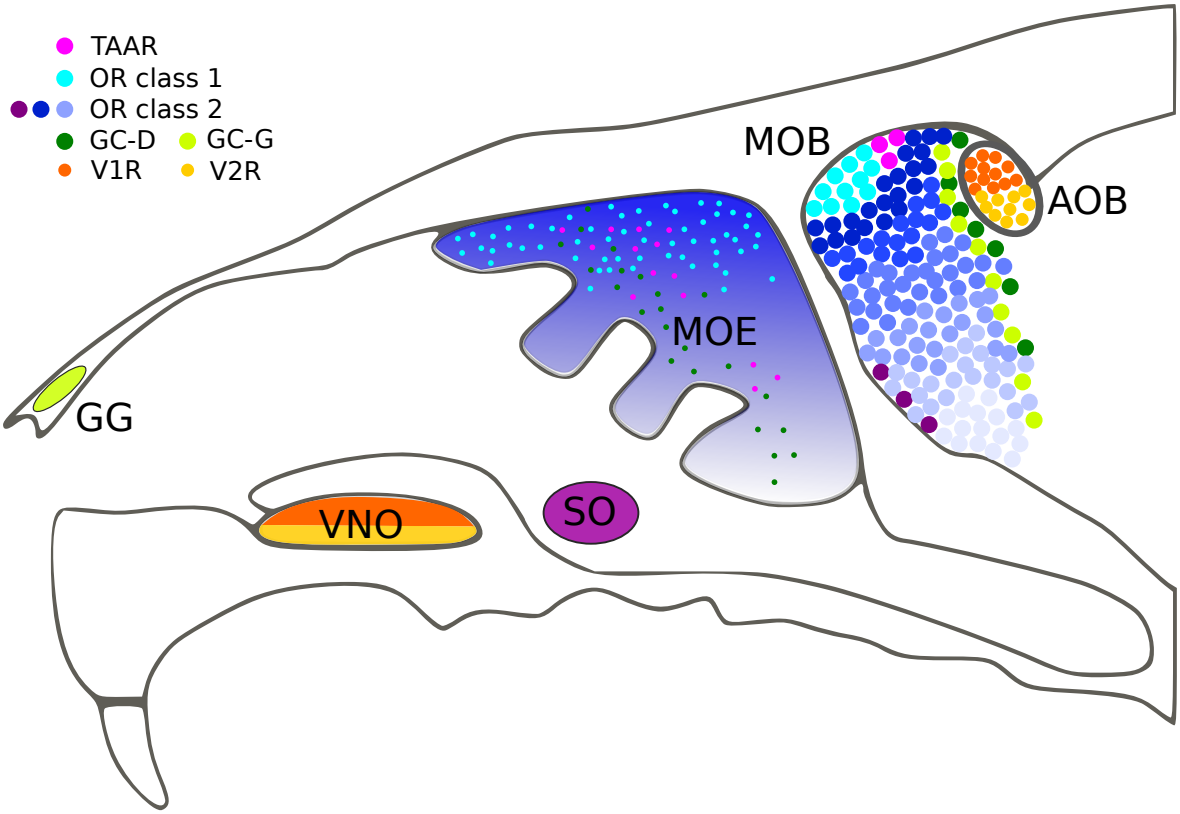

Figure 1.1: **Location of the different olfactory organs and receptor types in mice.** For abbreviations see text. Figure adapted from [Matsuo et al., 2012; Tirindelli et al., 2009; Brennan and Zufall, 2006]

expresses a single receptor gene. Most prominently this rule is violated by the V2R receptors which are mainly co-expressed.

In general sensory neurons expressing a specific type of receptor are restricted to certain subsystems (see Fig. 1.1). In the MOE ORs, Taars and GC-D are expressed, in the Vomeronasal Organ VRs and FPRs, in the Septal Organ of Masera a small subset of class 2 ORs and in the Gruenberg Ganglion V2R83, Taars and GC-G receptors [Munger et al., 2009; Liberles, 2013].

Typically within a subsystem sensory neurons expressing different receptor genes are intermingled. This holds both for OSNs expressing receptors of the same as well as of different gene families. Nonetheless also within subsystems, receptor expression is still structured. Expression of individual receptors in the MOE is restricted to distinct but highly overlapping zones along the dorsomedial-ventrolateral axis [Miyamichi et al., 2005]. Furthermore the VNO is subdivided into a basal and an apical region with expression of V2Rs in the first and V1Rs as well as most of the FPRs in the latter [Dulac and Torello, 2003; Dietschi et al., 2013].

Olfactory allocation

Analogue to the antennal lobes in *Drosophila*, in mice the basic sensation of the sensory neurons is collected and redistributed in the olfactory bulbs.

The sensory neurons of the MOE, SO and GG project to the Main Olfactory Bulb (MOB) whereas VNO neurons project to the adjacent Accessory Olfactory Bulb (AOB). Exactly as in the AL, sensory neurons of specific receptor types converge into distinct glomeruli, which are exclusively innervated by those type of OSNs. But in contrast to the AL each type of OSNs forms not only one but a few glomeruli in each ipsilateral bulb (mostly 2-4 in the MOB and 6-20 in the AOB) [Del Punta et al., 2002; Mombaerts et al., 1996; Wagner et al., 2006].

The arrangement of the glomeruli in the bulbs reflects the compartmentalisation of the olfactory subsystem in the nose and even renders it more pronounced: The basal and apical domains of the VNO are transferred to a posterior and anterior domain in the AOB [Dietschi et al., 2013]. The dorsomedial-ventrolateral axis of OE receptor expression is conveyed to a dorso-ventral arrangement of glomeruli in the MOB [Miyamichi et al., 2005]. Moreover glomeruli of class 1 OR, class 2 OR and Taar neurons occupy mostly separated domains in the MOB [Johnson et al., 2012; Pacifico et al., 2012] with the domains of class 1 ORs and Taars located in the dorsal part. The class 2 OR expressing neurons of the SO also project to the class 2 domain in the MOB, both as separate glomeruli and as additional input to MOE glomeruli [Breer et al., 2006]. Finally GC-D expressing neurons of the MOE and GC-G expressing neurons of the GG both project to distinct populations of so called 'necklace' glomeruli at the border of AOB and MOB [Matsuo et al., 2012; Munger et al., 2010].

In addition to the domain organization according to receptor family, the arrangement of glomeruli within MOB domains also follows a stereotypic layout across animals [Belluscio and Katz, 2001; Soucy et al., 2009]. Interestingly this layout appears twice in each MOB with a medial-lateral mirror symmetry [Lodovichi et al., 2003]. Thereby in general glomeruli of homologoues ORs map to similar positions [Tsuboi et al., 2011; Strotmann et al., 2000], although there are exceptions to this principle [Zhang et al., 2012]. Similarly in the anterior domain of the AOB the glomeruli are topographically arranged according to clades of the V1R gene family [Wagner et al., 2006].

All in all the AOB and MOB embody a stereotypic topographic representation of the olfactory perception. These precise layouts are obtained during ontogenesis by exploiting both genetic identity as well as correlated neural activity of OSNs [Mori and Sakano, 2011; Bozza et al., 2009; Yu et al., 2004; Zheng et al., 2000; Zou et al., 2004; Serizawa et al., 2006].

Olfactory projections

The sensory array of the MOB and AOB is projected further downstream by mitral and tufted (M/T) cells. M/T cells of the AOB target areas of the limbic system (especially the medial amygdala) whereas those of the MOB project mainly to areas of the paleocortical olfactory cortex (i.e. anterior olfactory nucleus (AON), piriform cortex (PC), entorhinal cortex , olfactory tubercule and lateral amygdala) [Dulac and Wagner, 2006].

Although there is not yet a complete picture of the topographical layout of these projections, two different patterns became apparent: For one topography of the MOB is kept en gros in the AON [Miyamichi et al., 2011] and especially in the AON pars externa [Yan et al., 2008] as well

as in the anterior and posterolateral cortical amygdala [Sosulski et al., 2011]. Thereby input to the amygdala stems merely from the dorsal MOB [Miyamichi et al., 2011]. On the other hand projections to the PC are distributed across its entire sheet without any regard to the topographic origin in the MOB [Miyamichi et al., 2011; Davison and Ehlers, 2011; Sosulski et al., 2011]. That is both a topographic and a scattered readout of the bulbs is prevalent.

M/T cells of the AOB cells integrate the excitatory signals of different glomeruli [Del Punta et al., 2002; Wagner et al., 2006], whereas M/T cells of the MOB convey mainly the excitatory input of a single glomerulus [Dhawale et al., 2010]. Nonetheless the few dozen M/T cells that receive input of the same glomerulus (called sister cells) show diverging response profiles on account of different modulations. These modulations are gradually dependent on the location of the M/T cell bodies due to the specific targeting of the lateral interneuron network [Kikuta et al., 2013]. The next section will give a brief introduction to this network.

Olfactory modulation

In the olfactory bulbs information is not only relayed forward, but also shaped by modulation. This modulation is mediated by a variety of interneurons at different layers of the olfactory bulb [Parrish-Aungst et al., 2007]. In spite of the immense complexity of this circuitry, some basic mechanism have been revealed.

At the glomerular layer inhibitory periglomerular (PG) cells and excitatory external tufted (ET) cells provide an intra-glomerular signal relay [Gire et al., 2012] and gain control [Murphy et al., 2005]. In addition excitatory [Aungst et al., 2003] and inhibitory [Whitesell et al., 2013] short axon (SA) cells mediate inter-glomerular interaction in a range of about 600µm ($\sim$ 9 glomeruli). Despite SA cells being partly excitatory their main effect on M/T cells is still inhibitory as excitatory SA primarily synapse to inhibitory PG cells.

At the next stage, the external plexiform layer (EPL), M/T cells exhibit strong dendritic arborizations which are exposed to dendro-dendritic inhibition. For one thing parvalbumin-expressing (PV) cells mediate areal inhibition in a range of $200 - 300$µm ($\sim$ 4 glomeruli) [Kato et al., 2013; Miyamichi et al., 2013]. For another thing granule cells of the granule cell layer provide next neighbour inhibition at a scope of about 100µm ($\sim$ 1 glomeruli) [Egger and Urban, 2006; Miyamichi et al., 2013].

Additionally the glomerular layer and the granule cell network are also targets of excitatory cortical feedback projections from the AON [Markopoulos et al., 2012] and the PC [Boyd et al., 2012]. As the centrifugal feedback mainly targets the lateral networks it effects the bulbs on the same length scales [Cazakoff et al., 2014].

In contrast to this local modulation, the olfactory bulbs are also subject to global centrifugal neuromodulatory input including noradrenealine, serotonin and acetylcholine releasing fibres [Matsutani and Yamamoto, 2008]. The release of these neuromodulators takes place all along the fibres such that they simultaneously effect wide areas within the bulb.

Synopsis

Analogue to the antennal lobe the olfactory bulbs are a sensory array which allocates the olfactory sensation on a stereotypic topographic map. Its arrangement reflects to a great extent genetic identities of the OSNs.

Thereby the topographic layout builds a substrate for local circuits of lateral and centrifugal integration of information at different length scales. Furthermore the topography of the MOB is transferred en gross in projections to the AON and the cortical amygdala, whereas it is lost in the projections to the piriform cortex.

1.3.2 Functional Organization

Olfactory Subsystems

For most of the olfactory subsystems major functional roles have been identified. The VNO in general is strongly involved in innate social behaviours [Chamero et al., 2012; Stowers et al., 2013; Sokolowski and Corbin, 2012] detecting a large number of con- and heterospecific cues as for example steroids (V1Rs), peptides and major urinary proteins (V2Rs) [Isogai et al., 2011; Chamero et al., 2011]. The importance of the VNO in eliciting innate behaviours is emphasized by its direct projections to the limbic system [Keverne, 1999]. Also for the Gruenberg Ganglion (i.e the necklace glomeruli) there is growing evidence that it is crucially involved in innate responses to alarm pheromones and kairomones containing heterocyclic sulphur or nitrogen containing compounds generated by meat digestion [Brechbühl et al., 2008, 2013].

No specific functionality of the SO has been discovered yet, but due to its location at the sopalatine duct, which connects the mouth with the nasal cavity, it is hypothesised to be involved in detection of non-volatile food components [Breer et al., 2006].

The MOE is believed to accomplish general odour detection and thus provide means for associative learning especially in the PC [Su et al., 2009]. Nonetheless there is also some evidence that the MOE takes an essential part in mediating different innate behaviours [Stowers and Logan, 2010]. For example the TAAR domain is involved in mediating both aversive [Dewan et al., 2013] and attractive [Li et al., 2013] behavioural responses. However it still has to be elucidated if this reflects rather true innate or (neonatally) socially learned olfactory behaviour [Stensmyr and Maderspacher, 2013; Sanchez-Andrade and Kendrick, 2009]. For instance the GC-D expressing neurons, associated with the necklace glomeruli, detect odors like carbon disufide and uroguanylin and seem to be crucially involved in learning socially transmitted food preferences [Munger et al., 2010; Arakawa et al., 2013].

Olfactory Bulb

Even worse than for *Drosophila* for most glomeruli in mice no activating molecules are known [Peterlin et al., 2014]. Nevertheless a general assessment of OSN responses has shown that both broadly and narrowly tuned OSN types exist, with many of them not being restricted to odours

of a specific functional group [Nara et al., 2011]. Thereby, just like in *Drosophila*, most odours activate a combination of multiple types of OSNs (i.e. glomeruli) [Malnic et al., 1999].

The lack of knowledge about individual receptive fields of glomeruli renders it difficult to investigate their functional arrangement. On the one hand there is evidence that nearby gomeruli exhibit a significant overlap in their receptive fields [Ma et al., 2012] or are even tuned to common functional groups [Matsumoto et al., 2010]. But on the other hand both hypotheses are also disputed and in some studies nearby glomeruli seem to be as diverse in their odor tuning as to distant ones [Soucy et al., 2009].

1.4 Conclusion

1.4.1 Topography in olfactory systems

In both mice and *Drosophila* a coarse arrangement of various receptors at the periphery is transformed into a stereotypic sensory array of glomeruli at the olfactory relay centres (olfacory bulbs in mice and antennal lobe in drosphila). Interestingly in both species their arrangement reflects to a great extent the genetic distance of the corresponding receptors. That may lead to the hypothesis that the obtained topography is a side effect of the axon-guidance in the process of separating different types of OSNs into individual glomeruli [Zhang et al., 2012]. But on the contrary there is evidence that the topography also plays a functional role. In particular the topographic arrangement is the substrate local circuits are acting upon and thus it strongly influences neural computation. Such topographic computations are in mice most pronounced in the OB's lateral network, in its projections to the AON and amgygdala and in *Drosophila* in the projections from the AL to the LH.

The following chapters investigate the functional relevance of topography in olfactory systems in two ways. First in chapter 4 it is investigated whether spatial proximity in the dorsal olfactory bulb of mice implies functional similarity. And second in chapter 5 the emergence of specific response areas in the LH by a topographic readout of the AL are explored.

1.4.2 Olfactory receptive fields

A major drawback in investigating the functional layout of the olfactory relay centres is the experimental limitation to the number of measured odours. Although the number of odourous molecules has been estimated to be more than 240000 [Boyle et al., 2013] or even 60 million [Ruddigkeit et al., 2014], currently not more than a few hundred odours have been measured for any glomerulus. Therefore all conclusions on functional similarities thus far have been drawn from only fragmentary olfactory receptive fields.

Even though improvements in experimental procedures will drastically increase the known odour responses [Peterlin et al., 2014], it seems intractable to measure all possible odour molecules. Thus it is highly desirable to obtain quantitative models of olfactory receptive fields, that is models that can interpolate the responses of unmeasured molecules from known responses [Boyle et al., 2013]. To this end chapter 3 explores ways to obtain such models.

References

Nixon M Abraham, Hartwig Spors, Alan Carleton, Troy W Margrie, Thomas Kuner, and Andreas T Schaefer. Maintaining accuracy at the expense of speed: stimulus similarity defines odor discrimination time in mice. *Neuron*, 44(5):865–876, 2004.

Hiroyuki Arakawa, Kevin R Kelliher, Frank Zufall, and Steven D Munger. The receptor guanylyl cyclase type d (gc-d) ligand uroguanylin promotes the acquisition of food preferences in mice. *Chemical senses*, 38(5): 391–397, 2013.

JL Aungst, PM Heyward, AC Puche, SV Karnup, A Hayar, G Szabo, and MT Shipley. Centre–surround inhibition among olfactory bulb glomeruli. *Nature*, 426(6967):623–629, 2003.

Leonardo Belluscio and Lawrence C Katz. Symmetry, stereotypy, and topography of odorant representations in mouse olfactory bulbs. *The Journal of Neuroscience*, 21(6):2113–2122, 2001.

Alison M Boyd, James F Sturgill, Cindy Poo, and Jeffry S Isaacson. Cortical feedback control of olfactory bulb circuits. *Neuron*, 76(6):1161–1174, 2012.

Sean Michael Boyle, Shane McInally, and Anandasankar Ray. Expanding the olfactory code by in silico decoding of odor-receptor chemical space. *Elife*, 2, 2013.

Thomas Bozza, Anne Vassalli, Stefan Fuss, Jing-Ji Zhang, Brian Weiland, Rodrigo Pacifico, Paul Feinstein, and Peter Mombaerts. Mapping of class i and class ii odorant receptors to glomerular domains by two distinct types of olfactory sensory neurons in the mouse. *Neuron*, 61(2):220–233, 2009.

Julien Brechbühl, Magali Klaey, and Marie-Christine Broillet. Grueneberg ganglion cells mediate alarm pheromone detection in mice. *Science*, 321(5892):1092–1095, 2008.

Julien Brechbühl, Fabian Moine, Magali Klaey, Monique Nenniger-Tosato, Nicolas Hurni, Frank Sporkert, Christian Giroud, and Marie-Christine Broillet. Mouse alarm pheromone shares structural similarity with predator scents. *Proceedings of the National Academy of Sciences*, 110(12):4762–4767, 2013.

H Breer, J Fleischer, and J Strotmann. Signaling in the chemosensory systems: The sense of smell: multiple olfactory subsystems. *Cellular and Molecular Life Sciences CMLS*, 63(13):1465–1475, 2006.

Peter A Brennan and Frank Zufall. Pheromonal communication in vertebrates. *Nature*, 444(7117):308–315, 2006.

Eric T Carlson, Russell J Rasquinha, Kechen Zhang, and Charles E Connor. A sparse object coding scheme in area v4. *Current Biology*, 21(4):288–293, 2011.

Sophie JC Caron, Vanessa Ruta, LF Abbott, and Richard Axel. Random convergence of olfactory inputs in the Drosophila mushroom body. *Nature*, 497(7447):113–117, 2013.

Brittany N Cazakoff, Billy YB Lau, Kerensa L Crump, Heike S Demmer, and Stephen D Shea. Broadly tuned and respiration-independent inhibition in the olfactory bulb of awake mice. *Nature neuroscience*, 17(4):569–576, 2014.

Pablo Chamero, Vicky Katsoulidou, Philipp Hendrix, Bernd Bufe, Richard Roberts, Hiroaki Matsunami, Joel Abramowitz, Lutz Birnbaumer, Frank Zufall, and Trese Leinders-Zufall. G protein gαo is essential for vomeronasal function and aggressive behavior in mice. *Proceedings of the National Academy of Sciences*, 108(31):12898–12903, 2011.

Pablo Chamero, Trese Leinders-Zufall, and Frank Zufall. From genes to social communication: molecular sensing by the vomeronasal organ. *Trends in neurosciences*, 35(10):597–606, 2012.

Jayaram Chandrashekar, Mark A Hoon, Nicholas JP Ryba, and Charles S Zuker. The receptors and cells for mammalian taste. *Nature*, 444(7117):288–294, 2006.

Xiaoke Chen, Mariano Gabitto, Yueqing Peng, Nicholas JP Ryba, and Charles S Zuker. A gustotopic map of taste qualities in the mammalian brain. *Science*, 333(6047):1262–1266, 2011.

Ya-Hui Chou, Maria L Spletter, Emre Yaksi, Jonathan CS Leong, Rachel I Wilson, and Liqun Luo. Diversity and wiring variability of olfactory local interneurons in the Drosophila antennal lobe. *Nature neuroscience*, 13 (4):439–449, 2010.

Africa Couto, Mattias Alenius, and Barry J Dickson. Molecular, anatomical, and functional organization of the Drosophila olfactory system. *Current Biology*, 15(17):1535–1547, 2005.

Stephen V David, Benjamin Y Hayden, and Jack L Gallant. Spectral receptive field properties explain shape selectivity in area v4. *Journal of neurophysiology*, 96(6):3492–3505, 2006.

Ian G Davison and Michael D Ehlers. Neural circuit mechanisms for pattern detection and feature combination in olfactory cortex. *Neuron*, 70(1):82–94, 2011.

Karina Del Punta, Adam Puche, Niels C Adams, Ivan Rodriguez, and Peter Mombaerts. A divergent pattern of sensory axonal projections is rendered convergent by second-order neurons in the accessory olfactory bulb. *Neuron*, 35(6):1057–1066, 2002.

Adam Dewan, Rodrigo Pacifico, Ross Zhan, Dmitry Rinberg, and Thomas Bozza. Non-redundant coding of aversive odours in the main olfactory pathway. *Nature*, 497(7450):486–489, 2013.

Ashesh K Dhawale, Akari Hagiwara, Upinder S Bhalla, Venkatesh N Murthy, and Dinu F Albeanu. Non-redundant odor coding by sister mitral cells revealed by light addressable glomeruli in the mouse. *Nature neuroscience*, 13(11):1404–1412, 2010.

Quentin Dietschi, Alexis Assens, Ludivine Challet, Alan Carleton, and Ivan Rodriguez. Convergence of fpr-rs3-expressing neurons in the mouse accessory olfactory bulb. *Molecular and Cellular Neuroscience*, 56:140–147, 2013.

C Dulac and S Wagner. Genetic analysis of brain circuits underlying pheromone signaling. *Annu. Rev. Genet.*, 40:449–467, 2006.

Catherine Dulac and A Thomas Torello. Molecular detection of pheromone signals in mammals: from genes to behaviour. *Nature Reviews Neuroscience*, 4(7):551–562, 2003.

Veronica Egger and Nathaniel N Urban. Dynamic connectivity in the mitral cell–granule cell microcircuit. In *Seminars in cell & developmental biology*, volume 17, pages 424–432. Elsevier, 2006.

G. Ehret. *Neurowissenschaft*, chapter 16.5, page 371ff. Springer, 2001.

Mehmet Fişek and Rachel I Wilson. Stereotyped connectivity and computations in higher-order olfactory neurons. *Nature neuroscience*, 2013.

Elane Fishilevich and Leslie B Vosshall. Genetic and functional subdivision of the Drosophila antennal lobe. *Current Biology*, 15(17):1548–1553, 2005.

David Fitzpatrick and Nachum Ulanovsky. Editorial overview: neural maps. *Current opinion in neurobiology*, 24 (1):iv–vi, 2014.

Joerg Fleischer, Katharina Mamasuew, and Heinz Breer. Expression of cgmp signaling elements in the grueneberg ganglion. *Histochemistry and cell biology*, 131(1):75–88, 2009.

C Giovanni Galizia, Daniel Münch, Martin Strauch, Anja Nissler, and Shouwen Ma. Integrating heterogeneous odor response data into a common response model: a door to the complete olfactome. *Chemical senses*, 35(7): 551–563, 2010.

David H Gire, Kevin M Franks, Joseph D Zak, Kenji F Tanaka, Jennifer D Whitesell, Abigail A Mulligan, René Hen, and Nathan E Schoppa. Mitral cells in the olfactory bulb are mainly excited through a multistep signaling path. *The Journal of Neuroscience*, 32(9):2964–2975, 2012.

Gustavo Glusman, Anita Bahar, Dror Sharon, Yitzhak Pilpel, Julia White, and Doron Lancet. The olfactory receptor gene superfamily: data mining, classification, and nomenclature. *Mammalian genome*, 11(11):1016–1023, 2000.

Yael Grosjean, Raphael Rytz, Jean-Pierre Farine, Liliane Abuin, Jérôme Cortot, Gregory SXE Jefferis, and Richard Benton. An olfactory receptor for food-derived odours promotes male courtship in Drosophila. *Nature*, 478(7368):236–240, 2011.

Anna-Katerina Hadjantonakis, Mary E Dickinson, Scott E Fraser, and Virginia E Papaioannou. Technicolour transgenics: imaging tools for functional genomics in the mouse. *Nature Reviews Genetics*, 4(8):613–625, 2003.

Elissa A Hallem and John R Carlson. Coding of odors by a receptor repertoire. *Cell*, 125(1):143–160, 2006.

Gertrud Heimbeck, Véronique Bugnon, Nanaë Gendre, Andreas Keller, and Reinhard F Stocker. A central neural circuit for experience-independent olfactory and courtship behavior in Drosophila melanogaster. *Proceedings of the National Academy of Sciences*, 98(26):15336–15341, 2001.

Martin Heisenberg, Alexander Borst, Sibylle Wagner, and Duncan Byers. Drosophila mushroom body mutants are deficient in olfactory learning: Research papers. *Journal of neurogenetics*, 2(1):1–30, 1985.

K.-P. Hoffman and C. Wehrhan. *Neurowissenschaft*, chapter 18, page 407ff. Springer, 2001.

Aiqun Hu, Wei Zhang, and Zuoren Wang. Functional feedback from mushroom bodies to antennal lobes in the Drosophila olfactory pathway. *Proceedings of the National Academy of Sciences*, 107(22):10262–10267, 2010.

Yoh Isogai, Sheng Si, Lorena Pont-Lezica, Taralyn Tan, Vikrant Kapoor, Venkatesh N Murthy, and Catherine Dulac. Molecular organization of vomeronasal chemoreception. *Nature*, 478(7368):241–245, 2011.

Gregory SXE Jefferis, Christopher J Potter, Alexander M Chan, Elizabeth C Marin, Torsten Rohlfing, Calvin R Maurer Jr, and Liqun Luo. Comprehensive maps of Drosophila higher olfactory centers: Spatially segregated fruit and pheromone representation. *Cell*, 128(6):1187–1203, 2007.

Jianzhong Jin, Yushi Wang, Harvey A Swadlow, and Jose M Alonso. Population receptive fields of on and off thalamic inputs to an orientation column in visual cortex. *Nature neuroscience*, 14(2):232–238, 2011.

Mark A Johnson, Lulu Tsai, Dheeraj S Roy, David H Valenzuela, Colleen Mosley, Angeliki Magklara, Stavros Lomvardas, Stephen D Liberles, and Gilad Barnea. Neurons expressing trace amine-associated receptors project to discrete glomeruli and constitute an olfactory subsystem. *Proceedings of the National Academy of Sciences*, 109(33):13410–13415, 2012.

Hiroyuki K Kato, Shea N Gillet, Andrew J Peters, Jeffry S Isaacson, and Takaki Komiyama. Parvalbumin-expressing interneurons linearly control olfactory bulb output. *Neuron*, 80(5):1218–1231, 2013.

Alex C Keene and Scott Waddell. Drosophila olfactory memory: single genes to complex neural circuits. *Nature Reviews Neuroscience*, 8(5):341–354, 2007.

EB Keverne, CL Murphy, WL Silver, CJ Wysocki, and M Meredith. Non-olfactory chemoreceptors of the nose: recent advances in understanding the vomeronasal and trigeminal systems. *Chemical senses*, 11(1):119–133, 1986.

Eric B Keverne. The vomeronasal organ. *Science*, 286(5440):716–720, 1999.

Shu Kikuta, Max L Fletcher, Ryota Homma, Tatsuya Yamasoba, and Shin Nagayama. Odorant response properties of individual neurons in an olfactory glomerular module. *Neuron*, 77(6):1122–1135, 2013.

Stephen W Kuffler et al. Discharge patterns and functional organization of mammalian retina. *J Neurophysiol*, 16(1):37–68, 1953.

Qian Li, Wayne J Korzan, David M Ferrero, Rui B Chang, Dheeraj S Roy, Mélanie Buchi, Jamie K Lemon, Angeldeep W Kaur, Lisa Stowers, Markus Fendt, et al. Synchronous evolution of an odor biosynthesis pathway and behavioral response. *Current Biology*, 23(1):11–20, 2013.

Stephen D Liberles. Mammalian pheromones. *Annual review of physiology*, 2013.

Stephen D Liberles, Lisa F Horowitz, Donghui Kuang, James J Contos, Kathleen L Wilson, Jessica Siltberg-Liberles, David A Liberles, and Linda B Buck. Formyl peptide receptors are candidate chemosensory receptors in the vomeronasal organ. *Proceedings of the National Academy of Sciences*, 106(24):9842–9847, 2009.

Claudia Lodovichi, Leonardo Belluscio, and Lawrence C Katz. Functional topography of connections linking mirror-symmetric maps in the mouse olfactory bulb. *Neuron*, 38(2):265–276, 2003.

Limei Ma, Qiang Qiu, Stephen Gradwohl, Aaron Scott, Q Yu Elden, Richard Alexander, Winfried Wiegraebe, and C Ron Yu. Distributed representation of chemical features and tunotopic organization of glomeruli in the mouse olfactory bulb. *Proceedings of the National Academy of Sciences*, 109(14):5481–5486, 2012.

Bettina Malnic, Junzo Hirono, Takaaki Sato, and Linda B Buck. Combinatorial receptor codes for odors. *Cell*, 96(5):713–723, 1999.

Vidya S Mandiyan, Jennifer K Coats, and Nirao M Shah. Deficits in sexual and aggressive behaviors in cnga2 mutant mice. *Nature neuroscience*, 8(12):1660–1662, 2005.

Foivos Markopoulos, Dan Rokni, David H Gire, and Venkatesh N Murthy. Functional properties of cortical feedback projections to the olfactory bulb. *Neuron*, 76(6):1175–1188, 2012.

Fernando Martin, Tamara Boto, Carolina Gomez-Diaz, and Esther Alcorta. Elements of olfactory reception in adult Drosophila melanogaster. *The Anatomical Record*, 296(9):1477–1488, 2013.

Hideyuki Matsumoto, Ko Kobayakawa, Reiko Kobayakawa, Takuya Tashiro, Kenji Mori, Hitoshi Sakano, and Kensaku Mori. Spatial arrangement of glomerular molecular-feature clusters in the odorant-receptor class domains of the mouse olfactory bulb. *Journal of neurophysiology*, 103(6):3490–3500, 2010.

Tomohiko Matsuo, Daniel Aharony Rossier, Chenda Kan, and Ivan Rodriguez. The wiring of grueneberg ganglion axons is dependent on neuropilin 1. *Development*, 139(15):2783–2791, 2012.

Shinji Matsutani and Noboru Yamamoto. Centrifugal innervation of the mammalian olfactory bulb. *Anatomical science international*, 83(4):218–227, 2008.

Soohong Min, Minrong Ai, Seul A Shin, and Greg SB Suh. Dedicated olfactory neurons mediating attraction behavior to ammonia and amines in Drosophila. *Proceedings of the National Academy of Sciences*, 110(14): E1321–E1329, 2013.

Kazunari Miyamichi, Shou Serizawa, Hiroko M Kimura, and Hitoshi Sakano. Continuous and overlapping expression domains of odorant receptor genes in the olfactory epithelium determine the dorsal/ventral positioning of glomeruli in the olfactory bulb. *The Journal of neuroscience*, 25(14):3586–3592, 2005.

Kazunari Miyamichi, Fernando Amat, Farshid Moussavi, Chen Wang, Ian Wickersham, Nicholas R Wall, Hiroki Taniguchi, Bosiljka Tasic, Z Josh Huang, Zhigang He, et al. Cortical representations of olfactory input by trans-synaptic tracing. *Nature*, 472(7342):191–196, 2011.

Kazunari Miyamichi, Yael Shlomai-Fuchs, Marvin Shu, Brandon C Weissbourd, Liqun Luo, and Adi Mizrahi. Dissecting local circuits: Parvalbumin interneurons underlie broad feedback control of olfactory bulb output. *Neuron*, 80(5):1232–1245, 2013.

Peter Mombaerts, Fan Wang, Catherine Dulac, Steve K Chao, Adriana Nemes, Monica Mendelsohn, James Edmondson, and Richard Axel. Visualizing an olfactory sensory map. *Cell*, 87(4):675–686, 1996.

Kensaku Mori and Hitoshi Sakano. How is the olfactory map formed and interpreted in the mammalian brain? *Annual review of neuroscience*, 34:467–499, 2011.

Brad C Motter. Central v4 receptive fields are scaled by the v1 cortical magnification and correspond to a constant-sized sampling of the v1 surface. *The Journal of Neuroscience*, 29(18):5749–5757, 2009.

Steven D Munger, Trese Leinders-Zufall, and Frank Zufall. Subsystem organization of the mammalian sense of smell. *Annual review of physiology*, 71:115–140, 2009.

Steven D Munger, Trese Leinders-Zufall, Lisa M McDougall, Renee E Cockerham, Andreas Schmid, Petra Wandernoth, Gunther Wennemuth, Martin Biel, Frank Zufall, and Kevin R Kelliher. An olfactory subsystem that detects carbon disulfide and mediates food-related social learning. *Current Biology*, 20(16):1438–1444, 2010.

Gabe J Murphy, Daniel P Darcy, and Jeffry S Isaacson. Intraglomerular inhibition: signaling mechanisms of an olfactory microcircuit. *Nature neuroscience*, 8(3):354–364, 2005.

Kiyomitsu Nara, Luis R Saraiva, Xiaolan Ye, and Linda B Buck. A large-scale analysis of odor coding in the olfactory epithelium. *The Journal of Neuroscience*, 31(25):9179–9191, 2011.

Ian Nauhaus and Kristina J Nielsen. Building maps from maps in primary visual cortex. *Current opinion in neurobiology*, 24:1–6, 2014.

Masatoshi Nei, Yoshihito Niimura, and Masafumi Nozawa. The evolution of animal chemosensory receptor gene repertoires: roles of chance and necessity. *Nature Reviews Genetics*, 9(12):951–963, 2008.

Shawn R Olsen, Vikas Bhandawat, and Rachel Irene Wilson. Divisive normalization in olfactory population codes. *Neuron*, 66(2):287, 2010.

Rodrigo Pacifico, Adam Dewan, Dillon Cawley, Caiying Guo, and Thomas Bozza. An olfactory subsystem that mediates high-sensitivity detection of volatile amines. *Cell reports*, 2012.

S Parrish-Aungst, MT Shipley, F Erdelyi, G Szabo, and AC Puche. Quantitative analysis of neuronal diversity in the mouse olfactory bulb. *Journal of Comparative Neurology*, 501(6):825–836, 2007.

Zita Peterlin, Stuart Firestein, and Matthew E Rogers. The state of the art of odorant receptor deorphanization: A report from the orphanage. *The Journal of general physiology*, 143(5):527–542, 2014.

William G Quinn, William A Harris, and Seymour Benzer. Conditioned behavior in Drosophila melanogaster. *Proceedings of the National Academy of Sciences*, 71(3):708–712, 1974.

Stéphane Rivière, Ludivine Challet, Daniela Fluegge, Marc Spehr, and Ivan Rodriguez. Formyl peptide receptor-like proteins are a novel family of vomeronasal chemosensors. *Nature*, 459(7246):574–577, 2009.

Lars Ruddigkeit, Mahendra Awale, and Jean-Louis Reymond. Expanding the fragrance chemical space for virtual screening. *Journal of cheminformatics*, 6(1):27, 2014.

Vanessa Ruta, Sandeep Robert Datta, Maria Luisa Vasconcelos, Jessica Freeland, Loren L Looger, and Richard Axel. A dimorphic pheromone circuit in Drosophila from sensory input to descending output. *Nature*, 468 (7324):686–690, 2010.

Raphael Rytz, Vincent Croset, and Richard Benton. Ionotropic receptors (irs): Chemosensory ionotropic glutamate receptors in Drosophila and beyond. *Insect biochemistry and molecular biology*, 2013.

Gabriela Sanchez-Andrade and Keith M Kendrick. The main olfactory system and social learning in mammals. *Behavioural brain research*, 200(2):323–335, 2009.

Julia L Semmelhack and Jing W Wang. Select Drosophila glomeruli mediate innate olfactory attraction and aversion. *Nature*, 459(7244):218–223, 2009.

Shou Serizawa, Kazunari Miyamichi, Haruki Takeuchi, Yuya Yamagishi, Misao Suzuki, and Hitoshi Sakano. A neuronal identity code for the odorant receptor-specific and activity-dependent axon sorting. *Cell*, 127(5): 1057–1069, 2006.

SR Shanbhag, B Müller, and RA Steinbrecht. Atlas of olfactory organs of Drosophila melanogaster: 1. types, external organization, innervation and distribution of olfactory sensilla. *International Journal of Insect Morphology and Embryology*, 28(4):377–397, 1999.

Katie Sokolowski and Joshua G Corbin. Wired for behaviors: from development to function of innate limbic system circuitry. *Frontiers in molecular neuroscience*, 5, 2012.

Dara L Sosulski, Maria Lissitsyna Bloom, Tyler Cutforth, Richard Axel, and Sandeep Robert Datta. Distinct representations of olfactory information in different cortical centres. *Nature*, 472(7342):213–216, 2011.

Edward R Soucy, Dinu F Albeanu, Antoniu L Fantana, Venkatesh N Murthy, and Markus Meister. Precision and diversity in an odor map on the olfactory bulb. *Nature neuroscience*, 12(2):210–220, 2009.

Marcus Stensmyr and Florian Maderspacher. Olfactory evolution: Mice rethink stink. *Current Biology*, 23(2): R59–R61, 2013.

Marcus C Stensmyr, Hany KM Dweck, Abu Farhan, Irene Ibba, Antonia Strutz, Latha Mukunda, Jeanine Linz, Veit Grabe, Kathrin Steck, Sofia Lavista-Llanos, et al. A conserved dedicated olfactory circuit for detecting harmful microbes in Drosophila. *Cell*, 151(6):1345–1357, 2012.

RF Stocker, MC Lienhard, A Borst, and KF Fischbach. Neuronal architecture of the antennal lobe in Drosophila melanogaster. *Cell and tissue research*, 262(1):9–34, 1990.

Lisa Stowers and Darren W Logan. Olfactory mechanisms of stereotyped behavior: on the scent of specialized circuits. *Current opinion in neurobiology*, 20(3):274–280, 2010.

Lisa Stowers, Peter Cameron, and Jason A Keller. Ominous odors: olfactory control of instinctive fear and aggression in mice. *Current opinion in neurobiology*, 23(3):339–345, 2013.

Jörg Strotmann, Sidonie Conzelmann, Anja Beck, Paul Feinstein, Heinz Breer, and Peter Mombaerts. Local permutations in the glomerular array of the mouse olfactory bulb. *The Journal of Neuroscience*, 20(18): 6927–6938, 2000.

Chih-Ying Su, Karen Menuz, and John R Carlson. Olfactory perception: receptors, cells, and circuits. *Cell*, 139 (1):45–59, 2009.

Nobuaki K Tanaka, Keita Endo, and Kei Ito. Organization of antennal lobe-associated neurons in adult Drosophila melanogaster brain. *Journal of Comparative Neurology*, 520(18):4067–4130, 2012a.

Nobuaki K Tanaka, Emiko Suzuki, Louis Dye, Aki Ejima, and Mark Stopfer. Dye fills reveal additional olfactory tracts in the protocerebrum of wild-type Drosophila. *Journal of Comparative Neurology*, 520(18):4131–4140, 2012b.

Roberto Tirindelli, Michele Dibattista, Simone Pifferi, and Anna Menini. From pheromones to behavior. *Physiological reviews*, 89(3):921–956, 2009.

Marco Tizzano and Thomas E Finger. Chemosensors in the nose: Guardians of the airways. *Physiology*, 28(1): 51–60, 2013.

Akio Tsuboi, Takeshi Imai, Hiroyuki K Kato, Hideyuki Matsumoto, Kei M Igarashi, Misao Suzuki, Kensaku Mori, and Hitoshi Sakano. Two highly homologous mouse odorant receptors encoded by tandemly-linked mor29a and mor29b genes respond differently to phenyl ethers. *European Journal of Neuroscience*, 33(2):205–213, 2011.

Pierre Vanderhaeghen, Qiang Lu, Neal Prakash, Jonas Frisén, Christopher A Walsh, Ron D Frostig, and John G Flanagan. A mapping label required for normal scale of body representation in the cortex. *Nature neuroscience*, 3(4):358–365, 2000.

Leslie B Vosshall and Reinhard F Stocker. Molecular architecture of smell and taste in Drosophila. *Annu. Rev. Neurosci.*, 30:505–533, 2007.

Shlomo Wagner, Amy L Gresser, A Thomas Torello, and Catherine Dulac. A multireceptor genetic approach uncovers an ordered integration of vno sensory inputs in the accessory olfactory bulb. *Neuron*, 50(5):697–709, 2006.

Jennifer D Whitesell, Kyle A Sorensen, Brooke C Jarvie, Shane T Hentges, and Nathan E Schoppa. Interglomerular lateral inhibition targeted on external tufted cells in the olfactory bulb. *The Journal of Neuroscience*, 33 (4):1552–1563, 2013.

Rachel I Wilson. Early olfactory processing in Drosophila: mechanisms and principles. *Annual review of neuroscience*, 36:217, 2013.

Zhiqiang Yan, Jie Tan, Chang Qin, Yao Lu, Cheng Ding, and Minmin Luo. Precise circuitry links bilaterally symmetric olfactory maps. *Neuron*, 58(4):613–624, 2008.

C Ron Yu, Jennifer Power, Gilad Barnea, Sean O'Donnell, Hannah EV Brown, Joseph Osborne, Richard Axel, and Joseph A Gogos. Spontaneous neural activity is required for the establishment and maintenance of the olfactory sensory map. *Neuron*, 42(4):553–566, 2004.

Sidney Yu, Leon Avery, Eric Baude, and David L Garbers. Guanylyl cyclase expression in specific sensory neurons: a new family of chemosensory receptors. *Proceedings of the National Academy of Sciences*, 94(7): 3384–3387, 1997.

Feng Zhang, Alexander M Aravanis, Antoine Adamantidis, Luis de Lecea, and Karl Deisseroth. Circuit-breakers: optical technologies for probing neural signals and systems. *Nature Reviews Neuroscience*, 8(8):577–581, 2007.

Jingji Zhang, Guangzhe Huang, Adam Dewan, Paul Feinstein, and Thomas Bozza. Uncoupling stimulus specificity and glomerular position in the mouse olfactory system. *Molecular and Cellular Neuroscience*, 51(3):79–88, 2012.

Chen Zheng, Paul Feinstein, Thomas Bozza, Ivan Rodriguez, and Peter Mombaerts. Peripheral olfactory projections are differentially affected in mice deficient in a cyclic nucleotide-gated channel subunit. *Neuron*, 26(1): 81–91, 2000.

Dong-Jing Zou, Paul Feinstein, Aimée L Rivers, Glennis A Mathews, Ann Kim, Charles A Greer, Peter Mombaerts, and Stuart Firestein. Postnatal refinement of peripheral olfactory projections. *Science*, 304(5679): 1976–1979, 2004.

NeuroImage 98 (2014) 279–288

Contents lists available at ScienceDirect

NeuroImage

journal homepage: www.elsevier.com/locate/ynimg

Automatic segmentation of odor maps in the mouse olfactory bulb using regularized non-negative matrix factorization

Jan Soelter [a], Jan Schumacher [b], Hartwig Spors [b], Michael Schmuker [a,c,*]

[a] Neuroinformatics & Theoretical Neuroscience, Institute of Biology, Freie Universität Berlin, 14195 Berlin, Germany
[b] Max-Planck Institute for Biophysics, Frankfurt am Main, Germany
[c] Bernstein Center for Computational Neuroscience Berlin, 10119 Berlin, Germany

ARTICLE INFO

Article history:
Accepted 12 April 2014
Available online 24 April 2014

Keywords:
Non-negative matrix factorization
Independent component analysis
Intrinsic optical signal
Olfactory bulb

ABSTRACT

Segmentation of functional parts in image series of functional activity is a common problem in neuroscience. Here we apply regularized non-negative matrix factorization (rNMF) to extract glomeruli in intrinsic optical signal (IOS) images of the olfactory bulb. Regularization allows us to incorporate prior knowledge about the spatio-temporal characteristics of glomerular signals. We demonstrate how to identify suitable regularization parameters on a surrogate dataset. With appropriate regularization segmentation by rNMF is more resilient to noise and requires fewer observations than conventional spatial independent component analysis (sICA). We validate our approach in experimental data using anatomical outlines of glomeruli obtained by 2-photon imaging of resting synapto-pHluorin fluorescence. Taken together, we show that rNMF provides a straightforward method for problem tailored source separation that enables reliable automatic segmentation of functional neural images, with particular benefit in situations with low signal-to-noise ratio as in IOS imaging.

Introduction

Measuring the activity of large neuronal ensembles is a fundamental problem in neuroscience. Functional optical imaging is a widely used tool to measure spatio-temporal responses of neuronal ensembles distributed over extended brain areas. Many neuroscientific questions require identification of regions in the imaged areas which exhibit correlated activity, for example groups of neurons which are functionally related or anatomically grouped. For an efficient work-flow it is desirable that large volumes of recorded ensemble activity are automatically disaggregated into functional/anatomical parts, with each part characterized by its associated pixels (spatial location) and their common time-course (Dorostkar et al., 2010). The automatic segmentation of neuronal activity is not only important to increase experimental throughput, but also to increase the reproducibility and reliability of the results.

For instance, this problem arises in extracting individual glomeruli and their response time-course from optical recordings of the olfactory bulb, a system extensively studied using functional imaging (for a review see Pain et al., 2011). Glomeruli are the first relay station in the olfactory pathway, with each glomerulus relaying the convergent input of a distinct type of olfactory sensory neurons (OSNs) expressing the same olfactory receptor (Firestein, 2001). Thus, the input to the glomerular ensemble represents the basic sensory representation of the olfactory world. Our understanding of this representation is still rudimentary and disputed (Ma et al., 2012; Murthy, 2011; Soucy et al., 2009). This circumstance demands large-scale studies of chemical receptive fields of glomeruli and their spatial arrangement, a task conveniently achieved using optical imaging of neuronal activity.

A well established technique for imaging the dorsal olfactory bulb is to measure reflectance at about 700 nm, the so-called intrinsic optical signal (IOS) (Rubin and Katz, 1999).

The IOS comprises both a global diffuse signal and a local signal originating in the glomeruli (Meister and Bonhoeffer, 2001). The local signal is related to OSN glutamate release and its uptake by astrocytes (Gurden et al., 2006). It has been demonstrated that the IOS corresponds well to both pre-synaptic calcium signals (Wachowiak and Cohen, 2003) and pre-synaptic exocytosis measured using synapto-pHluorin (Soucy et al., 2009). However, the intrinsic optical signal is by a factor of three to ten (calcium) up to twenty (synapto-pHluorin) weaker, implying a smaller signal-to-noise ratio which poses a significant challenge to data analysis. The advantage of IOS imaging is that it doesn't require an ion-sensitive dye, which significantly simplifies the experimental procedure.

* Corresponding author at: Neuroinformatics & Theoretical Neuroscience, Institute of Biology, Freie Universität Berlin, 14195 Berlin, Germany.
E-mail address: m.schmuker@fu-berlin.de (M. Schmuker).

http://dx.doi.org/10.1016/j.neuroimage.2014.04.041
1053-8119/

A range of algorithms and techniques have been applied with the aim of identifying both the location of glomeruli and the time course of their activation from the noisy optical imaging data. In the most straightforward approach the image is de-noised and spatial regions of interest are selected as local maxima of odor induced activation, crossing a defined threshold (Bathellier et al., 2007; Belluscio and Katz, 2001; Ma et al., 2012; Meister and Bonhoeffer, 2001; Wachowiak and Cohen, 2001). The corresponding time courses are then extracted from the surrounding pixels. However, choosing the right threshold is difficult. A high threshold delivers robust segmentation of single spatial peaks in the signal, but small activations may not be detected. In contrast, neighboring strong response regions merge when using a low threshold (Dorostkar et al., 2010). Furthermore biological responses to stimuli are often superimposed onto biological and technical noise sources (Grinvald et al., 1999). The manual choice of a threshold may also complicate the reproduction of results in independent experiments even if experimental conditions vary only slightly.

Techniques for blind source separation (BSS) offer an elegant way out of this dilemma. Using BSS techniques it is possible to separate distinct sources which compose a signal, allowing the simultaneous determination of spatial extent and temporal response of the sources (*i.e.* glomeruli in our case). For example spatial independent component analysis (sICA) was successfully applied to analyze IOS odor responses in the mouse olfactory bulb (Reidl et al., 2007) and to extract glomeruli in calcium imaging experiments in the honeybee antennal lobe (Strauch and Galizia, 2012). The sICA approach relies on the spatial structures of the sources being independent, *i.e.* that they are located at different positions or have different shapes (*e.g.*, blood vessels *vs.* glomeruli). Instead of assuming spatial independence, other approaches in optical imaging segmentation have been proposed which separate sources by assuming temporal (Strauch and Galizia, 2012) or spatio-temporal (Mukamel et al., 2009) independence. But since glomeruli can exhibit largely overlapping ligand spectra and hence correlated odor responses (Ma et al., 2012), the assumption of temporal independence is violated and thus requires at least an additional step of image segmentation. Also the convex cone analysis (Strauch et al., 2012) suffers from the demand of additional post-processing steps.

We propose regularized non-negative matrix factorization (rNMF) (Cichocki and Anh-Huy, 2009) as an alternative approach to identify the spatial location and temporal activity of glomeruli in the olfactory bulb. rNMF allows incorporating *a priori* knowledge about the source characteristics through appropriate regularization terms. In our case, this knowledge comprises both the spatial arrangement of glomeruli, largely side to side with a diameter of 40–190 mm (Royet et al., 1988), and the excitatory response characteristic of OSNs to odor stimulation (Nara et al., 2011). Because the accuracy of BSS depends critically on the suitability of the assumption underlying the factorization algorithm, the incorporation of prior knowledge renders rNMF a well suited approach for glomerulus extraction.

In this study, we introduce regularization terms specific to our BSS problem of identifying glomeruli and extracting their response time-courses in IOS imaging. We elucidate how suitable parameters can be chosen in a data-driven fashion. In addition, we compare the rNMF approach to conventional sICA and examine the application domain of both approaches.

Materials and methods

Mathematical notation

Matrices are denoted in bold capital letters and bold small letters indicate column vectors. Therefore $\mathbf{a}^T\mathbf{x}$ represents the dot product and $\mathbf{a}\mathbf{x}^T$ the outer product.

Experiments

Functional intrinsic optical signal imaging

Three OMP-SpH-mice (9–22 weeks) (Bozza et al., 2004) were anaesthetized using urethane (1.5 g/kg i.p.). Anaesthetic was supplemented throughout the experiments and the body temperature was kept between 36.5 °C and 37.5 °C using a heating pad and a rectal probe. For imaging a craniotomy over one olfactory bulb was cut. The dura mater was removed and the imaging chamber was filled with agar (1.5%) and covered with a glass cover slip. The prepared skull was fixated with cement to a metal plate under the microscope. All animal care and procedures were in accordance with the animal ethics guidelines of the Max Planck Society.

Instant JChem was used for searching, managing and property prediction of odorants in a chemical database (Instant JChem 5.9.4, 2012, ChemAxon, http://www.chemaxon.com).

Odors were presented with a two armed robot (Combipal, CTC-Analytics, Zwingen, Switzerland) using the Software Chronos (Axel Semrau, Sprockhoevel, Germany). 2.5 ml of the odor headspace was injected into a constant carrier flow of filtered and humidified air (2 l/min) towards the mouse's nose. After each odor presentation the syringe used for odor transfer was flushed with nitrogen for 72 s to minimize contamination. Odor responses were recorded in the dorsal olfactory bulb for 12 s at 5 Hz using a macroscope (Pentax Zoom lens 12–48 mm, f = 1:1.0 and Nikkor 135 mm, f = 1:2.0) and an Orca-R2 camera (Hamamatsu, Japan; 1024 × 1344 pixels, field of view 1.63 mm × 1.24 mm) under illumination with red light (690 nm). Odor molecules reached the nose 2.5 ± 0.3 s after recording onset as measured by a photoionization detector (Aurora Scientific, Canada). In each animal the response to a stimulus set of 46 to 47 odors was recorded (for odor list see supplemental table T1). Each odor stimulus was repeated at least twice and stimuli were represented in a pseudo-randomized sequence. Before and after each presentation of the entire stimulus set, the pattern of blood vessels was recorded using green illumination (546 nm, 'green image') and controlled for shifts to exclude movement artifacts.

Anatomical SpH imaging

In addition to functional imaging we performed an anatomical scan in all mice. Synapto-pHluorin labeled OB glomeruli were imaged using a 2-photon laser scanning microscope (Prairie Technologies, Middleton, TN, USA), a 16× water immersion objective (N.A. 0.8, Nikon, back aperture overfilled) and a MaiTai DeepSee laser (50–170 mW, tuned to 880 nm, 80 MHz repetition rate of pulses 120 fs in length; Spectra-Physics/Newport, Santa Clara, CA, USA). Images (512 × 512 pixels) were acquired at 3 μm steps in z-direction. Multiple Z-stacks were stitched and aligned to the functional imaging data using custom written Matlab scripts. For alignment we used the blood vessel pattern obtained by illuminating the olfactory bulb using the 'green image' recorded at a wavelength of 546 nm. We manually outlined glomeruli in the Z-stacks (see Supplementary movie). To avoid a bias in the outlining procedure the glomeruli were identified with the experimenter blinded to the results of factorization.

Data preprocessing

To increase signal-to-noise ratio and reduce computational load the raw data was filtered by binning with an 8 × 8 pixel spatial and a 12 frame temporal window. Then the odor induced activation was calculated as the relative decrease of reflectance $-\Delta R/R = -(R - R_0)/R$. R_0 is the mean reflectance on the first 2 s after recording onset, well before the odors reached the nose (see above). Furthermore the data was spatially bandpass filtered with two Gaussian filters ($\sigma_{low} = 10$ pixels, $\sigma_{high} = 1$ pixels) and down-sampled by a factor of 2. The final resolution of the measurement time series was thus 64 × 84 pixels at 0.42 Hz. The concatenation of the preprocessed frames for all odors

leads to the measurement matrix $\mathbf{Y} \in R^{F \times P}$ with element $Y_{f,p}$ being the observed value of the pth pixel in the fth frame. Every fifth frame is the start of a new odor o_i, in the following denoted as f_{o_i}.

After preprocessing we estimated the remaining pixel noise as the standard deviation of pixel activation in response to the 'non-odor' Argon.

Surrogate data

To evaluate the factorization performance we created surrogate datasets resembling the main characteristics of the biological case. That is we randomly placed 40 sources side by side on a regular 9 × 9 grid in a 50 × 50 pixel image (Fig. 1a). A source s contributes to the activation of a pixel p with a decaying pixel participation $\mathbf{x}_s$ around the source's center $x_{s,p} = \exp(-0.1(p - p_s^{center})^2)$ (Fig. 1d). For a set of $i = 1, \ldots n$ surrogate stimuli o_i, we drew peak activations $a_{o_i,s}$ from a gamma distribution ($\mu = 0.2$, $\sigma = 0.28$) (Fig. 1b), resulting in a narrowly tuned response spectrum $\mathbf{spec}_s = (a_{o_1,s}, a_{o_2,s}, \ldots, a_{o_n,s})$. A temporal correlation between groups of sources, as depicted in Fig. 1b, was introduced *via* a Gaussian copula (Nelsen, 1998). Furthermore each stimulus response was expanded to a six frame time series mimicking the shape of an experimentally observed time course (Fig. 1c). The concatenation of these single stimuli responses yielded the overall time series $\mathbf{a}_s$

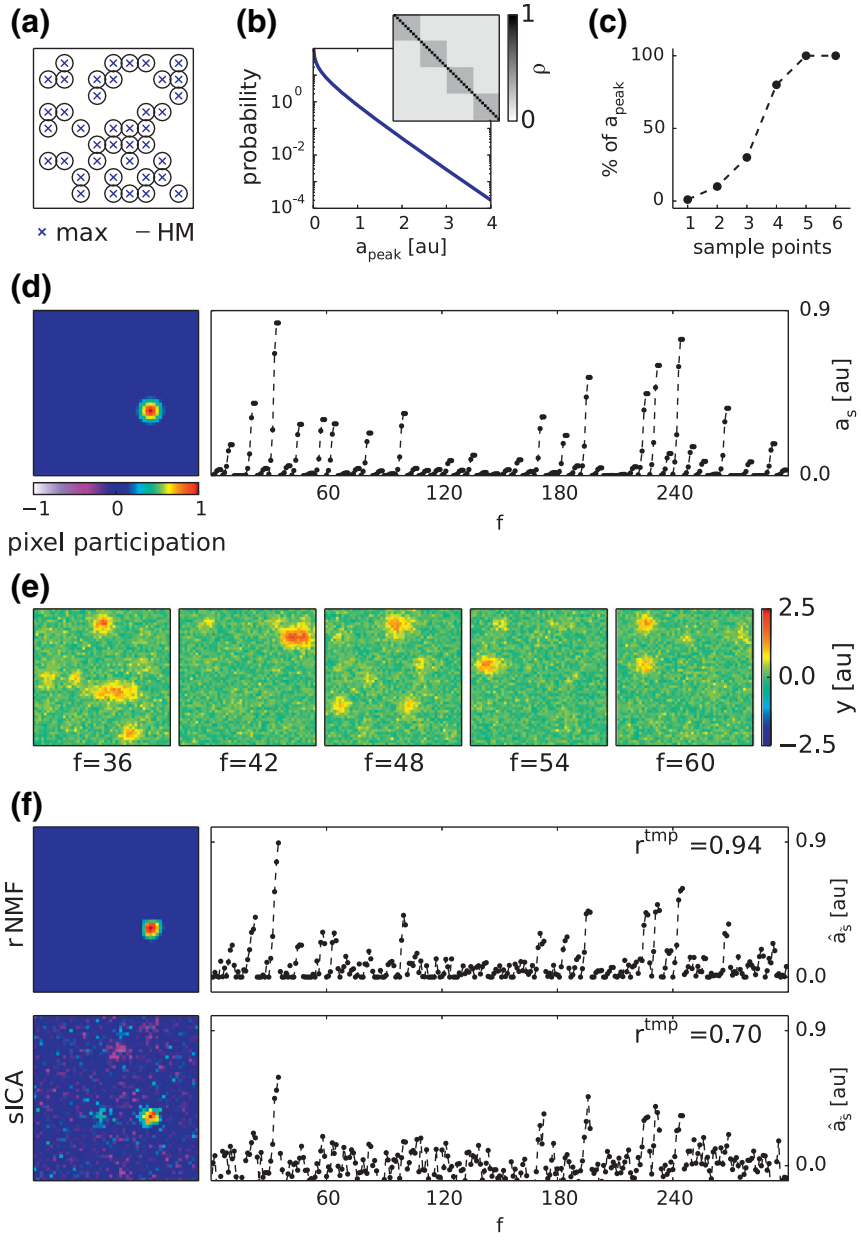

Fig. 1. Surrogate data. (a) 40 Gaussian shaped sources randomly placed on a regular 9 × 9 grid in a 50 × 50 pixel image. Crosses mark centers of pixel participation and circles indicate half maximum. (b) Distribution of per-stimulus peak activations (in arbitrary units au) (gamma distribution with $\mu = 0.2$, $\sigma = 0.28$). Inset: Gaussian copula with correlations ρ used to induce temporal correlation within four groups of sources. (c) Six-point model time-course for stimulus activation. (d) Pixel participation (left) and full activation time series of a source instance (50 odors in 300 frames f). (e) Surrogate signal for five example stimuli at peak activation, including gaussian pixel noise ($\sigma_{noise} = 0.2$). (f) Left panels: recovered source in rNMF (top) and sICA (bottom). Right panels: reconstructed source activation time series. Temporal correlation r^{tmp} to true source is given in upper left corners.

of a source s, modeling the response of a single glomerulus throughout a series of measurements. Finally the summed activation of all sources gave the overall spatio-temporal observation $\mathbf{Y} = \sum_s \mathbf{a}_s \mathbf{x}_s^T + \mathbf{N}$ additionally corrupted by gaussian pixel noise $N_{f,p} \in \mathcal{N}(0, \sigma_{\text{noise}})$ (Fig. 1e).

Matrix factorization

The objective of matrix factorization is to obtain a decomposition of observation $\mathbf{Y}$ into K components with time-courses $\hat{\mathbf{A}} \in R^{F \times K}$ and pixel participations $\hat{\mathbf{X}} \in R^{K \times P}$. Therein $\hat{a}_{f,k}$ is the activation value of component k in the fth frame and $\hat{x}_{k,p}$ the participation of the pth pixel in it. Accordingly $\hat{\mathbf{a}}_k$ is the full time-course of this component and $\hat{\mathbf{x}}_k$ the participation strength for all pixels. The reconstruction of a measurement is then given by $\hat{\mathbf{Y}} = \sum_k \hat{\mathbf{a}}_k \hat{\mathbf{x}}_k^T = \hat{\mathbf{A}}\hat{\mathbf{X}}$ and a measurement is described as its reconstruction and the unexplained residual data $\mathbf{Y} = \hat{\mathbf{A}}\hat{\mathbf{X}} + \mathbf{R}$. After factorization we rescaled $\hat{\mathbf{x}}'_k = \hat{\mathbf{x}}_k / \max(\hat{\mathbf{x}}_k)$ and $\hat{\mathbf{a}}'_k = max(\hat{\mathbf{x}}_k) * \hat{\mathbf{a}}_k$ which leaves the contribution of a component $\hat{\mathbf{a}}'_k \hat{\mathbf{x}}'^T_k = \hat{\mathbf{a}}_k \hat{\mathbf{x}}_k^T$ invariant and allows for reading the pixel-participation as relative strength of participation in the common time series.

Spatial ICA (sICA)

In sICA, factorization is performed under the objective that all pixel participations $\hat{\mathbf{x}}_k$ are mutually independent. We employed the FastICA implementation of scikit-learn (Pedregosa et al., 2011) to obtain such a factorization. First the data is whitened and reduced to K components *via* principal component analysis. The choice of K determines the number of unique components extracted by ICA. The resulting factorization $\mathbf{Y} = \mathbf{A}^{\text{PCA}}\mathbf{X}^{\text{PCA}} + \mathbf{R}$ has minimal variance in residual $\mathbf{R}$ and orthogonal pixel participations $\mathbf{x}_k^{\text{PCA}}$ of zero mean and unit variances. To obtain pixel participations $\hat{\mathbf{x}}_k$ which are not only uncorrelated but independent, FastICA estimates an unmixing matrix $\mathbf{W}$ maximizing the nongaussianity/negentropy of the 'unmixed' components $\hat{\mathbf{X}} = \mathbf{W}\mathbf{X}^{\text{PCA}}$ (Hyvärinen, 1999). This yields the final factorization $\mathbf{Y} = \hat{\mathbf{A}}\hat{\mathbf{X}} + \mathbf{R} = \mathbf{A}^{\text{PCA}}\mathbf{W}^{-1}\mathbf{W}\mathbf{X}^{\text{PCA}} + \mathbf{R}$.

Regularized NMF (rNMF)

In non-negative matrix factorization the values of factorization are restricted to be positive ($a_{f,k} \geq 0, x_{k,p} \geq 0 \; \forall \, f, k, p$). Positive pixel participations enable straightforward physiological interpretation, reading the pixel values in each component as contribution values of the extracted physiological source. Positive time-courses reflect the assumption that source responses are excitatory. To obtain such a factorization the HALS algorithm iteratively minimizes the reconstruction error $\mathbf{R} = \left|\left|\mathbf{Y} - \hat{\mathbf{A}}\hat{\mathbf{X}}\right|\right|_F^2$ under the non-negativity constraint (Cichocki and Anh-Huy, 2009), with $||||_F$ denoting the Frobenius Norm. To further constrain the factorization to known characteristics of the hidden sources the algorithm allows the imposition of additional regularization to the estimation. This is achieved by jointly minimizing the reconstruction error $\mathbf{R}$ together with a constraint C in the form $\left|\left|\mathbf{Y} - \hat{\mathbf{A}}\hat{\mathbf{X}}\right|\right|_F^2 + \alpha C\left(\hat{\mathbf{A}}, \hat{\mathbf{X}}\right)$, with α determining their trade off.

In general there is no unique solution of the NMF problem (Donoho and Stodden, 2004). Especially if two sources have a similar activation profile, a valid factorization would be a component reflecting the common ground activation and components containing the deviation.

To avoid the explanation of pixel group activations in more than one component, a good solution $\hat{\mathbf{X}}$ contains only minimal off-diagonal elements in the components' spatial overlap matrix $\hat{\mathbf{X}}\hat{\mathbf{X}}^T$, leading to the global sparseness regularization term $C_{\text{sp}}\left(\hat{\mathbf{X}}\right) = \sum_j \sum_{k \neq j} \hat{\mathbf{x}}_j \hat{\mathbf{x}}_k$ (Chen and Cichocki, 2005). This term reflects the assumption that glomerular signals recorded by IOS imaging show only weak overlap. As a further physiological constraint we took into account that neighboring pixels are likely to belong to the same source. This was reflected in a smoothness regularization, minimizing the spatial variation of each component $C_{\text{sm}} = \sum_k \sum_p \left(\hat{x}_{k,p} - \mathbf{l}_p^T \hat{\mathbf{x}}_k\right)^2$ with $\mathbf{l}_p$ being the neighborhood vector of the pth pixel reflecting its 2D connectivity (Cichocki and Anh-Huy, 2009). Taking both regularizations together, a solution is preferred where the activation of a pixel is either attributed to a single source or the mixed signal of neighboring sources.

We used the hierarchical alternating least squares (HALS) framework (Cichocki and Anh-Huy, 2009) to optimize our regularized objective function. The full algorithm is provided in Appendix A.

The HALS algorithm can be initialized with any guess of $\hat{\mathbf{A}}$ and $\hat{\mathbf{X}}$. We chose a deterministic approach to obtain reproducible results and avoid any chance effects of random initialization (see Appendix B). In detail, we started with the pixel with the maximal peak activation in the signal and selected its time-course to initialize the first component. Then the participation of all pixels in this time-course was calculated and their contributions to the signal was subtracted from the data to obtain the unexplained residuals $\mathbf{R} = \mathbf{Y} - \hat{\mathbf{a}}_k \hat{\mathbf{x}}_k^T$. We repeated this procedure on the residuals $\mathbf{R}$ until we initialized all k components. This approach is similar to convex cone analysis (Strauch et al., 2012). Strauch et al. selected the pixel with the highest euclidean norm, essentially choosing the pixel with the highest variance. We instead chose the maximum norm (highest peak activation) to address the expected sources' activation characteristics of few but strong (*i.e. sparse*) activations.

Sequential compositions of rNMF and sICA

Both sICA and rNMF might provide complementary aspects of a solution. Therefore we created various sequential compositions of these approaches. The first composition we assessed was to perform one approach on the reconstructed data $\hat{\mathbf{Y}} = \hat{\mathbf{A}}\hat{\mathbf{X}} = \mathbf{Y} - \mathbf{R}$ of the other one. It implies the assumption that the residual $\mathbf{R}$ of the first factorization mainly contains noise, and removing it is equivalent to de-noising the data.

The second composition we used was to initialize rNMF by the rectified factorization $[\mathbf{X}^{\text{sICA}}]_+$, $[\mathbf{A}^{\text{sICA}}]_+$ of sICA. *Vice versa*, sICA was performed directly on the pixel participation $\mathbf{X}^{\text{rNMF}}$ of rNMF (instead of performing it on the data $\mathbf{Y}$). This procedure yielded a total of four sequential compositions of rNMF and sICA: 1) rNMF initialized with the rectified sICA components, 2) rNMF performed on the sICA reconstruction ('de-noising by sICA'), 3) sICA performed on pixel participations obtained with rNMF, and 4) sICA performed on rNMF reconstructions ('de-noising by rNMF').

Performance criteria

We employed different measures to evaluate the performance of factorization. In rNMF we estimated the efficiency of the sparseness constraint by calculating the spatial correlation (pixel-wise Pearson's r) of components. Especially the highest correlation $r_k^{\text{comp}} = \max_j r(\hat{\mathbf{x}}_k, \hat{\mathbf{x}}_j)$ highlights shared explanation of pixel groups in the factorization, which is in opposition to the assumption of locally sparse signals.

In case of the surrogate dataset where the ground truth is known we furthermore directly assessed how well the true sources were reconstructed in factorization. Therefore each source was assigned to the component to which it exhibited the highest spatial correlation $\tilde{s} = \arg\max_i r(\hat{\mathbf{x}}_i, \mathbf{x}_s)$. The recovery error of a source was then calculated as the relative mean squared error of reconstruction for all time-points and pixels $\text{MSE}_s = \sum_{f,p} (a_{f,s} x_{s,p} - \hat{a}_{f,\tilde{s}} \hat{x}_{\tilde{s},p})^2 / \sum_{f,p} (a_{f,s} x_{s,p})^2$. As $\hat{\mathbf{x}}_{\tilde{\mathbf{s}}}$ in sICA exhibits small but many non-local values (see Fig. 1f), this measure would indicate worse performance than actually could be

achieved by simple post-processing like thresholding. To ensure a fair performance comparison between sICA and rNMF, we therefore accounted for potential post-processing improvements by calculating the sICA recovery error only for the local source region $\mathrm{MSE}_s^{\mathrm{sICA}_{\mathrm{loc}}} = \sum_{f,p^{\mathrm{loc}}}\left(a_{f,s}x_{s,p^{\mathrm{loc}}} - \hat{a}_{f,\hat{s}}\hat{x}_{\hat{s},p^{\mathrm{loc}}}\right)^2 / \sum_{f,p^{\mathrm{loc}}}\left(a_{f,s}x_{s,p^{\mathrm{loc}}}\right)^2$ for pixels $p^{\mathrm{loc}} = \{p | x_{s,p} > 0.05\}$ which have a substantial participation in the original source. Instead of recovery error, we will report the counterpart source recovery $\mathrm{SR} = 1 - \mathrm{MSE}$. Furthermore we characterized coincidence of source and matched component by evaluating their mutual spatial and temporal correlation, $r_s^{\mathrm{spt}} = r(\hat{\mathbf{x}}_{\hat{s}}, \mathbf{x}_s)$ and $r_s^{\mathrm{tmp}} = r(\hat{\mathbf{a}}_{\hat{s}}, \mathbf{a}_s)$.

For the experimentally obtained IOS data the ground truth is unknown. Nevertheless we were able to utilize the exactly defined experimental design of repeated stimuli and the generally high reproducibility of odor responses on single trial basis (Spors and Grinvald, 2002) for evaluating temporal characteristics of a component. For each component k we calculated its response spectrum $\mathbf{spec}_k = (a_{o_1,k}, a_{o_2,k}, \ldots, a_{o_n,k})$ to the first and second stimulus repetition. The response to an odor o_i was the mean activation 4.8 s–12 s after odor measurement onset: $a_{o_i,k} = \sum_{f=f_{o_i}+2}^{f_{o_i}+4} \hat{a}_{f,k}/3$. The trial-to-trial correlation of response spectra $r_k^{\mathrm{t2t}} = r(\mathbf{spec}_k^{\mathrm{1st}}, \mathbf{spec}_k^{\mathrm{2nd}})$ reflects then the stimulus correlated fraction of activation in the component. Low r_k^{t2t} indicates sources with weak coupling to odor stimulation, for example blood vessels.

Source code

Source code (Python) for performing rNMF, including a GUI version, is available online at https://github.com/jansoe/FUImaging/tree/Neuroimage2014. In the "examples" subfolder of this repository, we provide IPython Notebooks to reproduce the data analysis performed in this manuscript. Supplemental file 3 contains the necessary data. Online inspection of this code is possible at http://nbviewer.ipython.org/github/jansoe/FUImaging/blob/master/examples/IOSsegmentation/regNMF.ipynb.

Results

The purpose of this study was to incorporate appropriate regularization in the NMF framework to improve automatic segmentation of glomeruli in the mouse olfactory bulb in IOS imaging. We first use surrogate data to analyze the benefits of rNMF, including the performance-critical choice of appropriate regularization. In a practical IOS imaging scenario we illustrate the capability of rNMF to infer glomerular positions and responses, and verify the results using anatomical measurements. At all stages, we compare the performance of the rNMF approach to conventional sICA.

Segmentation of surrogate data

It is generally difficult to assess factorization performance for experimentally obtained imaging data because the ground truth is unknown. To obtain nevertheless a detailed picture on the terms of performance for rNMF and sICA we constructed a parameterized surrogate dataset in which we have full control over the sources composing the signal. With this dataset we could address two important questions: First, what is the influence of method inherent parameters and how can we choose their values for a given dataset? And second, what is the application domain of both methods with respect to strength of pixel noise and number of measured stimuli? To answer these questions we constructed surrogate sources resembling the main characteristics of our biological object of research. Surrogate glomeruli are arranged side by side with overlapping spatial signal distribution (Fig. 1a). This induces a spatial correlation of 0.29, *i.e.* a small dependence, to neighboring sources. Their response spectra are narrowly tuned and groups of glomeruli exhibit correlation in their response spectra (Fig. 1b). Each glomerulus rises to peak activation with a model time-course that mimics measured response dynamics (Fig. 1c). The data to enter factorization is the concurrent observation of 40 glomeruli in response to n_{stim} stimuli (*e.g.* odors) corrupted by additional pixel noise σ_{noise} (Fig. 1e).

We started our analysis with a dataset roughly mimicking the properties of our intrinsic optical signal (IOS) imaging data with $n_{\mathrm{stim}} = 50$ stimulus observations and a noise level of $\sigma_{\mathrm{noise}} = 0.2$. Fig. 1f shows an example of a recovered source from both rNMF ($\alpha_{\mathrm{sm}} = 2$, $\alpha_{\mathrm{sp}} = 0.5$) and sICA, illustrating the general characteristics of the methods. rNMF indeed showed the desired properties of a localized, sparse and smooth pixel participation, accurately reproducing the spatial and temporal characteristics of the source. In contrast plain sICA (with no additional processing applied) generates more holistic pixel participations, containing global noise contributions besides the local source contribution. While the non-local aspects could probably be mitigated using suitable post-processing, this result points out a more noisy reconstruction of the activation courses by sICA, especially for weaker signals.

Choice of regularization parameters

The outcome of rNMF factorization depends on the choice of regularization. On the basis of problem-specific knowledge we devised two regularization terms on the basis of expected source characteristics: spatial sparseness and spatial smoothness (see Materials and methods). The relative influence of those regularization terms is governed by the parameters α_{sp} (sparseness) and α_{sm} (smoothness). We systematically evaluated their effect on factorization results on the surrogate data in order to provide a heuristic for choosing useful parameter values.

We first started with the parameter for smoothness regularization α_{sm}. With $\alpha_{\mathrm{sm}} = \alpha_{\mathrm{sp}} = 0$, that is without any regularization, pixel participations of the NMF components spread across the whole image, containing small scale structures of one pixel size. These small scale structures progressively disappeared as we increased the smoothness regularization to $\alpha_{\mathrm{sm}} = 8$ (Fig. 2a). Nonetheless, the extracted components contained contributions from different sources even with strong smoothness regularization. Therefore we introduced sparseness regularization, which controls the number of components a pixel is participating through the parameter α_{sp}. With moderate regularization ($\alpha_{\mathrm{sp}} = 0.5$), a component exactly described a single source (Fig. 2b, left panel). Setting its value too high (*e.g.* $\alpha_{\mathrm{sp}} = 4$) resulted in components covering only part of a source, as any overlap of components is prevented by the regularization (Fig. 2b, right panel).

To further quantify the effect of sparseness regularization we employed two measures. First, we calculated the recovery of the actual surrogate sources by the components, SR_k. Second, we measured shared explanation of pixel groups in multiple components *via* spatial correlation between components r_k^{comp} (see Materials and methods). This is an uninformed measure not depending on any knowledge of actual sources, and hence is also applicable when the ground truth is not known, *i.e.* in real experimental data.

We found that the mean source recovery SR_k, starting at almost zero without any sparseness regulation, increased to a maximum at about $\alpha_{\mathrm{sp}} = 0.25$ (2^{-2}) and then decreased again (Fig. 2c). In contrast, the maximal mutual correlation between components r_k^{comp} started to decrease to zero at sparseness regularization values of $\alpha_{\mathrm{sp}} > 0.125$ (2^{-3}) (Fig. 2c). The range of maximal source recovery was thus in a regime where all strong component correlations became eliminated but some residual correlation was left. This reflects the fact that neighboring sources actually have a spatial correlation of $r = 0.26$ due to their spatial overlap. The interdependency of both measures suggests the simple heuristic to choose α_{sp} in a regime where spatial component correlation starts to be significantly reduced. In the following we implemented this by choosing $\alpha_{\mathrm{sp}}^{\mathrm{opt}}$ as the first value of α_{sp} where $\max_k r_k^{\mathrm{comp}}$ drops below 0.5.

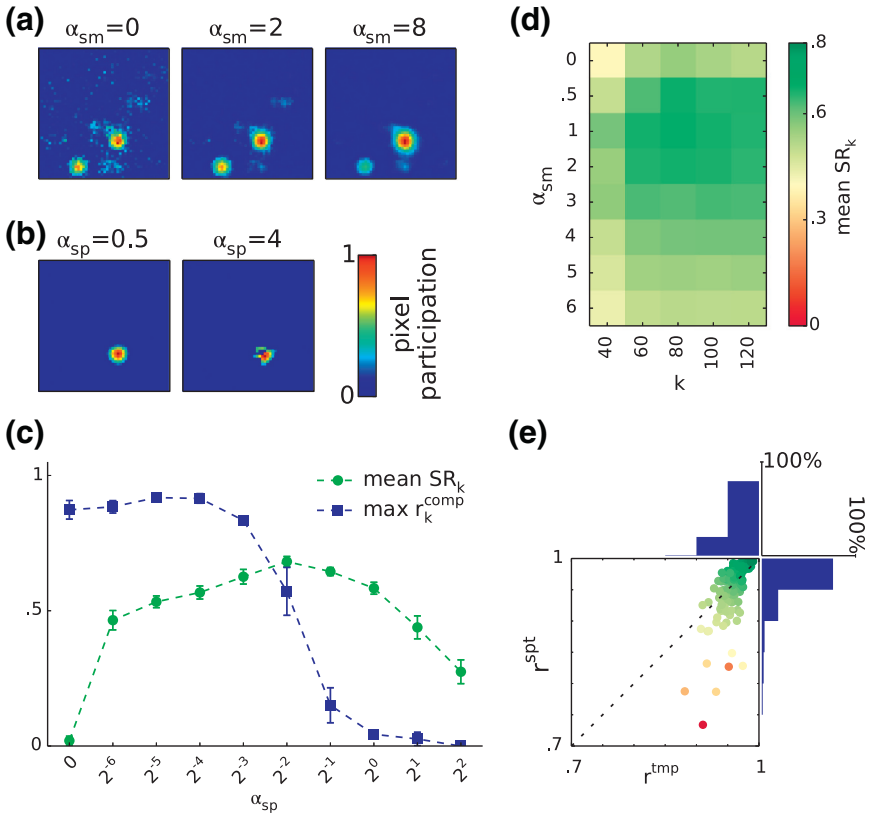

Fig. 2. Regularization parameter choice for surrogate data set ($n_{stim} = 50$, $\sigma_{noise} = 0.2$). (a) Effect of smoothness regularization parameter α_{sm} on an rNMF-extracted component ($k = 80$, $\alpha_{sp} = 0$). (b) Effect of sparseness regularization through α_{sp} on the rNMF component ($k = 80$, $\alpha_{sm} = 2$). (c) Maximal spatial component correlation r^{comp} and standard deviation for five different dataset instances (blue) respectively mean recovery SR_k (green) in dependence of α_{sp} ($k = 80$, $\alpha_{sm} = 2$). (d) Mean source recovery SR in dependence of number of components k and smoothness regularization α_{sm}. (e) Spatial and temporal correlation of matched components ($k = 80$, $\alpha_{sm} = 2$, $\alpha_{sp} = 0.5$) to 200 sources of five dataset instances. The color of each dot indicates the corresponding SR value (colorbar see (d)). Histograms on axes depict per-axis marginal distributions.

We next asked how sensitive the results are on the initial choice of smoothness regularization α_{sm} and number of components k. Setting $\alpha_{sp} = \alpha_{sp}^{opt}$ according to the above derived heuristic, the factorization performance was robust to the exact choice of k as long as it substantially exceeded the number of sources, *e.g.* by a factor of 1.5 to 3 (Fig. 2d). With respect to smoothness regularization the best results were obtained for values of α_{sm} between 0.5 and 2. This is a regime where most, but not all small scale structures are removed.

Taken together, we suggest the following heuristic to choose rNMF parameters: set the number of components k well above the number of expected sources (as a rule of thumb a factor of two), tune smoothness regularization to just remove most small scale structures and adjust sparseness regularization to just remove any strong component correlation.

With parameters corresponding to these heuristics ($k = 80$, $\alpha_{sm} = 2$, $\alpha_{sp} = \alpha_{sp}^{opt} = 0.5$) we obtained near optimal factorizations of the surrogate data with very good source recovery. This especially implied an extremely high temporal accuracy with 99.5% of components exhibiting a temporal correlation to their corresponding source higher than 0.9. Fig. 2e shows that for components with moderate source recovery values the temporal correlation to the source was always larger than 0.85.

Comparison of rNMF and sICA

Having demonstrated the benefits of appropriate regularization in rNMF, we next compare the performance of rNMF to that of conventional sICA on the surrogate data set. In sICA both spatial and temporal reconstruction of sources were more noisy, as already pointed out in the example above (*cf.* Fig. 1f). Due to the many but small non-local pixel participation values, the performance measure we used for rNMF might underestimate sICA's recovery performance compared to what could be achieved by simple post-processing like thresholding. To account for such post-processing and enable a fair comparison we only computed source recovery for localized sICA components ($sICA^{loc}$, see Materials and methods). Nonetheless $sICA^{loc}$ components showed significantly lower source recovery than rNMF components (Fig. 3a) ($p = 4 * 10^{-41}$, Kolmogorov–Smirnov test). This result was independent of the number of components k chosen to initialize the method (Fig. 3b). In particular, rNMF outperformed sICA regarding the reconstruction of the true time course of the sources, as measured by the temporal correlation r^{tmp} (Fig. 3c).

In general matrix factorization consists of the objective function to be optimized and the optimization procedure thereof. In FastICA the optimization procedure is further sub-divided in a first step of data reduction to k components *via* PCA and subsequent optimization of the component's independence. To better understand the particular influence of these steps we performed various sequential combinations of rNMF and sICA (see Materials and methods). Initializing rNMF with sICA components had no effect on recovery performance (Fig. 3d, sICA ini). In contrast, recovery was impaired when rNMF was applied on the data reconstruction from the sICA factorization (Fig. 3d, sICA dat). Since the sICA dat condition implies removing the part of the data that sICA reconstruction did not

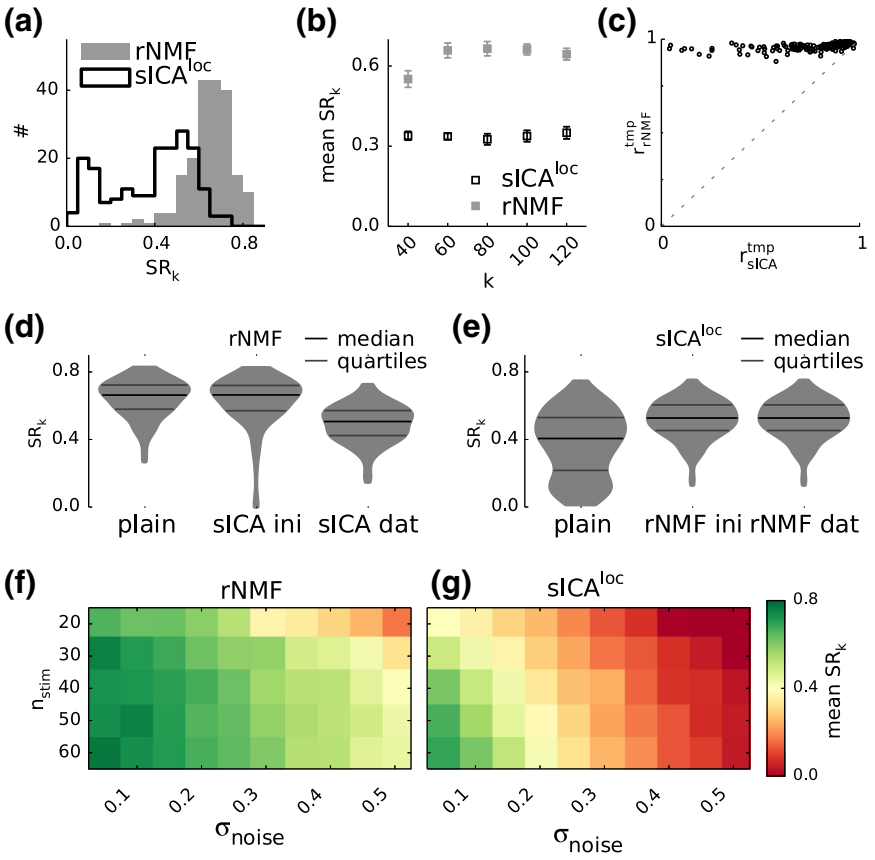

Fig. 3. Comparison of rNMF and sICA performance in source reconstruction. Data is pooled for five independently drawn surrogate datasets. (a) Histogram of source recovery values SR_k for rNMF (solid gray, $k = 80$, $\alpha_{sm} = 2$, $\alpha_{sp} = 0.5$) and localized sICA components $sICA^{loc}$ (black line, $k = 80$). (b) Dependence of mean source recovery SR_k on the number of components k in the surrogate data. (c) Temporal correlation of rNMF components $r^{tmp}{}_{rNMF}$ *vs.* $r^{tmp}{}_{sICA}$ of sICA components. (d,e) Violin plots of distribution on source recovery values SR_k for (d) plain rNMF, rNMF initialized with sICA components (sICA ini) and rNMF performed on sICA data reconstruction (sICA dat) and (e) for plain sICA, sICA performed on pixel participation of rNMF components (rNMF init) and sICA performed on rNMF data reconstruction (rNMF dat). (f,g) Mean source recovery SR_k in (f) rNMF and (g) $sICA^{loc}$ for different amounts of pixel noise σ_{noise} and number of stimuli used for dataset generation n_{stim}.

explain (the residual), this effect shows that in sICA part of the sparse signal is lost in the noise due to the variance driven dimensionality reduction of PCA. We also evaluated the reverse procedures, *i.e.* initializing sICA with rNMF pixel participations (Fig. 3e, rNMF ini), and performing sICA on rNMF reconstructions (Fig. 3e, rNMF dat). We found that both procedures improved the performance of plain sICA, showing that de-noising the data with rNMF is beneficial for sICA segmentation. On the other hand, the resulting sICA segmentation is worse than the results of the prior rNMF step, *i.e.* before applying sICA. This indicates that the objective function of rNMF better suits the source characteristics than the spatial independence objective of sICA.

Finally we asked how dataset statistics influenced the performance of rNMF and sICA.

In particular we asked to which extent the methods were affected by noise and the number of stimuli used for dataset generation (n_{stim}). Both rNMF and sICA performed well in low noise regimes and when the number of stimuli was larger than the number of sources (Figs. 3f, g). However, rNMF was more resilient to pixel noise and also coped better with the 'overcomplete' case when the number of stimuli n_{stim} was smaller than the number of sources (which was set to 40 in all examples). This result points out that the rNMF method is particularly suited to studying odor maps in the olfactory bulb with wide-field IOS imaging, when the expected number of sources (glomeruli) is in the same range or greater than the number of stimuli (unique odorants) used in one recording session.

In-vivo imaging data

The surrogate data provided insight into the application domain of the methods and yielded a heuristic for parameter choice. But experimentally obtained *in-vivo* IOS data is more complex than the surrogate data. With respect to spatial characteristics, glomeruli have varying sizes and shapes and also the exact spatial signal distribution is unknown. Furthermore the temporal characteristics of glomeruli do not obey an unique probability distribution but vary strongly in overall peak activation strength and odor selectivity (Nara et al., 2011).

Since IOS imaging alone doesn't reveal the ground truth regarding glomerulus locations, we performed 2-photon synaptopHluorin imaging of the resting fluorescence and obtained outlines of anatomical glomerulus positions (Fig. 4a). While the anatomical outlines naturally can't provide full information on the actual contribution of individual glomeruli to each pixel in the IOS recording, they do provide reliable information about glomerular position. The process of manual outlining and alignment of functional and anatomical measurements (Fig. 4b) may introduce a small error, complicating a 'hard' assessment of reconstruction quality. Nevertheless these outlines allowed for visual inspection of the match between anatomical glomerulus positions and extracted components.

We thus asked whether our general observations on the surrogate dataset still held for the IOS data. To answer this question, we

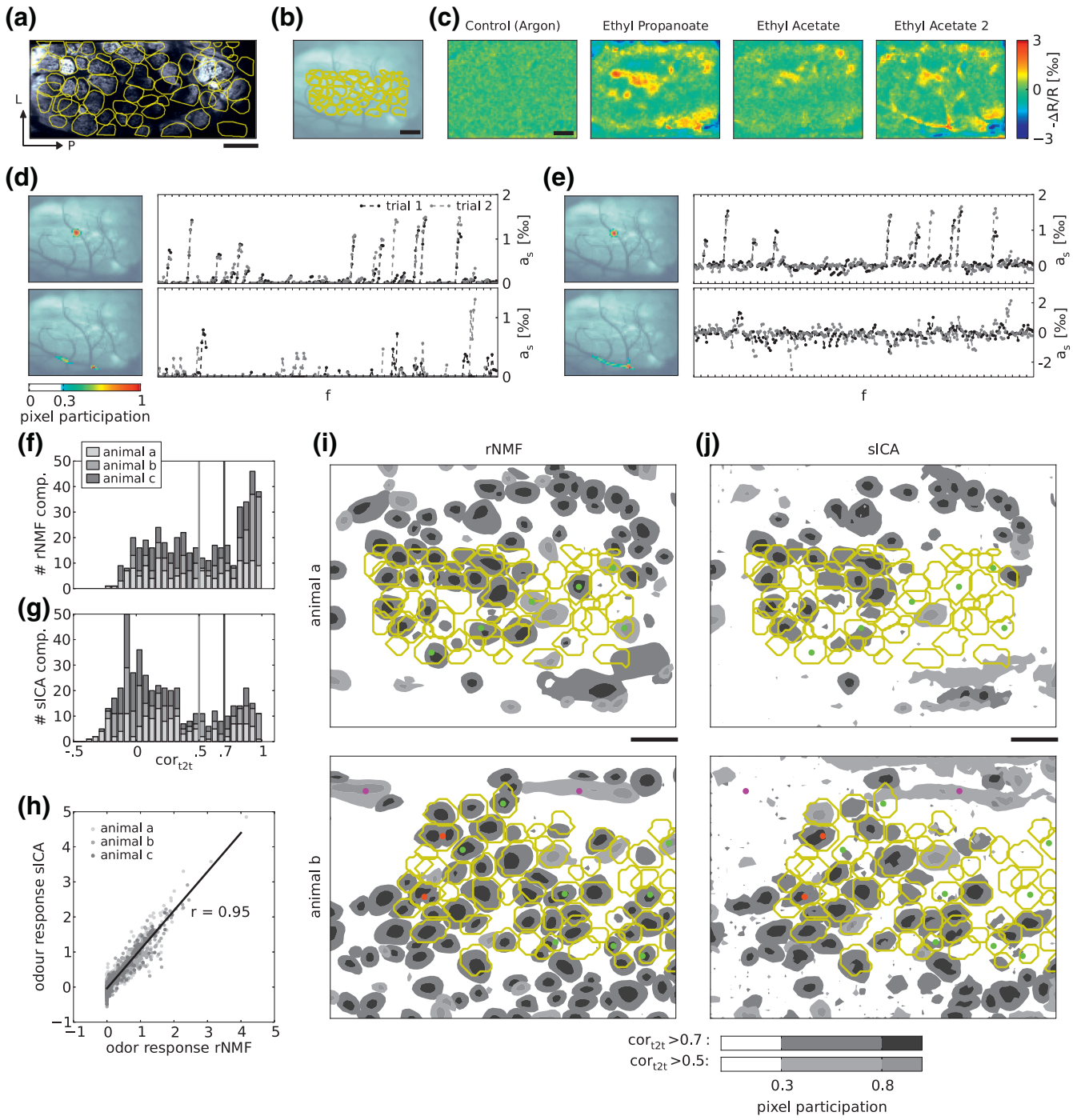

Fig. 4. Factorization of IOS mouse olfactory bulb imaging. (a) Z-frame of the synapto-pHluorin resting fluorescence image stack and manually outlined glomeruli (yellow contours, scale bar: 200 μm). (b) Glomerulus outlines (yellow) aligned to green image of the dorsal OB. (c) Examples of odor response maps obtained with IOS; mean $-\Delta R/R$ 6 s after odor delivery. (d) Two exemplary extracted rNMF components. Top: glomerulus-like component with localized activity (left panel) and high trial-to-trial correlation. Bottom: blood vessel-like component with low trial-to-trial correlation (right panel). (e) Similar components extracted by sICA. (f,g) Stacked histograms of observed trial-to-trial correlations of (f) rNMF and (g) sICA components. Vertical lines indicate thresholds for contour plots in (i,j). (h) Odor responses of reliably extracted glomeruli ($r^{t2t} > 0.7$) obtained by sICA *vs.* responses of matched glomeruli obtained by rNMF. (i) Contour plot of extracted pixel participation compared to anatomical glomerulus outlines (yellow) for rNMF in two animals. Black/dark gray contours indicate components with trial-to-trial correlation ($r_k^{t2t} > 0.7$), light gray contours correspond to components with $r_k^{t2t} > 0.5$. Green marks highlight glomeruli that only appeared in rNMF. Red marks highlight glomeruli better recovered in sICA. Magenta marks highlight components with $0.5 < r^{t2t} < 0.7$ that do not resemble glomeruli. (j) Same as (i) for sICA.

performed sICA and rNMF for three measurements (termed animal a, b, and c) according to our deduced heuristic. Both the pixel noise ($\sigma_{\text{noise}} = 0.15$ (animal a), $\sigma_{\text{noise}} = 0.15$ (animal b), $\sigma_{\text{noise}} = 0.19$ (animal c), estimated from the response to the 'non-odor' Argon) as well as the range of observed activations were in the range of the surrogate dataset (Fig. 4c).

We chose $k = 150$ to initialize rNMF and sICA, well above the estimated number of around 60 activated glomeruli.

In addition we set $\alpha_{sm} = 2$ in rNMF to avoid one-pixel scale structures and $\alpha_{sp} = 0.5$ to prohibit any component correlation above 0.5. In both rNMF and sICA we found some components that resembled glomeruli regarding their spatial extent and the activation course, while others looked like parts of blood vessels or measurement artifacts ('*noise*') (Figs. 4d,e). To distinguish putative glomerulus components from non-glomeruli we exploited the trial-to-trial correlation r_k^{t2t} of the components' odor spectra. The distributions of r_k^{t2t} values were roughly bimodal for both methods with a population of highly stimulus dependent components (Figs. 4f,g). Those stimulus dependent components exhibited good overlap with the anatomical outlines (Figs. 4i,j and Supplemental Fig. S1), taking into account the ambiguity of the outlines along the z-axis.

We made three observations: First, components with $r^{t2t} > 0.7$ corresponded well to anatomical glomerulus outlines. The same holds true for components with $0.5 < r^{t2t} < 0.7$ except in a few cases where components rather resembled blood vessels or other artifacts (magenta marks in Figs. 4i,j). Second, many glomeruli were detected by both methods, but some were solely extracted by rNMF (green marks in Figs. 4i,j) or exhibited higher trial-to-trial correlation r^{t2t} in rNMF than in sICA. Third, in rare cases we observed that two rNMF components were located within one anatomical outline (red marks in Figs. 4i,j) indicating different temporal activation of these parts, potentially due to underlying blood vessels or as an artifact of bandpass filtering.

In general these observations matched the results obtained using the surrogate dataset. rNMF yielded higher source recovery than sICA with a more precise temporal reconstruction, *i.e.* a higher trial-to-trial correlation. These results were robust over a range of parameter values (see Supplemental Fig. S2).

Finally, we asked whether the confinement of rNMF to positive activations had an effect on the extracted components compared to those extracted by sICA. To asses this we matched the most reliable components extracted with sICA ($r^{t2t} > 0.7$) to the respective rNMF component with which it exhibited the highest spatial correlation. The odor response spectra of the matched components were highly similar for both methods (Fig. 4h, $r = 0.95$). Furthermore, sICA extracted only a few and small negative signals which are not present in rNMF. Although this could indicate that our assumption of observing purely excitatory responses with IOS imaging has been mildly impaired, negative values in sICA might just as well be artifacts of the initial highpass filtering.

Discussion

In this study we demonstrated how to introduce prior knowledge about source characteristics through regularization in the NMF framework. We showed that regularized NMF outperformed standard sICA as a blind source separation approach for the automatic segmentation of glomeruli from IOS images of the olfactory bulb. We achieved this by reducing the approach's 'blindness' through incorporating knowledge about the spatial continuity and spatial separation of glomeruli. As a result of the regularization, the rNMF approach was more resilient to pixel noise and required fewer independent observations than sICA to reliably extract the locations and odor response spectra of individual glomeruli. Since the number of measurable stimuli is often restricted by experimental constraints, the reduced demand in stimulus number makes rNMF an interesting choice for other techniques with high signal-to-noise ratio, *e.g.* calcium sensitive dye imaging (Spors et al., 2006).

The combination of smoothness and sparseness regularization promoted factorizations in which observations were explained by neighboring pixels. In our case the almost two dimensional arrangement of glomeruli on the surface of the olfactory bulb justifies this approach. Nevertheless this assumption holds also in many 3D imaging scenarios like functional 2-photon imaging or fMRI. Moreover, tuning the introduced regularizations to the expected distribution of activity in the imaged tissue allows for a fine-grained adjustment of the methods' sensitivity in a broad range of applications.

We have demonstrated that the rNMF results remained stable over a wide range of parameters. But we also showed that regularization is absolutely necessary in NMF to obtain good results. Given a sufficiently large set of stimuli and/or low noise levels, sICA will also yield robust and fast segmentation, with no regularization parameters to tune. Hence, there is a tradeoff between the benefits of rNMF and the additional effort required for appropriate regularization.

In general sICA and NMF are closely related (in particular sparseness regulated NMF Hoyer, 2002, 2004). Therefore instead of alternating the basic NMF approach, one might also modify standard ICA to obtain a problem specific objective function. Indeed there exist numerous ICA variations addressing specific aspects of our regularization, *e.g.* non-negative ICA (Plumbley, 2003), sparse ICA (Babaie-Zadeh et al., 2006) spatio-temporal tomographic non-negative ICA (Valdés-Sosa et al., 2009) or overcomplete ICA (Lee et al., 1999). However, the sICA assumption of spatial independence is violated in our data set because the sources show partial overlap. The advantage of rNMF is that it allows the gradual adjustment of the spatial correlation of the segmented components to the expected spatial correlation of the true sources.

In general rNMF stands out by its straightforward implementation of constraints from prior knowledge. It allows for the addition or replacement of further modifications like temporal decorrelation or temporal smoothness and hence provides an opportunity to tailor factorization to known source statistics. While the assumption of non-negative responses in our data is in agreement with the literature (Nara et al., 2011) and our own results (see the *In-vivo* imaging data section), it is also straightforward to relax this assumption in the HALS algorithm by dismissing the rectification step (Cichocki and Anh-Huy, 2009). This would allow for negative source signals to be covered while still keeping the interpretability of non-negative pixel participations. Such an approach may prove useful to apply rNMF in cases where inhibitory signals are expected, such as using calcium imaging to measure odor maps in the insect antennal lobe (Sachse and Galizia, 2002).

The great flexibility in generating problem tailored factorization makes rNMF a promising approach for automated analysis in many functional imaging situations. In our case it facilitates an automatic and reliable high throughput investigation of chemical receptive fields of glomeruli in the mouse olfactory bulb.

Supplementary data to this article can be found online at http://dx.doi.org/10.1016/j.neuroimage.2014.04.041.

Acknowledgments

This work was supported by grants of Deutsche Forschungsgemeinschaft (MS: DFG SCHM2474/1-1, SCHM2474/1-2 (SPP 1392); HS: FOR 643, SP1134/1-1, SP1134/2-1 (SPP1392)). We thank Alexander Lehmann for sharing Matlab functions and Stephan Gabler for developing a graphical interface to the analysis method. We also thank Anna D'Errico, Martin Vogel, Thomas Rost and Joachim Haenicke for helpful discussions on the manuscript. We thank Jürgen Reichert and his team for excellent technical support, Christiane Kalmbach for electronic support, and Bolek Zapiec for IT support. We thank Peter Mombaerts for generous financial support, for providing infrastructure and resources for mouse breeding and genotyping, and for scientific discussions. We thank Prof. M. Nawrot for his general support and insightful comments.

Appendix A. Regularized NMF algorithm

Symbols are defined in the Materials and methods section. Additionally matrix $\mathbf{L}$ contains the neighborhood vector $\mathbf{l}_p$ of pixel p in it's pth row and $\hat{\mathbf{x}}_k^{\text{prev}}$ denotes the estimation of $\hat{\mathbf{x}}_k$ in the previous iteration.

Algorithm 1 regularized HALS

Initialize $\hat{\mathbf{A}}$ and $\hat{\mathbf{X}}$

$\mathbf{R} = \mathbf{Y} - \hat{\mathbf{A}}\hat{\mathbf{X}}$

repeat

  for $k = 1$ to K **do**

    $\mathbf{R} \leftarrow \mathbf{R} + \hat{\mathbf{a}}_k \hat{\mathbf{x}}_k^T$

    $\hat{\mathbf{x}}_k \leftarrow \frac{1}{1+\alpha_{\text{sm}}}[\mathbf{R}^T\hat{\mathbf{a}}_k - \alpha_{\text{sp}}\sum_{j\neq k}\hat{\mathbf{x}}_j + \alpha_{\text{sm}}\mathbf{L}\hat{\mathbf{x}}_k^{\text{prev}}]_+$

    $\hat{\mathbf{a}}_k \leftarrow [\mathbf{R}^T\hat{\mathbf{x}}_k]_+$

    $\hat{\mathbf{a}}_k \leftarrow \frac{\hat{\mathbf{a}}_k}{\|\hat{\mathbf{a}}_k\|_2^2}$

    $\mathbf{R} \leftarrow \mathbf{R} - \hat{\mathbf{a}}_k \hat{\mathbf{x}}_k^T$

  end for

until convergence criterion is reached.

Appendix B. Initialization

Initialization procedure for $\hat{\mathbf{A}}$ and $\hat{\mathbf{X}}$. $\mathbf{r}_p$ denotes the pth row of matrix $\mathbf{R}$ and therefore the residual time-course of pixel p.

Algorithm 2 Init

$\mathbf{R} = \mathbf{Y}$

for $k = 1$ to K **do**

  $\tilde{p} \leftarrow \text{argmax}_p \|\mathbf{r}_p\|_\infty$

  $\hat{\mathbf{a}}_k \leftarrow \mathbf{r}_{\tilde{p}}$

  $\hat{\mathbf{a}}_k \leftarrow \frac{\hat{\mathbf{a}}_k}{\|\hat{\mathbf{a}}_k\|_2^2}$

  $\hat{\mathbf{x}}_k \leftarrow [\mathbf{R}^T\hat{\mathbf{a}}_k]_+$

  $\mathbf{R} \leftarrow \mathbf{R} - \hat{\mathbf{a}}_k \hat{\mathbf{x}}_k^T$

end for

References

Babaie-Zadeh, M., Jutten, C., Mansour, A., 2006. Sparse ICA via cluster-wise PCA. Neurocomputing 69 (13–15), 1458–1466.

Bathellier, B., Van De Ville, D., Blu, T., Unser, M., Carleton, A., 2007. Wavelet-based multiresolution statistics for optical imaging signals: application to automated detection of odour activated glomeruli in the mouse olfactory bulb. NeuroImage 34 (3), 1020–1035.

Belluscio, L., Katz, L.C., 2001. Symmetry, stereotypy, and topography of odorant representations in mouse olfactory bulbs. J. Neurosci. 21 (6), 2113–2122.

Bozza, T., McGann, J.P., Mombaerts, P., Wachowiak, M., 2004. In vivo imaging of neuronal activity by targeted expression of a genetically encoded probe in the mouse. Neuron 42 (1), 9–21.

Chen, Z., Cichocki, A., 2005. Nonnegative matrix factorization with temporal smoothness and/or spatial decorrelation constraints. Technical Report, Laboratory for Advanced Brain Signal Processing, RIKEN, pp. 1–10.

Cichocki, A., Anh-Huy, P., 2009. Fast local algorithms for large scale nonnegative matrix and tensor factorizations. IEICE Trans. Fundam. Electron. Commun. Comput. Sci. E92-A (3), 708–721.

Donoho, D., Stodden, V., 2004. When does non-negative matrix factorization give a correct decomposition into parts? In: Thrun, S., Saul, L., Schölkopf, B. (Eds.), Advances in Neural Information Processing Systems, 16. MIT Press, Cambridge, MA.

Dorostkar, M.M., Dreosti, E., Odermatt, B., Lagnado, L., 2010. Computational processing of optical measurements of neuronal and synaptic activity in networks. J. Neurosci. Methods 188 (1), 141–150.

Firestein, S., 2001. How the olfactory system makes sense of scents. Nature 413 (6852), 211–218.

Grinvald, A., Shoham, D., Shmuel, A., Glaser, D., Vanzetta, I., Shtoyerman, E., Slovin, H., Wijnbergen, C., Hildesheim, R., Arieli, A., 1999. In-vivo optical imaging of cortical architecture and dynamics. In: Windhorst, U., Johansson, H.K. (Eds.), Modern Techniques in Neuroscience Research. Springer, Berlin Heidelberg, pp. 893–969.

Gurden, H., Uchida, N., Mainen, Z.F., 2006. Sensory-evoked intrinsic optical signals in the olfactory bulb are coupled to glutamate release and uptake. Neuron 52 (2), 335–345.

Hoyer, P.O., 2002. Non-negative sparse coding. Proceedings of the 12th IEEE Workshop on Neural Networks for Signal Processing. IEEE. IEEE, pp. 557–565.

Hoyer, P.O., 2004. Non-negative matrix factorization with sparseness constraints. J. Mach. Learn. Res. 5, 1457–1469.

Hyvärinen, A., 1999. Fast and robust fixed-point algorithms for independent component analysis. IEEE Trans. Neural Netw. 10 (3), 626–634.

Lee, T.-W., Lewicki, M., Girolami, M., Sejnowski, T., 1999. Blind source separation of more sources than mixtures using overcomplete representations. IEEE Signal Process. Lett. 6 (4), 87–90.

Ma, L., Qiu, Q., Gradwohl, S., Scott, A., Yu, E.Q., Alexander, R., Wiegraebe, W., Yu, C.R., 2012. Distributed representation of chemical features and tunotopic organization of glomeruli in the mouse olfactory bulb. Proc. Natl. Acad. Sci. U. S. A. 109 (14), 5481–5486.

Meister, M., Bonhoeffer, T., 2001. Tuning and topography in an odor map on the rat olfactory bulb. J. Neurosci. 21 (4), 1351–1360.

Mukamel, E.A., Nimmerjahn, A., Schnitzer, M.J., 2009. Automated analysis of cellular signals from large-scale calcium imaging data. Neuron 63 (6), 747–760.

Murthy, V.N., 2011. Olfactory maps in the brain. Annu. Rev. Neurosci. 34, 233–258.

Nara, K., Saraiva, L.R., Ye, X., Buck, L.B., 2011. A large-scale analysis of odor coding in the olfactory epithelium. J. Neurosci. 31 (25), 9179–9191.

Nelsen, R.B., 1998. An Introduction to Copulas, 1st edition. Springer, New York.

Pain, F., L'heureux, B., Gurden, H., 2011. Visualizing odor representation in the brain: a review of imaging techniques for the mapping of sensory activity in the olfactory glomeruli. Cell. Mol. Life Sci. 68 (16), 2689–2709.

Pedregosa, F., Varoquaux, G., Gramfort, A., Michel, V., Thirion, B., Grisel, O., Blondel, M., Prettenhofer, P., Weiss, R., Dubourg, V., Vanderplas, J., Passos, A., Cournapeau, D., Brucher, M., Perrot, M., Duchesnay, E., 2011. Scikit-learn: machine learning in Python. J. Mach. Learn. Res. 12 (Oct), 2825–2830.

Plumbley, M.D., 2003. Algorithms for nonnegative independent component analysis. IEEE Trans. Neural Netw. 14 (3), 534–543.

Reidl, J., Starke, J., Omer, D.B., Grinvald, A., Spors, H., 2007. Independent component analysis of high-resolution imaging data identifies distinct functional domains. NeuroImage 34 (1), 94–108.

Royet, J.P., Souchier, C., Jourdan, F., Ploye, H., 1988. Morphometric study of the glomerular population in the mouse olfactory bulb: numerical density and size distribution along the rostrocaudal axis. J. Comp. Neurol. 270 (4), 559–568.

Rubin, B.D., Katz, L.C., 1999. Optical imaging of odorant representations in the mammalian olfactory bulb. Neuron 23 (3), 499–511.

Sachse, S., Galizia, C.G., 2002. Role of inhibition for temporal and spatial odor representation in olfactory output neurons: a calcium imaging study. J. Neurophysiol. 87 (2), 1106–1117.

Soucy, E.R., Albeanu, D.F., Fantana, A.L., Murthy, V.N., Meister, M., 2009. Precision and diversity in an odor map on the olfactory bulb. Nat. Neurosci. 12 (2), 210–220.

Spors, H., Grinvald, A., 2002. Spatio-temporal dynamics of odor representations in the mammalian olfactory bulb. Neuron 34 (2), 301–315.

Spors, H., Wachowiak, M., Cohen, L.B., Friedrich, R.W., 2006. Temporal dynamics and latency patterns of receptor neuron input to the olfactory bulb. J. Neurosci. 26 (4), 1247–1259.

Strauch, M., Galizia, C.G., 2012. Fast PCA for processing calcium-imaging data from the brain of *Drosophila melanogaster*. BMC Med. Inform. Decis. Mak. 12 (Suppl. 1), S2.

Strauch, M., Rein, J., Galizia, C.G., 2012. Signal extraction from movies of honeybee brain activity by convex analysis. Computational Advances in Bio and Medical Sciences (ICCABS), 2012 IEEE 2nd International Conference on. IEEE, pp. 1–6.

Valdés-Sosa, P.A., Vega-Hernández, M., Sánchez-Bornot, J.M., Martínez-Montes, E., Bobes, M.A., 2009. EEG source imaging with spatio-temporal tomographic nonnegative independent component analysis. Hum. Brain Mapp. 30 (6), 1898–1910.

Wachowiak, M., Cohen, L.B., 2001. Representation of odorants by receptor neuron input to the mouse olfactory bulb. Neuron 32 (4), 723–735.

Wachowiak, M., Cohen, L.B., 2003. Correspondence between odorant-evoked patterns of receptor neuron input and intrinsic optical signals in the mouse olfactory bulb. J. Neurophysiol. 89 (3), 1623–1639.

Supplemental Material

Supplemental Movie M1

This movie shows 3D stack of resting synaptho-pHluorin fluorescence in the dorsal bulb. Yellow contours show hand drawn outlines of glomeruli on the surface.

Supplemental Table T1

List of odours which were presented to the animals.

Odour	CAS	Odour	CAS
Isopropyl ethanoate	108-21-4	Ethyl hexanoate	123-66-0
Isobutyl propanoate	540-42-1	3-Hexanone	589-38-8
Citronellal	106-23-0	2,3-Heptadione	96-04-8
Isobutyl ethanoate	110-19-0	Isobutyl formate	542-55-2
1,2-Propandione	78-98-8	Prop-2-enyl ethanoate	591-87-7
2-Pentanone	107-87-9	(R)-(+)-Pulegone	89-82-7
Propyl ethanoate	109-60-4	Methyl 2-methylbut-2-enoate	6622-76-0
3-Methylbutanal	590-86-3	Prop-2-enyl propanoate	2408-20-0
2,3-Hexadione	3848-24-6	2,3-Pentanedione	600-14-6
Butanethiol	109-79-5	Methyl butanoate	623-42-7
Propyl propanoate	106-36-5	Methyl ethanoate	79-20-9
Ethyl pentanoate	539-82-2	Methyl benzoate	93-58-3
Ethanal	75-07-0	Methyl propanoate	554-12-1
2-Methyl-pent-2-enal	623-36-9	Ethyl propanoate	105-37-3
Phenylethanol	60-12-8	2,3-Butandione	431-03-8
1,4-Cineole	470-67-7	Butyl ethanoate	123-86-4
Pentyl ethanoate	628-63-7	Butyl propanoate	590-01-2
(-)-Geosmin	19700-21-1	2-Ethyl-3-methoxy pyrazine	25680-58-4
Prop-2-enyl 2-methylbut-2-enoate	7493-71-2	Ethyl 2-methylbutyrate	7452-79-1
Hex-2-enyl ethanoate	2497-18-9	Ethyl 2-mercapto propanoate	19788-49-9
Ethyl prop-2-enoate	140-88-5	Ethyl ethanoate	141-78-6
Paraldehyde	123-63-7	Diethyl carbonate	105-58-8
Diethyl oxalate	95-92-1	Methyl prop-2-enyl carbonate	35466-83-2
Argon	14320-37-7		

Supplemental Figure S1

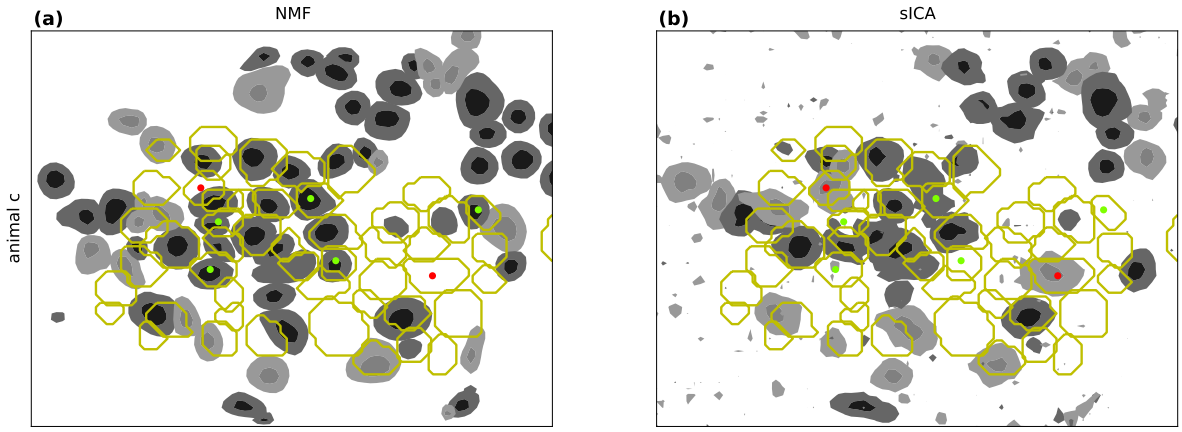

Figure S1: Same illustration as in Figure 4(i,j) for animal c. Contour plots of pixel participation for stimulus driven components ($r_k^{\mathrm{t2t}} > 0.5$) and highly stimulus driven components ($r_k^{\mathrm{t2t}} > 0.7$) compared to anatomical outlined glomeruli (yellow) for (a) NMF and (b) sICA. Green marks indicate glomeruli solely recovered in NMF whereas red marks show glomeruli better recovered in sICA.

Supplemental Figure S2

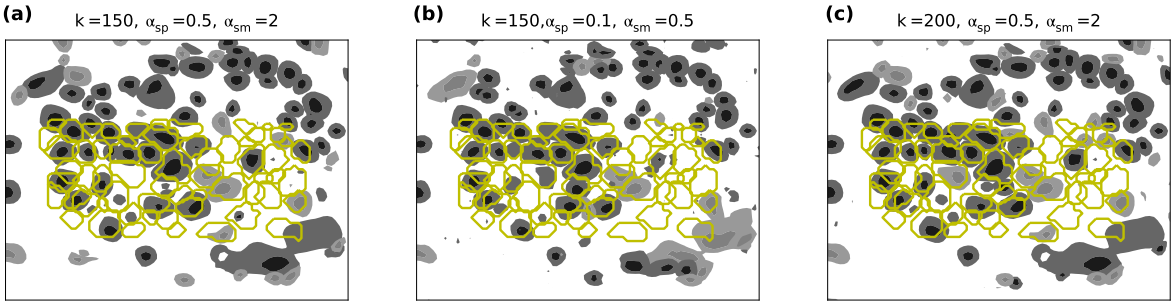

Figure S2: Example for NMF parameter dependence. In spite of some small differences the factorization generally delivers robust results over the parameter range. (a) NMF for animal a using the same parameters as in the main document, (b) NMF with lower smoothness regularisation $\alpha_{\mathrm{sm}} = 0.5$ and hence lower $\alpha_{\mathrm{sp}}^{\mathrm{opt}} = 0.1$. (c) NMF with increased number of components k.

Chapter 3

Physicochemical vs. Vibrational Descriptors for Prediction of Odor Receptor Responses

Stephan Gabler[*1,2], *Jan Soelter*[*1], *Taufia Hussain*[4], *Silke Sachse*[4] *and Michael Schmuker*[1,2]

* These authors contributed equally to this work

This chapter is published in Molecular Informatics 2013, Volume 32, pages 855-865
You can find it at http://dx.doi.org/10.1002/minf.201300037

Profiling the role of receptor MOR18-2 in the olfactory code

Jan Soelter[a], Jan Schumacher[b], Hartwig Spors[b], Michael Schmuker[a,c,*]

[a] *Neuroinformatics & Theoretical Neuroscience, Institute of Biology, Freie Universität Berlin, Germany*
[b] *Max-Planck Institute for Biophysics, Frankfurt am Main, Germany*
[c] *Bernstein Center for Computational Neuroscience Berlin, Germany*

Abstract

In contrast to most sensory systems, receptive ranges in the olfactory system are still awaiting to be thoroughly determined. In this study we took a step in this direction and profiled the receptive range of the olfactory receptor MOR18-2 and evaluated its relation to the receptive fields of other receptors. To this end we imaged odour responses of the dorsal olfactory bulb (dOB) with an emphasis on ligands of MOR18-2. We obtained an extensive response spectrum of MOR18-2 with its ligands being mainly small esters. It showed that some of those ligands are shared with spatially proximal glomeruli such that MOR18-2 glomeruli are embedded in a local tunotopic response domain.

Furthermore we derived a description of the MOR18-2 receptive range in terms of physicochemical properties. With regard to those properties we observed a weak chemotopic embedding of MOR18-2 in a lateral-posterior domain of the dOB.

1. Introduction

For most sensory systems the receptive fields of individual sensory neurons are fairly well identified and the principles by which neurons are topographically arranged across the neural sheets could be revealed (e.g. retinotopy in vision, tonotopy in audition, somatopy in somatosensation) (Imig and Morel, 1983; Grill-Spector and Malach, 2004; Kaas, 1991). In contrast, for the olfactory sense our knowledge on the sensory mapping is less complete concerning both molecular receptive ranges (MRRs) of individual olfactory sensory neurons (OSNs) as well as their functional arrangement (Peterlin et al., 2014).

Among the best explored olfactory systems is the main olfactory system of mice. It comprises of a large variety of OSNs, each of them expressing only a single receptor gene out of a repertoire of $\sim$ 1000 genes from three classes ($\sim$ 150 class 1 ORs, $\sim$ 900 class 2 ORs and 14 TAARs) (Zhang and Firestein, 2002; Liberles and Buck, 2006). Notably the different receptors are mostly not labelled lines for specific molecules, but in general each receptor is activated by a range of molecules and each molecule activates an ensemble of receptors (Malnic et al., 1999).

*Corresponding author.
Email: m.schmuker@fu-berlin.de
Phone: +49 (0) 30 838 57294

Each receptor is expressed in restricted zones along the dorsomedial-ventrolateral axis of the main olfactory epithelium (OE), but the zones of different receptors are strongly overlapping. Thus OSNs of different receptor types and even receptor classes are strongly intermingled in the OE (Miyamichi et al., 2005; Pacifico et al., 2012). It is only in the olfactory bulb (OB), the first relay station of the olfactory pathway, the sensory array becomes demixed. OSNs of the same receptor type converge to distinct neuropil, called glomeruli, that are exclusively innervated by those OSNs (Mombaerts et al., 1996). The glomeruli are arranged side by side on a spherical surface with a stereotypic position relating to their receptor type (Soucy et al., 2009). Furthermore glomeruli corresponding to each of the three receptor classes are mainly segregated into separate domains (Pacifico et al., 2012). Thereby glomeruli positions reflect the dorsomedial-ventrolateral axis of OE receptor expression in a corresponding dorso-ventral arrangement (rhinotopy) (Miyamichi et al., 2005).

All in all the OB embodies a two dimensional topographical representation of the stimulus induced receptor repertoire activation. But to which extent this layout implies a functional logic is still under debate (Matsumoto et al., 2010; Soucy et al., 2009; Ma et al., 2012). Two notions of functional similarity for proximal glomeruli are frequently discussed: First the degree of overlap of their ligand spectra per se and second chemical similarity thereof. Adhering to Ma et al., in the following we denote the former as tunotopy and the latter as chemotopy. Note that there is no generic definition of chemical similarity and thus has to be first defined (Saito et al., 2009; Haddad et al., 2008).

A more general problem in evaluating the functional layout of the OB lies in the experimental limitation in the size of the employed odour set. Typically they do not exceed the order of one hundred odours, and hence only provide a tiny snapshot of the olfactory world. Therefore studies often have to rely on only fragmentary obtained MRRs. Detailed MRRs are only available for an exiguous amount of receptors (Li et al., 2012; Baud et al., 2010; Katada et al., 2005; Araneda et al., 2000) and partial MRRs merely for a few more (Repicky and Luetje, 2009; Grosmaitre et al., 2009; Oka et al., 2006; Bozza et al., 2002; Abaffy et al., 2006; Saito et al., 2009; Bautze et al., 2012).

In this study we determined in detail the MRR of the glomeruli corresponding to the class 1 receptor MOR18-2 (aka MOL2.3). Based on this knowledge we then investigated the glomerular layout in a novel way: Instead of investigating the topographic relationship of many glomeruli with fragmentary MRR, we evaluated the topographic embedding of this single receptor with respect to its 'full' MRR.

Furthermore, in a first step to evaluate chemotopic embedding, we obtained a physico-chemical activation model of MOR18-2. That is, instead of describing its receptive field by the listing of activating odours, we specified its activating range within a space of physico-chemical properties. Finally we compared placement within this space to spatial position on the dOB.

2. Methods

2.1. Imaging

Mice were anaesthetized using urethane (1.5g/kg i.p.). Anaesthetic was supplemented throughout the experiments and the body temperature was kept between 36.5C and 37.5C using a heating pad and a rectal probe. For imaging a craniotomy over one or both olfactory bulb were cut. The dura mater was removed and the imaging chamber was filled with agar (1.5%) and covered with a glass cover slip. The prepared skull was fixated with cement to a metal plate under the microscope. All animal care and procedures were in accordance with the animal ethics guidelines of the Max Planck Society.

Odours were presented with a two armed robot (Combipal, CTC-Analytics, Zwingen, Switzerland) using the Software Chronos (Axel Semrau, Sprockhoevel, Germany). 2.5ml of the odour headspace was injected into a constant carrier flow of filtered and humidified air (2l/min) towards the mouse's nose. Odour molecules reached the nose 2.5 ± 0.3s after recording onset as measured by a photoionization detector (Aurora Scientific, Canada). After each odour presentation the syringe used for odour transfer was flushed with nitrogen for 72s to minimize contamination. We measured different stimuli set of 4 to 53 odours in 78 MOL2.3-IGITL mice (Conzelmann et al., 2000), 3 heterozygote OMP-SpH mice (Bozza et al., 2004) and 15 heterozygote MOL2.3-IGITL OMP-Sph cross-breeds. Thereby each stimulus set was at least measured twice in each mice with odours presented in a pseudo-randomized sequence.

Intrinsic Optical Signal (IOS) Imaging

Odour responses were recorded in the dorsal olfactory bulb for 12s at 5Hz using a macroscope (Pentax zoom lens 12-48 mm, f = 1:1.0 and Nikkor lens 135 mm, f = 1:2.0) and an Orca-R2 camera (Hamamatsu, Japan; 1024×1344px) under illumination with red light (690nm). Unilateral OB recordings were performed at a focal distance of 24 mm (field of view 1.63mm $\times$ 1.24mm), whereas bilateral recordings were performed at a distance of 48 mm (field of view $3.26\text{mm} \times 2.48\text{mm}$). Before and after each presentation of the entire stimulus set, the pattern of blood vessels was recorded using green illumination (546nm, 'green image') and controlled for shifts to exclude movement artefacts. Furthermore the locations of MOR18-2 glomeruli were made visible by blue illumination (475nm, 'GPF image') and an emission filter at 535nm.

To increase signal-to-noise ratio and reduce computational load we binned the raw data with an 8×8px spatial and a 12 frame temporal window. Then the odour induced activation was calculated as the relative decrease of reflectance $-\Delta R/R = -(R - R_0)/R$. R_0 was the mean reflectance on the first 2s after recording onset, well before the odours reached the nose (see above). Furthermore the data was spatially bandpass filtered with two Gaussian filters ($\sigma_{\text{low}} = 10$px, $\sigma_{\text{high}} = 1$px) and down-sampled by a factor of 2. The final resolution of the measurement time series was thus 64×84px at 0.42Hz. The concatenation of the preprocessed frames for all odours lead to the measurement matrix $\mathbf{Y} \in R^{F \times P}$ with element $Y_{f,p}$ being the observed value of the p^{th} pixel in the f^{th} frame.

Synapto-pHluorin (SpH) Imaging

Synapto-pHluorin imaging was performed with a 2-photon laser scanning microscope (Prairie Technologies, Middleton, TN, USA), a 16x water immersion objective (N.A. 0.8, Nikon, back aperture overfilled) and a MaiTai DeepSee laser (50-170mW, tuned to 880nm, 80 MHz repetition rate of pulses 120fs in length; Spectra-Physics/Newport, Santa Clara, CA, USA). Emitted light was separated and recorded into a green 525nm and red 607nm channel.

Functional imaging (128 x 128 pixel, $5.02\mu m$/pixel) was performed for each odour 12.77s with 94 Hz at a fixed z-position. To increase signal-to-noise ratio and reduce computational load we binned the raw data with a 120 frame temporal window. Then the odour induced activation was calculated as the increase in fluorescence $F - F_0$. F_0 was the mean fluorescence on the first 2s after recording onset. Furthermore the data was low pass filtered (Gaussian filter $\sigma = 1.5$px) and down-sampled by a factor of 2 to suppress pixel noise. The final resolution of the measurement matrix $\mathbf{Y}$ was thus 64×64px at 0.94Hz. To account for bleaching effects the same procedure was applied to control measurements without any odour stimulation. Out of these we calculated for each pixel the mean bleaching time course and subtracted those from the pixels' odour responses time courses.

Before and after functional imaging we acquired anatomical images (512 x 512 pixel, $1.25\mu m$/pixel) at 3μm steps in z-direction. After functional imaging the mice were first killed by an overdose of urethane. Subsequently the OB was stained by Fast Red Violet (FRV) before anatomical images were obtained. This made MOR18-2 glomeruli visible in the red channel (607nm, 'FRV image')

2.2. Glomerular response spectra

We segmented the functional image series into individual glomeruli and their activation course by means of regularized non-negative matrix factorization (rNMF) (Soelter et al., 2014). Such a factorization disaggregates the measurement matrix $\mathbf{Y}$ into k components with a spatial signal distribution $\mathbf{x}_k$ and a common activation course $\mathbf{a}_k$ of the participating pixel. The factorization contained spatial smoothness (governed by parameter α_{sm}) and sparseness regularization (α_{sp}) to promote a disaggregation into spatial distinct but possibly overlapping components, i.e. glomeruli arranged side by side with an overlapping signal distribution.

We decomposed IOS image series into 150 components with fixed smoothness regularization parameter $\alpha_{\mathrm{sm}} = 2$. The sparseness regularization parameter α_{sp} was adjusted such that spatial component correlation was just below 0.5 (Soelter et al., 2014). In image analysis performed to extract MOR18-2 responses, we dismissed the usual non-negativity constraint on the components' activation courses to capture possible odour induced inhibitions. In contrast, in analysis to extract response spectra across the full dOB we kept the non-negativity constraint as it increased the trial-to-trial correlation of response spectra.

SpH image series were disaggregated by the same approach. With respect to the reduced field of view, the factorization was performed only into 20 components with an extended smoothness regularization of $\alpha_{\mathrm{sm}} = 5$.

Odour responses a_k^o of each component k (e.g. glomeruli) were obtained by averaging the activation of frames 3 and 4 in IOS (4.8−9.6s after recording onset) and frames 8-11 (6.6−10.3s) in SpH measurements. All odour responses of a measurement composed the components response spectrum $\mathbf{s}_k = (a_k^{o1}, \ldots, a_k^{oN})$. To sort out non glomerular components of the factorization, we only took components into account that exhibited a trial-to-trial correlation above 0.6 between response spectra of odour set repetitions within an animal (Soelter et al., 2014).

Components were manually assigned as MOR18-2 glomeruli if their pixel participation matched the GFP marked location of MOR18-2. Since the overall response strength varied strongly across animals we normed MOR18-2 responses to its Methyl propionate (MP) response in the same measurement ($a_{\text{relMP}} = a/a^{\text{MP}}$). The final odour response was than computed as the median response of all measured animals, in which sufficient strong responses were observed ($a^{\text{MP}} > 0.2‰$)

To evaluate similarity of glomerular response spectra we computed the pairwise correlation distance $d_r = 1 - r(\mathbf{s}_j, \mathbf{s}_k) = \sum_o (a_j^o - \langle a_j \rangle_o)(a_k^o - \langle a_k \rangle) / \sqrt{\sum_o (a_j^o - \langle a_j \rangle_o)^2 \sum_o (a_k^o - \langle a_k \rangle_o)^2}$. Based on this distance we obtained a hierarchical clustering by the UPGMA method and evaluated cluster at different thresholds. We manually set thresholds to obtain clusters with distinct gaps between them. Thereby we restricted cluster to contain at least glomeruli of three different animals. To account for varying overall response strength across animals we normalized all responses to unit length response spectra $a_{\text{norm}}^o = a^o / \|\mathbf{s}\|$.

2.3. Physico-chemical characterization

For all measured molecules we obtained 3d structures via Pubchem. We managed the structures using ChemAxon Instant JChem (version 5.9.4, 2012, http://www.chemaxon.com) and standardized them by its Clean3d function. For all molecules we computed the 1600 descriptors of 19 descriptor blocks in eDragon (all blocks except Information Indices) (Tetko et al., 2005). Furthermore we computed the EVA descriptors (Turner and Willett, 2000; Gabler et al., 2013) . To this end we optimized structures and computed vibrational frequencies in the GAUSSIAN software package using the B3LYP method and the 6-311G(d,p) basis set. Afterwards the vibration spectra were mapped to a continuous range [0,4000 cm^{-1}] by placing a Gaussian kernel of unit height and varying width $\sigma \in \{1, 5, 10, 20, 50, 100\}$ on each frequency. The final descriptors sets EVA_σ^q were then generated by sampling from this spectrum from $q = 0$ to $q = 4000$ in intervals of σ. For individual descriptors x as well as descriptor sets $\mathbf{x}$ we fitted activation models $\hat{a} = f(x)$ to match the observed odour activations a^o. We evaluated goodness of fit by calculating the coefficient of determination $R^2 = 1 - \sum_o (a^o - \hat{a}^o)^2 / \sum_o (a^o - \langle a \rangle_o)^2$ over all odors o. Whereas this measure assessed how well the data could be described by a model, it does not reflect that sufficient complex models could perfectly fit any functional relationship of the data without the ability to generalize to unseen data. Therefore we also evaluated the coefficient of determination for unseen data in a bootstrap approach (Consonni et al., 2009). To this end, we fitted each model on 50 bootstrap samples b_i of the data and obtained predictions of odour activations $\hat{a}^o$ not contained in the bootstrap sample. We then calculated the predictive power as $q^2 = 1 - \sum_{b_i} \sum_{o \notin b_i} (a^o - \hat{a}^o)^2 / \sum_{b_i} \sum_{o \notin b_i} (a^o - \langle a \rangle_o)^2$. We evaluated the performance

of univariate linear regressions, isotonic regression and unimodal isotonic regression (Härdle, 1989) and multivariate Support Vector Regression (SVR) with Gaussian Kernel (Bishop et al., 2006). All models were obtained via the scikit-learn module using default parameters (Pedregosa et al., 2011). Scikit-learn was also employed to obtain the Multidimensional Scaling (MDS) of odour space distances. Prior of fitting SVR and MDS models we normalized all descriptors to zero mean and unit variance with respect to our in-house library of about 1000 odours.

We also employed normalized descriptors to obtain glomerular position in chemical space. To this end we assigned each glomerulus its barycenter of activation $\mathbf{x}^k = \sum_o (a^o_{\text{norm}} \mathbf{x}_o) / \sum_o a^o - \langle \mathbf{x} \rangle_o$ relative to the mean descriptor value $\langle \mathbf{x} \rangle_o = \sum_o x_o / N$ for all odours in the measurement set. We then calculated the pairwise cosine distance $d_{\cos} = 1 - \cos(\mathbf{x}_j, \mathbf{x}_k) = 1 - \mathbf{x}_j \mathbf{x}_k / \|\mathbf{x}_j\| / \|\mathbf{x}_k\|$ of the barycenters and obtained a hierarchical clustering thereof by the UPGMA method.

3. Results

The aim of this study was to investigate the MRR of the MOL2.3 receptor and its embedding in the glomerular ensemble code. To address these aspects we performed Intrinsic Optical Signal (IOS) imaging of the dorsal olfactory bulb (dOB, Fig. 1a) under stimulation with monomolecular odors in MOR18-2-IGITL mice (Conzelmann et al., 2000). The IOS allowed for measuring odor response of all glomeruli in the dOB (Fig. 1b) while the GFP-labelling of the MOR18-2 OSNs enabled localization of the corresponding glomeruli (Fig. 1c). To extract glomerular responses from the IOS we first band-passed the data to suppress pixel noise and separate the glomerular signal from the global unspecific signal (Meister and Bonhoeffer, 2001). We then performed regularized Matrix Factorization (rNMF) to obtain a decomposition of the image series into overlapping signals from neighbouring glomeruli (Fig. 1d, see methods and (Soelter et al., 2014)) and thus avoided a corruption of glomerular response by signal spillover.

3.1. Molecular receptive range

To obtain the MRR of MOR18-2 as complete as possible, we tried to determine a large number of ligands. After discovering the first ligand (Methyl propionate) by screening odors known to activate glomeruli in the dorsal bulb, we iteratively built hypotheses for further ligands based on the present set of revealed ligands. We acquired those hypotheses both empirically by our intuitive notion of chemical similarity (e.g. chain length, bond saturation) and automated by virtue of virtual screening (Boyle et al., 2013; Schmuker et al., 2007). Overall in this process we acquired the response to 214 odors from measurements of 41 animals.

The ligand spectrum of MOR18-2 showed a narrow range of strongly activating odors (Fig. 1d). Figure 1e depicts the ligand spectrum, containing the most active ligands as well as some related non-activating molecules. It shows that MOR18-2 was most sensitive to small aliphatic esters, with some medium response to small aldehydes/dialdehydes. We also observed some small, but significant negative responses (Fig. 1d) which may indicate some inhibitory responses. However, we can not exclude that inhibitory responses artificially were induced by positive activations of neighbouring glomeruli in the preprocessing step of bandpass filtering.

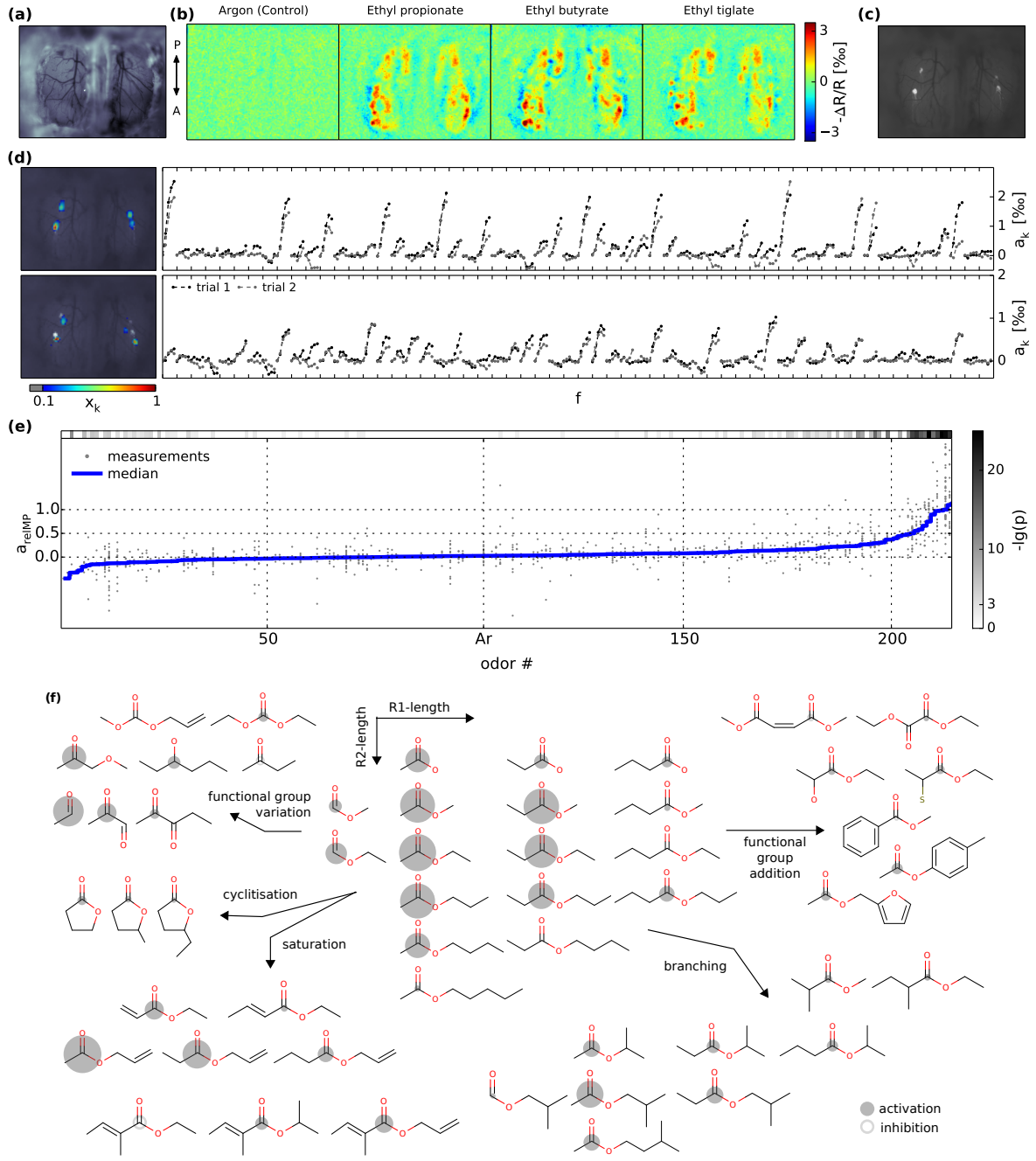

Figure 1: **MOR18-2 IOS ligand spectrum** (a) Image of a dorsal bulb preparation. (b) IOS odor maps after preprocessing. (c) GFP image of MOR18-2 glomeruli. (d) Pixel participation x_k of two exemplary extracted rNMF component (left) and corresponding activation strength a_k of each frame f (left). Each tick marks the beginning of a new odour. Upper example depicts a component located at the MOR18-2 glomeruli locations, lower example shows a neighbouring component. (e) All measured MOR18-2 odour responses (grey dots) and their median (blue line). Top line gives the p-value of a t-test that the measured response is different to control (Argon; Ar) measurements. (f) Molecular structure variation for some of the assessed odors. Area of the circles is proportional to response strength.

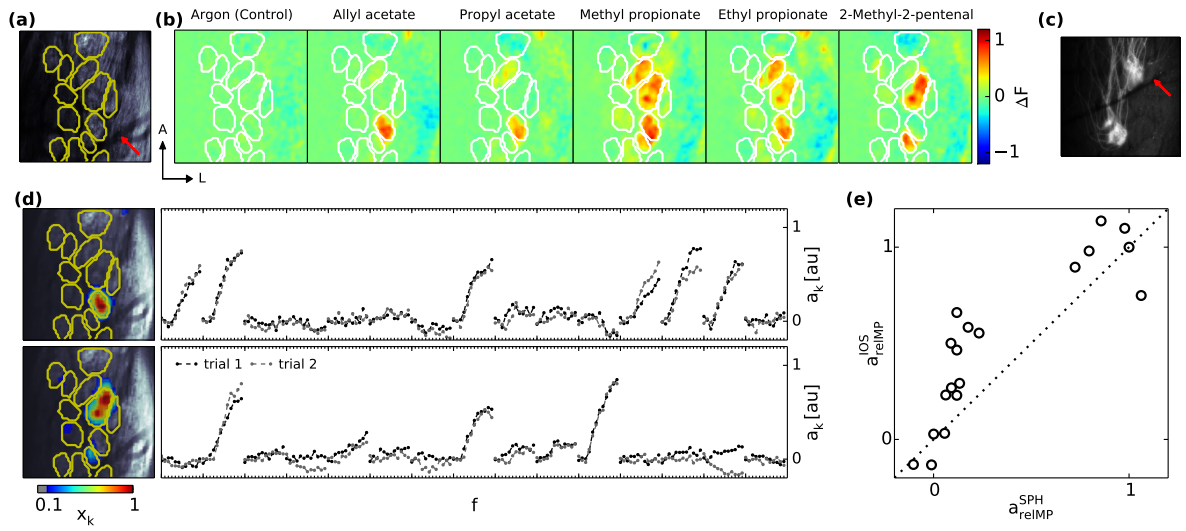

Figure 2: **MOR18-2 SpH ligand spectrum** (a) Resting SpH-fluorescence in a patch of the dOB. We manually outlined glomeruli in the full 3D-stack (yellow contours). Anatomical landmarks (red arrow) were used to compare location to post mortem FRV images (Panel (c)) (b) Exemplary SpH odour maps (c) Post mortem FRV image of MOR18-2 glomeruli. Via anatomical landmarks (red arrow) MOR18-2 location could be ascribed to the functional images. (d) Extracted activation of the MOR18-2 glomerulus component (top) and a neighbouring component (bottom) (e) IOS vs. SpH activation strength for all odours

To validate that in general the extracted IOS signals resemble the glomerular input activation, we performed high resolution 2-photon synapto-pHluorin (spH) imaging in mice expressing both spH in all OSNs as well as GFP in MOR18-2 OSNs. To this end we first performed an 3D-anatomical scan of the resting spH fluorescence in which we manually outlined glomerular contours (Fig. 2a). We then performed functional spH imaging (Fig. 2b) and extracted glomerular activation via rNMF (Fig. 2d). Since the GFP-fluorescence was masked by the spH-fluorescence, we stained the olfactory bulb post mortem by Fast Red Violet (FRV). This way we made MOR18-2 glomeruli visible (Fig. 2c) and could assign them via anatomical landmarks (red arrows Fig. 2a/c) to the previously outlined glomerular contours.

The extracted spH activation of MOR18-2 glomeruli strongly affirmed the IOS derived ligand rank (Spearman's rank correlation 0.92, $p <$ E-7; Fig. 2e). But in contrast to a rather continuous increasing response strength in the IOS, the spH derived spectrum had a pronounced separation of strong and weak activations. This might be both attributed to a steep non-linear gain of spH fluorescence as well to a saturated IOS responses for strong activations. Nonetheless, justified by the very high rank correlation of both spectra, we performed subsequent analysis on obtained IOS measurements due to their larger spatial extent and increased number of measured stimuli.

3.2. Physico-chemical receptive range

Having obtained the MRR of MOR18-2 we asked if this listing could be described by a quantitative ligand-based model. That is we asked if response strength could be explained by physico-chemical properties of a molecule. To this end we first obtained 1600 physico-chemical descriptors via eDragon (Tetko et al., 2005). These descriptors are subdivided into 19 blocks,

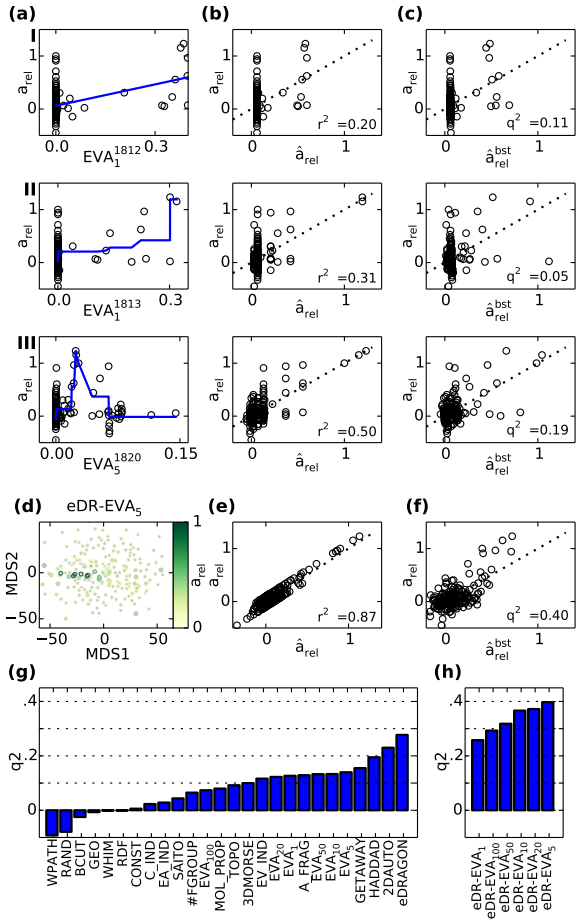

Figure 3: **MOR18-2 MRR models** (a) MOR18-2 activation a_{rel} in dependence of descriptor values and corresponding regression models (blue lines): I. linear regression, II. isotonic regression and III. unimodal regression. Each descriptor was chosen to represent the best possible regression model. (b) Observed activations a_{rel} vs. model values $\hat{a}_{\mathrm{rel}}$ of the regression models depicted in (a). Resulting fractions of explained variance r^2 is given in the lower right corners. (c) Observed activations a_{rel} vs. bootstrap model predictions $\hat{a}_{\mathrm{rel}}^{\mathrm{bst}}$ of the same models. Resulting predictive power q^2 is given in the lower right corners. (d) 2D representation of odour placement in eDR-EVA$_5$ descriptor space via Multi Dimensional Scaling (MDS). Circle edge color depicts MOR18-2 activation of odour. (e) Observed activations a_{rel} vs. model values $\hat{a}_{\mathrm{rel}}$ of a SVR regression models obtained in this descriptor space. (f) Observed activations a_{rel} vs. bootstrap model predictions $\hat{a}_{\mathrm{rel}}^{\mathrm{bst}}$ of the same model. (g) Predictive power q^2 of SVR models in different descriptor spaces. (h) Same as (g) with combined eDragon and EVA descriptor spaces of different resolutions.

ranging from simple scalar representations of molecules, like molecular weight or functional group counts, up to representations of the three dimensional arrangement of properties (e.g. mass, charge) within the molecule. Additional, based on the eigenvalues of molecular vibrations, we calculated the EVA descriptors for different resolutions (see methods and (Turner and Willett, 2000; Gabler et al., 2013)).

First we tested if a single descriptor is sufficient to explain the receptor activation. That is for each descriptor we evaluated different functional relationships between its value and receptor activation:

I. Linear increase of activation with descriptor value (linear regression)

II. Arbitrary (non-parametric) monotonic increase of activation (isotonic regression), e.g. saturated and/or thresholded increase of activation with descriptor value

III. Peak activation at intermediate descriptor value with monotonic decreasing activation both to lower and higher descriptor values (unimodal regression). This could for example be a scenario for chain length dependency.

For each of the three model classes Figure 3a depicts the best model over all descriptors with respect to the coefficient of determination R^2, i.e. the fraction of explained variance. With increasing model complexity more and more of the response variance became explained (Fig. 3b). However, none of the models could correctly capture the response to all odours. This shortcoming was especially apparent when evaluating the predictive power of the models (Fig. 3c). To this end we fitted the models to bootstrap sub-samples of the data. We then compared predictions to observed values for odours excluded in the sub-sample and calculated the coefficient of determination q^2 for those odours (see methods). The predictions both included odours with erroneous assigned activation and missed activation. This was reflected by a coefficient of determination q^2 below 0.2.

Since we could not identify a single descriptor which was sufficient to explain and predict receptor activation we next evaluated multivariate Support Vector Regression (SVR) models. Loosely speaking these models estimate the odour activation as a weighted sum of the activation of nearby odours (as measured in the underlying descriptor set). That is SVR models become predictive if similar activated odours are proximal along some axis of the multidimensional space. For such a multidimensional space, namely the combined set of all eDragon and the EVA_5 descriptors, Figure 3d illustrates the odour distances in a 2D approximation obtained by Multidimensional Scaling (MDS). The projection clearly showed a clustering of the activating odours. Hence the SVR model obtained in this space did not only describe the odour response (Fig. 3e) but also generalizes to odours, not employed in model construction (Fig. 3f).

We evaluated SVR models for several different descriptor sets regarding their predictive power. These sets included the full set of eDragon descriptors (eDRAGON), the logical subsets within them (for abbreviations see supplemental table T1), two subsets previously proposed to describe odour distances (HADDAD (Haddad et al., 2008), SAITO (Saito et al., 2009)) and the EVA descriptor at resolutions of 1, 5, 10 and 50cm^{-1} (EVA_x). Comparing the different sets with regard to their predictive power we found that the full set of eDragon descriptors yielded the best performance ($q^2 = 0.277$) followed by the 2DAUTO (2D-autocorrelations) and the odour optimized HADDAD subsets (Fig. 3g). The EVA descriptors performed worse than the aforementioned subsets, but still better than most of the other eDragon subsets. This made us wonder whether extending the full eDragon descriptor set by EVA descriptors (eDR-EVA_x) would enhance performance. And indeed, for mesoscale resolutions, the combination of both sets improved performance about 30% (Fig. 3h) yielding models of MOR18-2 activation with a predictive power $q^2 \approx 0.4$ (Fig. 3f). Thus, despite being very high dimensional (2400 descriptors), proximity in the combined eDragon-EVA descriptor space reflected to a good extent similarity in MOR18-2 activation.

3.3. Tunotopic embedding

Apart form the determination of the individual MRR of MOR18-2, the simultaneous recording of all glomeruli in the dOB also allowed us to to investigate its incorporation in the glomerular ensemble. In general the main class of MOR18-2 ligands, namely small esters, did not only activate glomeruli in a confined sub-region but did activate several glomeruli across the entire dOB (Fig. 1b and supplemental figure S1). That is the spatial location of the MOR18-2 glomeruli was not designated by any odours which were solely activating this area. Therefore we investigated their tunotopic embedding in more detail.

To this end we compiled a set of 48 odours representing the previously determined MRR of MOR18-2, that is all its ligands and some of their structural variations. We measured the dOB IOS response thereof in four GFP and three SpH mice and extracted glomerular response spectra (see methods). In the SpH mice we validated the glomerular segmentation of the IOS via anatomical glomeruli outlines obtained in a 3D-scan of the resting SpH fluorescence (see Soelter et al. (2014)). The GFP-mice served for identifying MOR18-2 glomeruli.

To investigate tunotopic relations between the extracted glomeruli, we calculated pairwise response similarity as the correlation distance d_r of the odour response spectra for all extracted glomeruli in all seven animals. Based on this distance we then obtained a hierarchical clustering of glomeruli (Fig. 4a). According to the chosen similarity threshold one can obtain clusters of different extent.

Glomeruli of low threshold cluster appeared at stereotypic positions across animals (Fig. 4b and supplemental figure S2). Furthermore in all animals with a GFP-marking of MOR18-2 glomeruli, exactly those fell into such a low-threshold cluster (red cluster in Fig. 4). Therefore it seems likely that low threshold cluster represent to a great extend glomeruli of identical ORs across animals. However, in most cases the correspondence of low threshold cluster to a distinct type of glomeruli was less pronounced then for MOR18-2 glomeruli. In some cases (e.g. green cluster in Fig. 4) low threshold cluster spanned only a subset of the animals, that is not in all animals corresponding glomeruli could be extracted. In other cases low threshold cluster were not clearly separable from the remaining glomeruli (e.g. blue cluster in Fig. 4) as the observed response spectra (Fig. 4c) were too similar (Fig. 4d&e) to be unambiguously assigned to a single type of glomeruli. Nonetheless all in all low threshold cluster always reflected stereotypic local response areas of the dOB.

We next investigated the tuning similarity of those local response areas to MOR18-2. To this end we determined spectra correlations $r_{\text{MOR18-2}} = r(\mathbf{s}_{\text{MOR18-2}}, \mathbf{s}_i)$ between prototype spectra of all these cluster and the cluster associated with MOR18-2. Figure 5a depicts all cluster which exhibited a response correlation $r_{\text{MOR18-2}} > 0.2$ to MOR18-2. Four of those, together with the MOR18-2 cluster formed a meta-cluster of mutual similar response spectra (blue-violet clusters in Fig. 5a and green cluster in Fig. 5d) mainly due to their shared activation by propionates (Fig. 5c). Spatially they were located in a patchy domain around the MOR18-2 glomeruli (Fig. 5b&e).

Besides this meta-cluster of mutually similar response spectra, MOR18-2 was also correlated

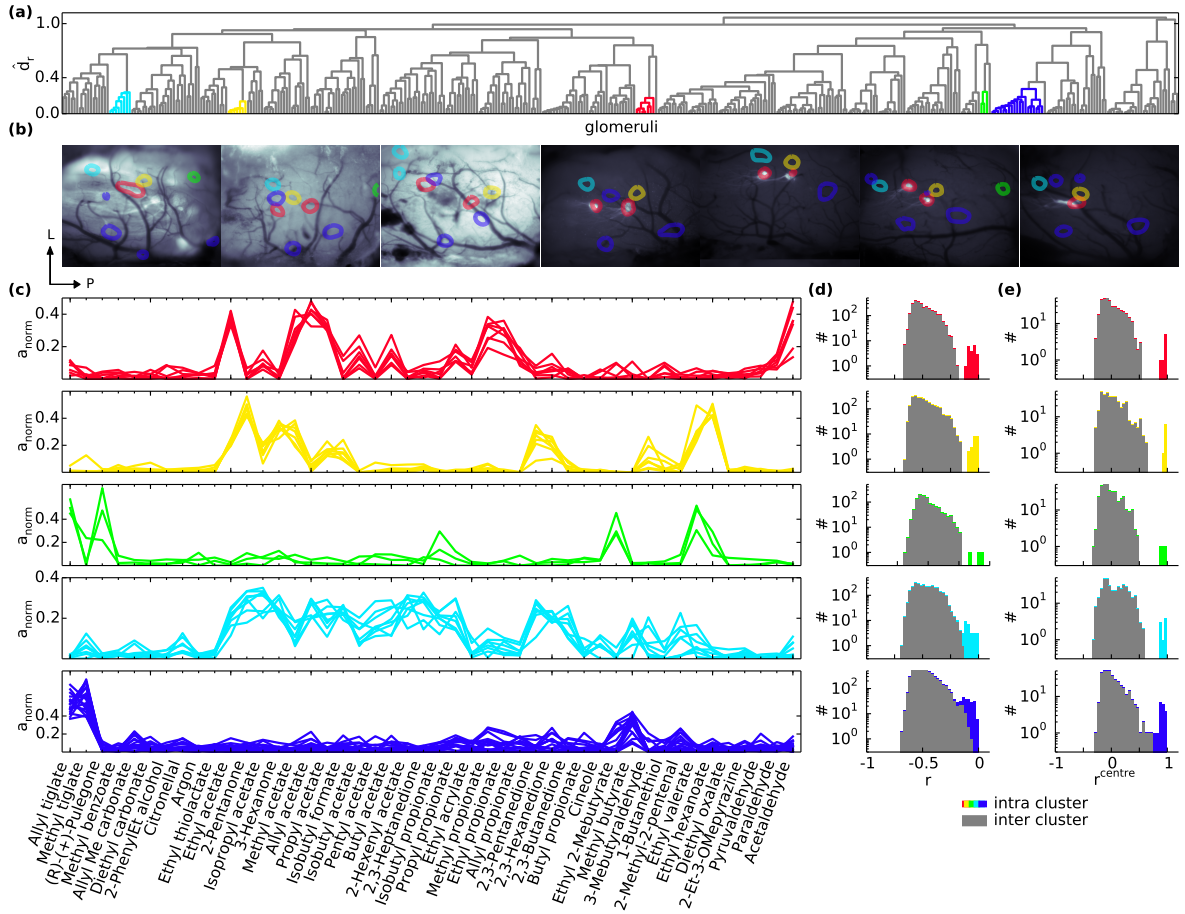

Figure 4: **Functional identification** (a) Hierarchical clustering of correlation distance d_r between glomeruli of 7 mice. Length of branches depicts the average correlation distance $\hat{d}_r$ between clades. Properties of coloured clusters are shown in the following panels. (b) Spatial location of cluster members in the OBs of all seven mice. Colours according to cluster colouring in (a). Locations extracted from IOS imaging are overlayed on green images (first 3 animals) respectively GFP images (last 4 animals) indicating position of GFP labelled MOR18-2 glomerulus. (c) Odour spectra of all glomeruli in each clusters. (d) Histogram of pairwise correlation r of all cluster members (coloured) and their correlation to remaining glomeruli (gray). (e) Histogram of correlation r^{centre} of all cluster members (coloured) and non cluster members (gray) to cluster prototype.

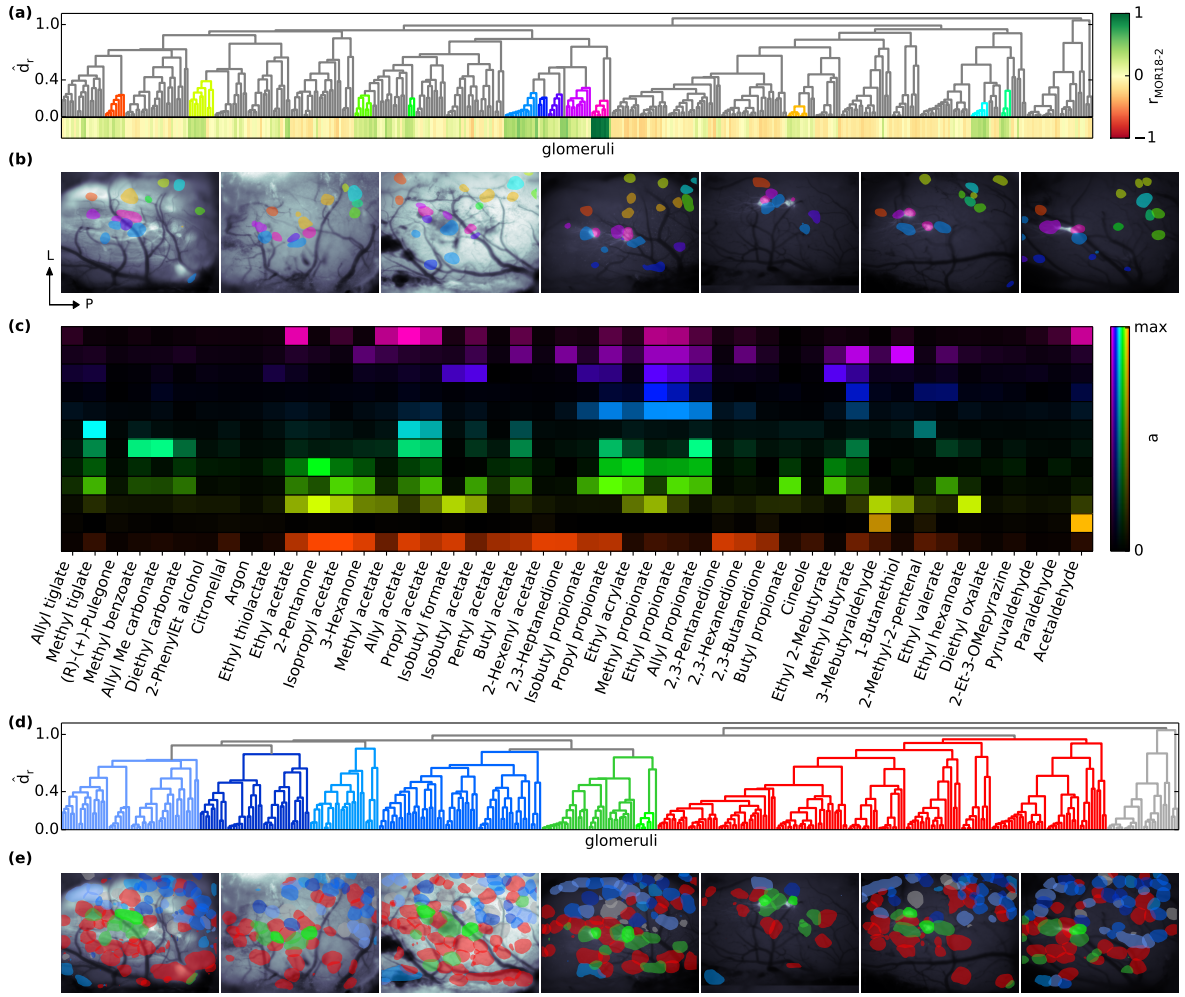

Figure 5: **Tunotopic clustering of response spectra** (a) Hierarchical clustering of correlation distance d_r between glomeruli of 7 mice. For each glomerulus leaf node its correlation $r_{\text{MOR18-2}}$ with the MOR18-2 cluster is depicted at the bottom. Clusters with a correlation > 0.2 to the MOR18-2 cluster (pink) are coloured. (b) Spatial location of cluster members in the OBs of all seven mice. Colours according (a). (c) Median odour spectra of all clusters. (d) Same hierarchical clustering as in (a) with colouring of high level clusters. (e) Spatial location of cluster members in the OBs of all seven mice. Colours according (d).

to other glomerular cluster located lateral-posterior to MOR18-2 glomeruli. However each of those cluster was most similar to glomeruli uncorrelated to MOR18-2. That is, although glomeruli tuned similar to MOR18-2 were located at distant locations, only those in proximity to MOR18-2 formed a meta-cluster of mutual similarity.

Next, when looking at the composition of the top-level (high threshold) clusters we observed a pronounced bipartition. Glomeruli in the top-level cluster including the MOR18-2 meta cluster (blue clusters in Fig. 5d) were primarily located in the lateral-posterior part of the dOB (Fig. 5e). In contrast, glomeruli of the second top-level cluster (red cluster in Fig. 5d) were primarily located in the medial-anterior part.

In summary we found that glomeruli were arranged at stereotypical positions regarding their response similarity to MOR18-2. A group of mutually similar glomeruli were arranged

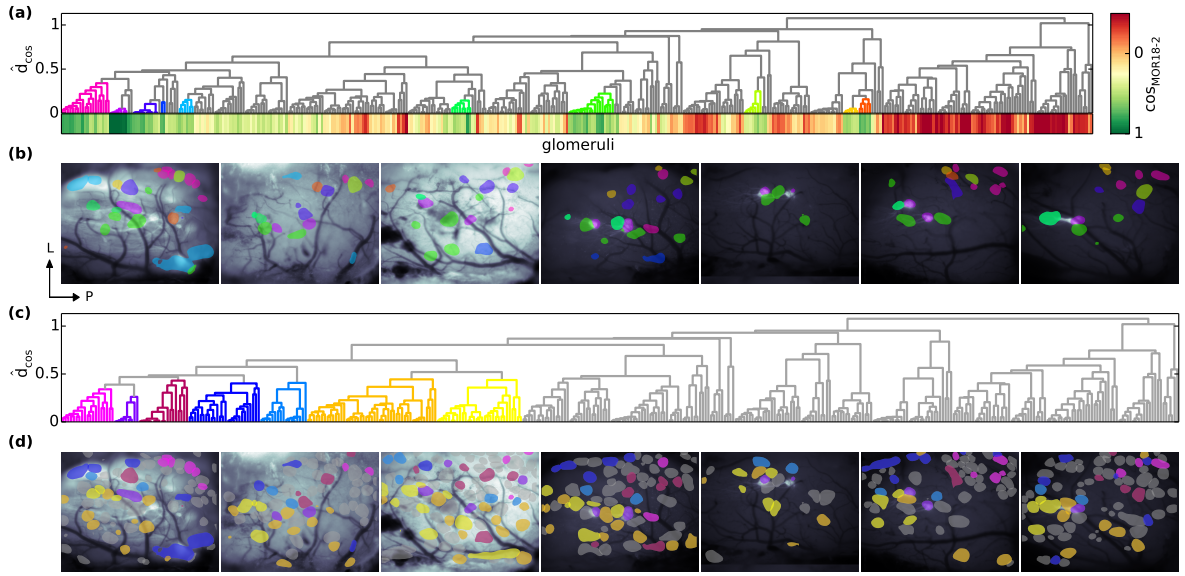

Figure 6: **Chemotopic clustering of response spectra** (a) Hierarchical clustering of cosine distance $d_{\cos}$ between glomeruli of 7 mice. For each glomerulus leaf node k its angle $cosx_{\text{MOR18-2}}, x_k$ with the MOR18-2 cluster is depicted at the bottom. Clusters with at least two cluster member at an angle $< 36.9°$ to the MOR18-2 cluster (blue) are coloured. (b) Spatial location of cluster members in the OBs of all seven mice. Colours according (a). (c) Same hierarchical clustering as in (a) with colouring of meta level clusters at close distance to the MOR18-2 cluster. (d) Spatial location of cluster members in the OBs of all seven mice. Colours according (c). (e) Same hierarchical clustering as in (a) with colouring of meta level clusters. (f) Spatial location of cluster members in the OBs of all seven mice. Colours according (e).

in a confined but patchy domain around MOR18-2. And at the top level most glomeruli were separated in a lateral-posterior and a medial-anterior domain of response similarity.

3.4. Chemotopic embedding

Our observation of a tunotopic embedding of MOR18-2 raised our curiosity if this is related to any chemotopy. Investigating on this topic required both the definition of a chemical space (i.e. chemical similarity) as well as positioning of glomeruli within this space. As chemical space we choose the combined eDragon-EVA$_5$ space since it proved best to characterize the MRR of MOR18-2 (see section MOR18-2 Physico-chemical receptive range). Furthermore we positioned the origin of the coordinate system at the mean descriptor value $\langle \mathbf{x} \rangle_o$ of our odour set, the location where a glomerulus with a homogeneous response spectrum would be located. Within this space we placed glomeruli by their barycentre of activation $\mathbf{x}^k = \sum_o (a^o \mathbf{x}_o) / \sum_o a^o - \langle \mathbf{x} \rangle_o$. We then obtained the relative positioning of the glomeruli to each other by calculating their cosine distance $d_{\cos}$, which is a measure of the angle between the glomerular positions. That is glomeruli were considered similar if their barycentres of activation were located in a similar direction from origin.

Based on this pairwise distances we again obtained a hierarchical clustering (Fig. 6a). As in the case of tunotopic clustering all MOR18-2 glomeruli were grouped together in a low threshold cluster (violet cluster in Fig. 6a&b). And also we again observed that glomeruli most similar to MOR18-2 were predominantly located in its vicinity or lateral-posterior to its location.

However, in contrast to the tunotopic case, the MOR18-2 glomeruli were not embedded in a small scale local chemotopic domain, but only in a meta-cluster of lateral-posterior located glomeruli (violet-blueish cluster in Fig 6c&d). This meta-cluster was contrasted by an adjacent meta-cluster of medial-anterior glomeruli (orange and yellow cluster in Fig 6c&d). But on the topmost level of clustering more distant glomeruli were widely dispersed in both domains (grey glomeruli in Fig 6c&d). In summary, the observed chemotopic structure was far less pronounced than the tunotopic structure.

4. Discussion

In our study we profiled in detail the MRR of MOR18-2 glomeruli and their embedding in the glomerular code. MOR18-2 glomeruli were mainly tuned to small esters and locally embedded in a patchy domain of glomeruli sensitive to short chain propionates. Furthermore we could determine a physico-chemical receptive range of MOR18-2 glomeruli within the multidimensional eDragon-EVA$_5$ space via SVR models, but did only observe a weak chemotopic representation of this space within the dorsal OB.

4.1. Molecular receptive range

We aimed to obtain the MRR of MOR18-2 as completely as possible but it is intractable to screen all existent odours. On this account we did not only randomly tested odours but generated search candidates based on our current information of ligands. Even so this lead to a directed search, it is very likely that we did not discover all ligands. Eventually our introduced predictive SVR model, as ascertained on bootstrap samples, suggests further possible ligands (data not shown). Nonetheless to our knowledge this study makes MOR18-2 to one of the best explored olfactory receptors (Peterlin et al., 2014).

Recently acetic and propionic acid have been reported as ligands of MOR18-2 receptors expressed in the kidney (Pluznick et al., 2013) whereas our study rather identified the corresponding esters as ligands. Although their study did not contain any of the ligands revealed in our study, there could be systemic reasons for such a deviation. For once in our study odour stimuli were presented in the gaseous instead of the liquid phase. Therefore the effective concentration that reached the nose was much lower for acids compared to esters due to their significantly lower vapour pressure. And second, we did not directly observe the receptor response but the full system response including chemical conversion in the mucus. Indeed it has been shown that metabolic enzymes of the mucus convert ester into the corresponding alcohols and acids (Nagashima and Touhara, 2010).

4.2. Physico-chemical receptive range

In this study we did not only determine the MRR of MOR18-2 but also translated it via SVR models to a physico-chemical receptive range in the eDragon-EVA$_5$ space. Despite bootstrap validation of the model and the success of a very similar approach for Drosophila ORs (Gabler

et al., 2013), an ultimate confirmation by successful biological screening of further model predictions is still missing. Nonetheless our careful model validation ascertains that our obtained physico-chemical range is at least a rough estimate.

We obtained the best results in describing the physico-chemical receptive range by combining features based on molecular vibrations (EVA) with features containing descriptions of the molecular shape (eDragon). Note that this provides neither evidence for nor against the heavily disputed theory of vibrational olfaction (Hettinger, 2011). In our model molecular vibrations are rather considered as a fingerprint of the molecular graph than a mechanistic interpretation of molecule-receptor interaction.

4.3. Tunotopic domains

Our results provided evidence for tunotopic domains at different scales: two global domains, a lateral-posterior and a medial-anterior one, and a local domain around the MOR18-2 glomeruli. Ma et al. (2012) obtained very similar results with a likewise global partitioning and some local domains, yet different to the one obtained by us. It seems that the global partitioning is a rather salient finding across different studies whereas the applied odour set determines which local clusters crystallize. The position of the tunotopic medial-anterior and lateral-posterior top-level domains resembles the domain separation of class 1 (medial-anterior) and class 2 receptors (lateral-posterior) (Matsumoto et al., 2010). It is also in line with the MOR18-2 glomeruli being located close to the border of class 1 and class 2 domains (Bozza et al., 2009). Interestingly, despite being a class 1 receptor, MOR18-2 is tunotopically embedded in the lateral-posterior domain which is presumably composed to a large extent of class 2 receptors. This could indicate that, albeit its physiological separation (Bozza et al., 2009) the functional transition between receptor class domains is rather continuous.

Mori and colleagues (Mori et al., 2006; Matsumoto et al., 2010) also observed a compartmentalization of the dOB into local response clusters. They attributed long chain ester responses to cluster A (within class 1 receptor domain) and cluster B (within class 2 receptor domain) but did not attribute any cluster to small esters. However their cluster assignments leave undesignated space especially at the border of domain 1 and 2 where we observed the propionate responding cluster of MOR18-2.

Our findings are well in line with the hypothesis of a tunotopic layout of the olfactory bulb. This was disputed by Soucy et al. (2009) who observed 'that nearby glomeruli were almost as diverse in their odor sensitivity as distant ones'. In their study they evaluated the dependence of glomerular spectrum similarity with regard to their spatial distance and did not find strong effects. One reason might be that a diverse odour set is not likely to contain adequate odours to accent local response cluster. For example in an odour set containing only acetates but not the propionates (which differ only by one additional Carbon atom) the local response cluster of MOR18-2 would not emerge.

4.4. Chemotopic domains

Besides tunotopic domains we did also observe some locally confined cluster of glomeruli with chemical similar response spectra. But this chemotopic organization was less pronounced than the tunotopic organization. This might have several reasons. First there is no canonical definition of chemical similarity. Our definition by the eDragon-EVA$_5$ descriptor space might be a suitable but still imprecise definition. Second, our odour set was constructed to contain MOR18-2 ligands but not the full ligand spectrum of other receptors. In case of the MOR18-2 response spectrum correlations, the tunotopic distance is only influenced by the number but not the identity of the un-measured non-mutual ligands. In contrast, the chemical distance is more strongly influenced by the identity of the of the un-captured non-mutual ligands and each un-measured ligand would cause a directional shift of the barycenter.

To conclude, we investigated the olfactory bulb's topographic layout with regard to an extensively characterized MRR of a single glomerulus. This provided further evidence for a functional topographic layout according to tuning similarity of glomeruli. Nonetheless also this approach still suffered from the incomplete representation of all but one MRR. Therefore it once more emphasis the demand of a full characterization of olfactory MRRs.

References

Tatjana Abaffy, Hiroaki Matsunami, and Charles W Luetje. Functional analysis of a mammalian odorant receptor subfamily. *Journal of neurochemistry*, 97(5):1506–1518, 2006.

Ricardo C Araneda, Abhay D Kini, and Stuart Firestein. The molecular receptive range of an odorant receptor. *Nature neuroscience*, 3(12):1248–1255, 2000.

Olivia Baud, Sylvain Etter, Morena Spreafico, Lorenza Bordoli, Torsten Schwede, Horst Vogel, and Horst Pick. The mouse eugenol odorant receptor: structural and functional plasticity of a broadly tuned odorant binding pocket. *Biochemistry*, 50(5):843–853, 2010.

Verena Bautze, Raphaela Bär, Benjamin Fissler, Michaela Trapp, Dietmar Schmidt, Uwe Beifuss, Bernd Bufe, Frank Zufall, Heinz Breer, and Jörg Strotmann. Mammalian-specific or37 receptors are differentially activated by distinct odorous fatty aldehydes. *Chemical senses*, 37 (5):479–493, 2012.

Christopher M Bishop et al. *Pattern recognition and machine learning*, volume 1. springer New York, 2006.

Sean Michael Boyle, Shane McInally, and Anandasankar Ray. Expanding the olfactory code by in silico decoding of odor-receptor chemical space. *Elife*, 2, 2013.

Thomas Bozza, Paul Feinstein, Chen Zheng, and Peter Mombaerts. Odorant receptor expression defines functional units in the mouse olfactory system. *The Journal of neuroscience*, 22(8): 3033–3043, 2002.

Thomas Bozza, John P McGann, Peter Mombaerts, and Matt Wachowiak. In vivo imaging of neuronal activity by targeted expression of a genetically encoded probe in the mouse. *Neuron*, 42(1):9–21, 2004.

Thomas Bozza, Anne Vassalli, Stefan Fuss, Jing-Ji Zhang, Brian Weiland, Rodrigo Pacifico, Paul Feinstein, and Peter Mombaerts. Mapping of class i and class ii odorant receptors to glomerular domains by two distinct types of olfactory sensory neurons in the mouse. *Neuron*, 61(2):220–233, 2009.

Viviana Consonni, Davide Ballabio, and Roberto Todeschini. Comments on the definition of the q 2 parameter for qsar validation. *Journal of chemical information and modeling*, 49(7): 1669–1678, 2009.

Sidonie Conzelmann, Olga Levai, Barbara Bode, Ulrich Eisel, Klaus Raming, Heinz Breer, and Jörg Strotmann. A novel brain receptor is expressed in a distinct population of olfactory sensory neurons. *European Journal of Neuroscience*, 12(11):3926–3934, 2000.

Stephan Gabler, Jan Soelter, Taufia Hussain, Silke Sachse, and Michael Schmuker. Physicochemical vs. vibrational descriptors for prediction of odor receptor responses. *Molecular Informatics*, 32(9-10):855–865, 2013.

Kalanit Grill-Spector and Rafael Malach. The human visual cortex. *Annu. Rev. Neurosci.*, 27: 649–677, 2004.

Xavier Grosmaitre, Stefan H Fuss, Anderson C Lee, Kaylin A Adipietro, Hiroaki Matsunami, Peter Mombaerts, and Minghong Ma. Sr1, a mouse odorant receptor with an unusually broad response profile. *The Journal of Neuroscience*, 29(46):14545–14552, 2009.

Rafi Haddad, Rehan Khan, Yuji K Takahashi, Kensaku Mori, David Harel, and Noam Sobel. A metric for odorant comparison. *Nature methods*, 5(5):425–429, 2008.

W Härdle. Robertson, t., wright, ft and rl dykstra: Order restricted statistical inference. *Statistical Papers*, 30(1):316–316, 1989.

Thomas P Hettinger. Olfaction is a chemical sense, not a spectral sense. *Proceedings of the National Academy of Sciences*, 108(31):E349–E349, 2011.

Thomas J Imig and Anne Morel. Organization of the thalamocortical auditory system in the cat. *Annual review of neuroscience*, 6(1):95–120, 1983.

Jon H Kaas. Plasticity of sensory and motor maps in adult mammals. *Annual review of neuroscience*, 14(1):137–167, 1991.

Sayako Katada, Takatsugu Hirokawa, Yuki Oka, Makiko Suwa, and Kazushige Touhara. Structural basis for a broad but selective ligand spectrum of a mouse olfactory receptor: mapping the odorant-binding site. *The Journal of neuroscience*, 25(7):1806–1815, 2005.

Jingyi Li, Rafi Haddad, Sisi Chen, Vanessa Santos, and Charles W Luetje. A broadly tuned mouse odorant receptor that detects nitrotoluenes. *Journal of neurochemistry*, 121(6):881–890, 2012.

Stephen D Liberles and Linda B Buck. A second class of chemosensory receptors in the olfactory epithelium. *Nature*, 442(7103):645–650, 2006.

Limei Ma, Qiang Qiu, Stephen Gradwohl, Aaron Scott, Q Yu Elden, Richard Alexander, Winfried Wiegraebe, and C Ron Yu. Distributed representation of chemical features and tunotopic organization of glomeruli in the mouse olfactory bulb. *Proceedings of the National Academy of Sciences*, 109(14):5481–5486, 2012.

Bettina Malnic, Junzo Hirono, Takaaki Sato, and Linda B Buck. Combinatorial receptor codes for odors. *Cell*, 96(5):713–723, 1999.

Hideyuki Matsumoto, Ko Kobayakawa, Reiko Kobayakawa, Takuya Tashiro, Kenji Mori, Hitoshi Sakano, and Kensaku Mori. Spatial arrangement of glomerular molecular-feature clusters in the odorant-receptor class domains of the mouse olfactory bulb. *Journal of neurophysiology*, 103(6):3490–3500, 2010.

Markus Meister and Tobias Bonhoeffer. Tuning and topography in an odor map on the rat olfactory bulb. *The journal of neuroscience*, 21(4):1351–1360, 2001.

Kazunari Miyamichi, Shou Serizawa, Hiroko M Kimura, and Hitoshi Sakano. Continuous and overlapping expression domains of odorant receptor genes in the olfactory epithelium determine the dorsal/ventral positioning of glomeruli in the olfactory bulb. *The Journal of neuroscience*, 25(14):3586–3592, 2005.

Peter Mombaerts, Fan Wang, Catherine Dulac, Steve K Chao, Adriana Nemes, Monica Mendelsohn, James Edmondson, and Richard Axel. Visualizing an olfactory sensory map. *Cell*, 87 (4):675–686, 1996.

Kensaku Mori, Yuji K Takahashi, Kei M Igarashi, and Masahiro Yamaguchi. Maps of odorant molecular features in the mammalian olfactory bulb. *Physiological reviews*, 86(2):409–433, 2006.

Ayumi Nagashima and Kazushige Touhara. Enzymatic conversion of odorants in nasal mucus affects olfactory glomerular activation patterns and odor perception. *The Journal of Neuroscience*, 30(48):16391–16398, 2010.

Yuki Oka, Sayako Katada, Masayo Omura, Makiko Suwa, Yoshihiro Yoshihara, and Kazushige Touhara. Odorant receptor map in the mouse olfactory bulb: in vivo sensitivity and specificity of receptor-defined glomeruli. *Neuron*, 52(5):857–869, 2006.

Rodrigo Pacifico, Adam Dewan, Dillon Cawley, Caiying Guo, and Thomas Bozza. An olfactory subsystem that mediates high-sensitivity detection of volatile amines. *Cell reports*, 2012.

F. Pedregosa, G. Varoquaux, A. Gramfort, V. Michel, B. Thirion, O. Grisel, M. Blondel, P. Prettenhofer, R. Weiss, V. Dubourg, J. Vanderplas, A. Passos, D. Cournapeau, M. Brucher, M. Perrot, and E. Duchesnay. Scikit-learn: Machine learning in Python. *Journal of Machine Learning Research*, 12:2825–2830, 2011.

Zita Peterlin, Stuart Firestein, and Matthew E Rogers. The state of the art of odorant receptor deorphanization: A report from the orphanage. *The Journal of general physiology*, 143(5): 527–542, 2014.

Jennifer L Pluznick, Ryan J Protzko, Haykanush Gevorgyan, Zita Peterlin, Arnold Sipos, Jinah Han, Isabelle Brunet, La-Xiang Wan, Federico Rey, Tong Wang, et al. Olfactory receptor responding to gut microbiota-derived signals plays a role in renin secretion and blood pressure regulation. *Proceedings of the National Academy of Sciences*, 110(11):4410–4415, 2013.

Sarah E Repicky and Charles W Luetje. Molecular receptive range variation among mouse odorant receptors for aliphatic carboxylic acids. *Journal of neurochemistry*, 109(1):193–202, 2009.

Harumi Saito, Qiuyi Chi, Hanyi Zhuang, Hiroaki Matsunami, and Joel D Mainland. Odor coding by a mammalian receptor repertoire. *Science signaling*, 2(60):ra9, 2009.

Michael Schmuker, Marien De Bruyne, Melanie Hähnel, and Gisbert Schneider. Predicting olfactory receptor neuron responses from odorant structure. *Chemistry Central Journal*, 1 (1):11, 2007.

Jan Soelter, Jan Schumacher, Hartwig Spors, and Michael Schmuker. Automatic segmentation of odor maps in the mouse olfactory bulb using regularized non-negative matrix factorization. *NeuroImage*, 2014.

Edward R Soucy, Dinu F Albeanu, Antoniu L Fantana, Venkatesh N Murthy, and Markus Meister. Precision and diversity in an odor map on the olfactory bulb. *Nature neuroscience*, 12(2):210–220, 2009.

Igor V Tetko, Johann Gasteiger, Roberto Todeschini, Andrea Mauri, David Livingstone, Peter Ertl, Vladimir A Palyulin, Eugene V Radchenko, Nikolay S Zefirov, Alexander S Makarenko, et al. Virtual computational chemistry laboratory–design and description. *Journal of computer-aided molecular design*, 19(6):453–463, 2005.

David B Turner and Peter Willett. The eva spectral descriptor. *European journal of medicinal chemistry*, 35(4):367–375, 2000.

Xinmin Zhang and Stuart Firestein. The olfactory receptor gene superfamily of the mouse. *Nature neuroscience*, 5(2):124–133, 2002.

Supplemental Material

Supplemental Figure S1

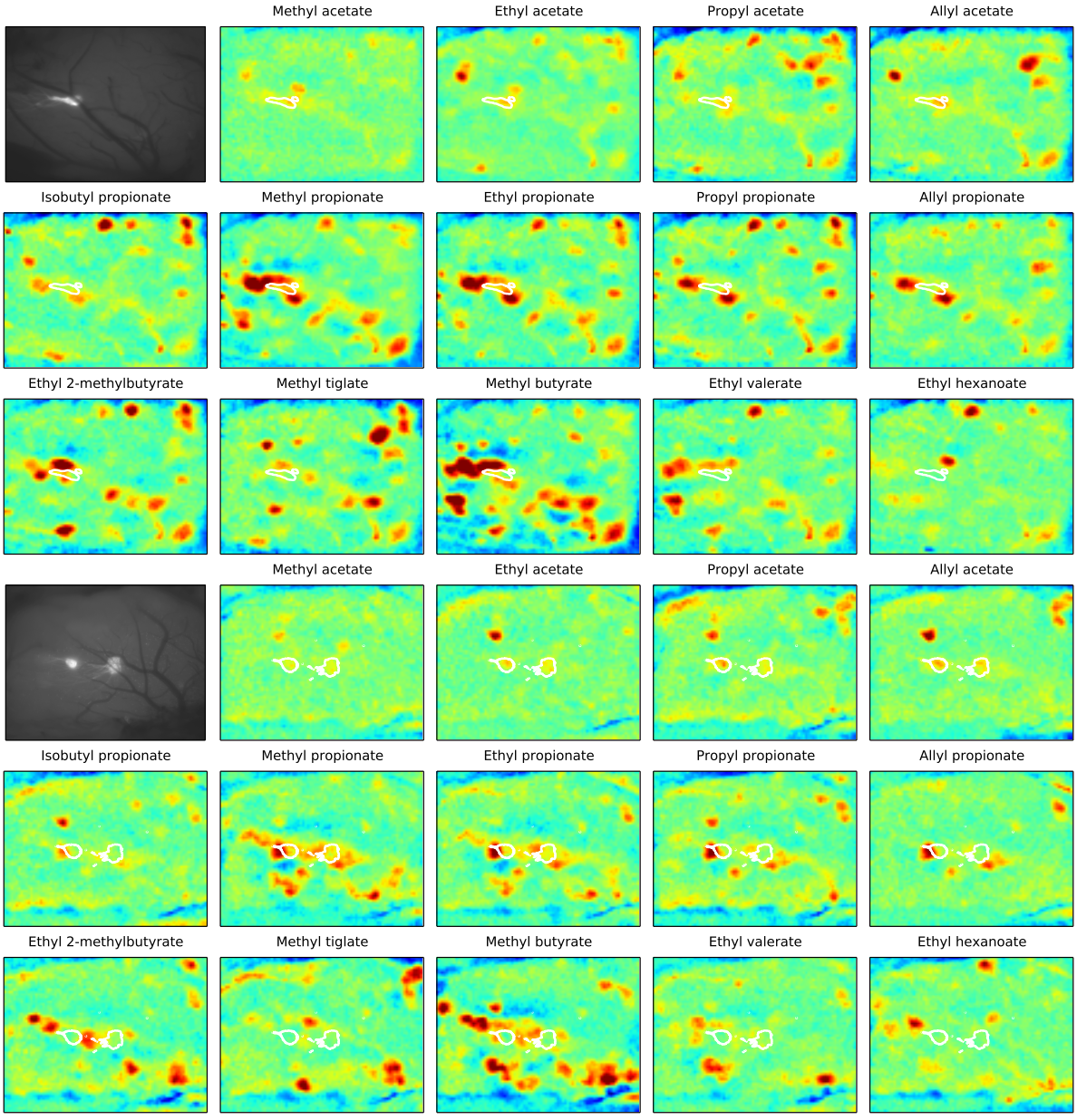

Exemplary Odormaps Odor response in the dOB for a selection of small ester in two different animals. Position of MOR18-2 is marked by white contours.

Supplemental Figure S2

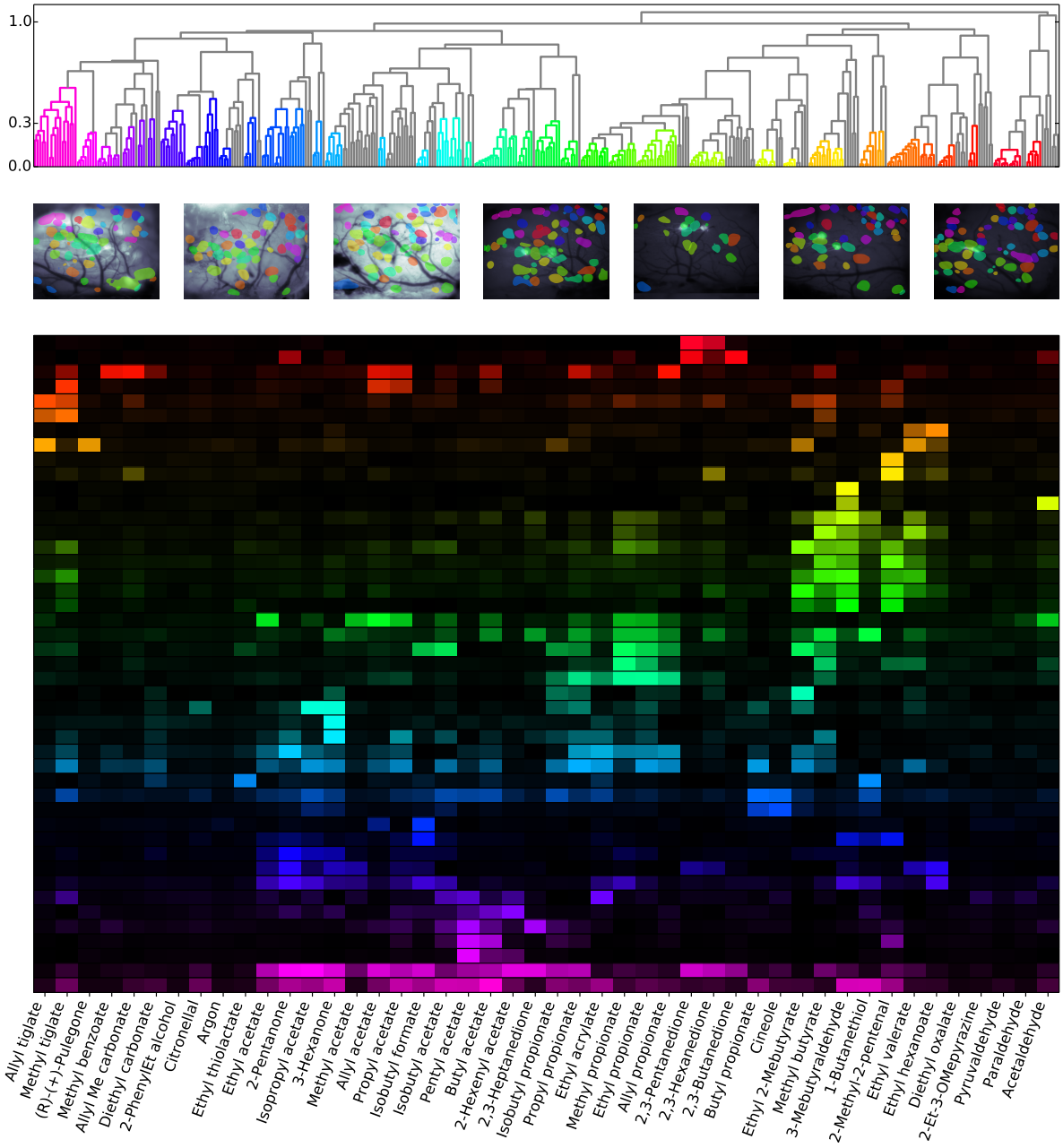

Response Cluster (a) Hierarchical clustering of correlation distance d_r between glomeruli of 7 mice. Length of branches depicts the average correlation distance $\hat{d}_r$ between clades. Properties of coloured clusters are shown in the following panels. (b) Spatial location of cluster members in the OBs of all seven mice. Colours according to cluster colouring in (a) Locations extracted from IOS imaging are overlayed on green images (first 3 animals) respectively GFP images (last 4 animals) (c) Median odour spectra of all glomeruli in each clusters.

Supplemental Table T1

List of all measured odors (CAS and name) and median response strength of MOR18-2 glomeruli

CAS	Name	response
591-87-7	Allyl acetate	1.14
141-78-6	Ethyl acetate	1.10
554-12-1	Methyl propionate	1.00
109-60-4	Propyl acetate	0.98
79-20-9	Methyl acetate	0.97
105-37-3	Ethyl propionate	0.90
75-07-0	Acetaldehyde	0.75
2408-20-0	Allyl propionate	0.66
110-19-0	Isobutyl acetate	0.58
106-36-5	Propyl propionate	0.55
123-86-4	Butyl acetate	0.50
64-19-7	Acetic acid	0.48
5878-19-3	Methoxyacetone	0.46
123-99-9	Azelaic acid	0.44
16491-36-4	cis-3-Hexenyl butyrate	0.40
109-94-4	Ethyl formate	0.37
108-62-3	Metaldehyde	0.37
123-63-7	Paraldehyde	0.31
78-98-8	Pyruvaldehyde	0.30
140-88-5	Ethyl acrylate	0.29
19089-92-0	Hexyl trans-2-butenoate	0.28
7493-71-2	Allyl tiglate	0.27
94133-92-3	1-Ethylhexyl tiglate	0.27
2349-13-5	Heptyl isobutyrate	0.24
540-42-1	Isobutyl propionate	0.23
108-21-4	Isopropyl acetate	0.23
4437-51-8	3,4-Hexanedione	0.23
41519-18-0	Isoamyl tiglate	0.22
7778-87-2	Propyl heptanoate	0.22
123-92-2	Isoamyl acetate	0.22
109-21-7	Butyl butyrate	0.21
2051-78-7	Allyl butyrate	0.20
105-66-8	Propyl butyrate	0.19
3848-24-6	2,3-Hexanedione	0.17
2639-63-6	Hexyl butyrate	0.17
61692-84-0	Isobutyltiglate	0.17
592-84-7	Butyl formate	0.16
79-09-4	Propionic acid	0.16
540-18-1	Amyl butyrate	0.16
96-04-8	2,3-Heptanedione	0.16
109-79-5	1-Butanethiol	0.15
52089-55-1	Ethyl 2-hydroxycaproate	0.15
71-23-8	Propanol	0.15
503-74-2	Isovaleric acid	0.14
637-78-5	Isopropyl propionate	0.14
19788-49-9	Ethyl thiolactate	0.14
6342-56-9	Pyruvic aldehyde diMe acetal	0.13
107-31-3	Methyl formate	0.13
1733-25-1	Isopropyl tiglate	0.13
623-37-0	3-Hexanol	0.13
431-03-8	2,3-Butanedione	0.12
64-17-5	Ethanol	0.12
5910-87-2	2,4-Nonadienal	0.12
624-24-8	Methyl valerate	0.11
591-12-8	alpha-Angelicalactone	0.11
140-39-6	p-Tolyl acetate	0.10
638-11-9	Isopropyl butyrate	0.10
107-92-6	Butyric acid	0.09
104-21-2	Anisyl acetate	0.09
600-14-6	2,3-Pentanedione	0.09
106-27-4	Isoamyl butyrate	0.09
79-77-6	beta-Ionone	0.09
35154-45-1	cis-3-Hexenyl 3-Mebutanoate	0.09
591-80-0	4-Pentenoic acid	0.08
623-17-6	Furfuryl acetate	0.08
21835-01-8	Ethyl cyclopentenolone	0.08
591-68-4	Butyl valerate	0.08
105-58-8	Diethyl carbonate	0.08
112-31-2	Decanal	0.08
577-16-2	2-Methylacetophenone	0.08
539-82-2	Ethyl valerate	0.08
3268-49-3	3-(Methio)propionaldehyde	0.08
1334-82-3	Amyl 2-furoate	0.08
2497-18-9	2-Hexenyl acetate	0.08
97-53-0	Eugenol	0.08
97-97-2	Chloroacetaldehyde diMe acetal	0.07
623-19-8	Furfuryl propionate	0.07
123-75-1	Pyrrolidine	0.07
4455-13-4	Ethyl (methylthio)acetate	0.07
116-53-0	2-Methylbutyric acid	0.07
646-07-1	4-Methylvaleric acid	0.07
96-48-0	gamma-Butyrolactone	0.07
1759-28-0	4-Methyl-5-vinylthiazole	0.07
1122-62-9	2-Acetylpyridine	0.06
56-86-0	L-Glutamic acid	0.06
2173-56-0	Pentyl valerate	0.05
556-82-1	3-Methyl-2-buten-1-ol	0.05
142-62-1	Hexanoic acid	0.05
112-14-1	Octyl acetate	0.05
589-82-2	3-Heptanol	0.05
7764-50-3	d-Dihydrocarvone	0.05
547-63-7	Methyl isobutyrate	0.05
25680-58-4	2-Ethyl-3-MeOpyrazine	0.05
97-64-3	Ethyl lactate	0.04
10094-34-5	Dimethylphenethyl butyrate	0.04
3391-87-5	(+)-Menthone	0.04
106-70-7	Methyl hexanoate	0.04
7452-79-1	Ethyl 2-Mebutyrate	0.04
108-29-2	gamma-Valerolactone	0.04
106-23-0	Citronellal	0.03
111-11-5	Methyl octanoate	0.03
7785-26-4	(-)-alpha-Pinene	0.03
103-58-2	3-Phenylpropyl isobutyrate	0.03
106-24-1	Geraniol	0.03
5405-41-4	Ethyl 3-hydroxybutyrate	0.03
623-42-7	Methyl butyrate	0.03
111-88-6	1-Octanethiol	0.03
687-47-8	(-)-Ethyl L-Lactate	0.03
628-63-7	Pentyl acetate	0.03
2705-87-5	Allyl cyclohexanepropionate	0.03
1188-02-9	2-Methylheptanoic acid	0.03
5454-19-3	Decyl propionate	0.03
7440-37-1	Argon (Control)	0.03
91-22-5	Quinoline	0.03
495-40-9	n-Butyrophenone	0.03
64-04-0	2-Phenethylamine	0.03
1797-74-6	Allyl phenylacetate	0.02
95-92-1	Diethyl oxalate	0.02
695-06-7	gamma-Hexalactone	0.02
5146-66-7	3,7-DiMe-2,6-octadienenitrile	0.02
542-55-2	Isobutyl formate	0.02

123-11-5	p-Anisaldehyde	0.02
98-01-1	2-Furaldehyde	0.02
541-85-5	5-Methyl-3-heptanone	0.02
141-05-9	Diethyl maleate	0.02
104-67-6	gamma-Undecanolactone	0.02
103-82-2	Phenylacetic acid	0.01
10031-92-2	Ethyl 2-nonynoate	0.01
79-31-2	Isobutyric acid	0.01
89-79-2	(-)-Isopulegol	0.01
119-36-8	Methyl salicylate	0.01
105-90-8	Geranyl propionate	0.01
106-65-0	Dimethyl succinate	0.01
106-73-0	Methyl heptanoate	0.01
123-68-2	Allyl hexanoate	0.01
34047-39-7	4-Methylthio-2-butanone	0.01
6728-26-3	trans-2-Hexenal	0.00
288-47-1	Thiazole	0.00
540-07-8	Amyl hexanoate	-0.00
60-12-8	2-PhenylEt alcohol	-0.00
142-92-7	Hexyl acetate	-0.00
35466-83-2	Allyl Me carbonate	-0.00
106-32-1	Ethyl caprylate	-0.00
589-38-8	3-Hexanone	-0.00
764-48-7	Ethylene glycol vinyl ether	-0.01
93-58-3	Methyl benzoate	-0.01
5454-28-4	Butyl heptanoate	-0.01
67883-79-8	cis-3-Hexenyl tiglate	-0.01
40015-15-4	1,1-Dimethoxy-2-(Methio)ethane	-0.01
13679-61-3	Methyl 2-thiofuroate	-0.01
89-82-7	(R)-(+)-Pulegone	-0.01
106-22-9	Citronellol	-0.01
590-86-3	3-Methylbutyraldehyde	-0.01
107-75-5	3,7-DiMe-7-hydroxyoctanal	-0.02
105-68-0	Isoamyl propionate	-0.02
7492-70-8	Butyl butyryllactate	-0.02
98-86-2	Acetophenone	-0.02
123-51-3	3-Methylbutanol	-0.02
106-30-9	Ethyl heptanoate	-0.02
629-14-1	Ethylene glycol diEt ether	-0.02
138-86-3	Dipentene	-0.02
78-70-6	Linalool	-0.02
93-89-0	Ethyl benzoate	-0.03
122-70-3	2-Phenylethyl propionate	-0.03
15707-24-1	2,3-Diethylpyrazine	-0.03
105-87-3	Geranyl acetate	-0.03
105-54-4	Ethyl butyrate	-0.03
6622-76-0	Methyl tiglate	-0.03
15707-23-0	2-Ethyl-3-methylpyrazine	-0.03
7540-53-6	Citronellyl valerate	-0.04
300-57-2	Allyl benzene	-0.04
137-00-8	4-Methyl-5-thiazoleethanol	-0.04
623-70-1	Ethyl crotonate	-0.04
53448-07-0	trans-2-Undecenal	-0.04
67-56-1	Methanol	-0.05
624-48-6	Dimethyl maleate	-0.05
108-98-5	Thiophenol	-0.05
123-66-0	Ethyl hexanoate	-0.05
1009-14-9	Valerophenone	-0.05
123-32-0	2,5-Dimethylpyrazine	-0.05
589-98-0	3-Octanol	-0.05
97-99-4	Tetrahydrofurfuryl alcohol	-0.05
470-67-7	Cineole	-0.05
100-52-7	Benzaldehyde	-0.06
107-87-9	2-Pentanone	-0.06
1128-08-1	Dihydrojasmone	-0.06
78-93-3	2-Butanone	-0.07
925-78-0	3-Nonanone	-0.08
543-49-7	2-Heptanol	-0.09
2396-83-0	Ethyl 3-hexenoate	-0.09
51729-83-0	Methyl isopropyl carbonate	-0.09
562-74-3	Terpinen-4-ol	-0.09
6976-93-8	2-Methoxyethyl methacrylate	-0.10
591-78-6	2-Hexanone	-0.10
590-01-2	Butyl propionate	-0.11
629-19-6	Propyl disulfide	-0.11
108-48-5	2,6-Lutidine	-0.11
20487-40-5	tert-Butyl propionate	-0.11
112-30-1	1-Decanol	-0.11
110-93-0	6-Methyl-5-hepten-2-one	-0.13
5837-78-5	Ethyl tiglate	-0.13
110-62-3	Valeraldehyde	-0.13
623-36-9	2-Methyl-2-pentenal	-0.13
100-66-3	Anisole	-0.13
111-13-7	2-Octanone	-0.14
110-43-0	2-Heptanone	-0.15
124-13-0	Octanal	-0.15
25152-84-5	trans, trans-2,4-Decadienal	-0.15
68480-28-4	3-Methylbut-2-enyl formate	-0.17
19700-21-1	Geosmin	-0.20
111-71-7	Heptanal	-0.28
121-45-9	Trimethyl phosphite	-0.32
66-25-1	Hexanal	-0.33
629-41-4	1,8-Octanediol	-0.45

Supplemental Table T2

Abbreviations of Descriptor Blocks as used in the manuscript

Abbreviation	Descriptors
FGROUP	FUNCTIONAL GROUP COUNTS
2DAUTO	TWOD AUTOCORRELATIONS
3DMORSE	THREEDMORSE
AFRAG	ATOMCENTRED FRAGMENTS
BCUT	BURDEN EIGENVALUES DESCRIPTORS
CONST	CONSTITUTIONAL
CIND	CONNECTIVITY INDICES
EAIND	EDGE ADJACENCY INDICES
EVIND	EIGENVALUE INDICES
GEO	GEOMETRICAL
GETAWAY	GETAWAY
MOLPROP	MOLECULAR PROPERTIES
RAND	RANDIC MOLECULAR PROFILES
RDF	RDF
TOPO	TOPOLOGICAL
WHIM	WHIM
WPATH	WALK PATH COUNTS

Decoding Odor Attraction and Intensity in the *Drosophila* brain

Antonia Strutz[a], Jan Soelter[b], Amelie Baschwitz[a], Abu Farhan[a], Veit Grabe[a], Jürgen Rybak[a], Markus Knaden[a], Michael Schmuker[b], Bill S. Hansson[a], Silke Sachse[a,*]

[a] *Department of Evolutionary Neuroethology, Max Planck Institute for Chemical Ecology, Jena, Germany*
[b] *Free University Berlin, Neuroinformatics & Theoretical Neuroscience, Department for Biology, Pharmacy and Chemistry, Berlin, Germany*

Abstract

To internally reflect the sensory environment, animals create neural maps encoding the external stimulus space. From that primary neural code relevant information has to be extracted for accurate navigation. Feature extraction and integration of stimulus modalities have mainly been studied in the visual system, while they remain unknown in the olfactory system. In this study, we analyzed if and how different odor features as hedonic valence and intensity are functionally integrated in the lateral horn (LH), a brain center that is assumed to be involved in innate olfactory behavior. We characterized an olfactory processing pathway, comprised of inhibitory projection neurons (iPNs), that target the LH exclusively at morphological, functional and behavioral levels. We demonstrate that iPNs are subdivided into two morphological groups that extract information from distinct glomerular subsets in the antennal lobe and integrate this into non-overlapping regions in the LH. Selective silencing of iPNs via RNAi severely diminished flies' attraction behavior and odor intensity perception. Functional imaging of the LH and single neuron tracing via photoactivated GFP revealed spatially segregated integration of both features into two non-overlapping LH response domains. Moreover, using two-photon laser-mediated transection we identified a third LH domain comprising third-order neurons that are selectively tuned to repellent odors. We provide evidence for a feature-based, spatially segregated activity map in the LH and elucidate its role as a center for integrating behaviorally relevant olfactory information.

1. Introduction

To navigate the environment in a way that optimizes their survival and reproduction, animals have evolved sensory systems. These have three essential tasks: First, the external world has to be translated into an internal representation in the form of an accurate neural map. Second, the neural map has to be readable and interpretable, i.e., the generated neural code must allow common attributes to be extracted across stimuli to enable the animal to make the best decisions. Third, the animal has to be able to adapt to environmental changes and to form a sensory memory of new stimuli. Many studies have been dedicated to unraveling the primary

*To whom correspondence should be addressed:
Email: ssachse@ice.mpg.de

transformation from a stimulus into an initial neural representation within various sensory systems [1-3] and to elucidating neuronal plasticity and sensory memory formation in higher-level processing centers [4,5]. In contrast, the ability to extract features and integrate stimulus modalities have so far mainly been studied in the visual system [6-8]; how these crucial functions are accomplished within the olfactory system remains unknown.

The olfactory system of the vinegar fly *Drosophila melanogaster* provides an excellent model system for deciphering olfactory processing mechanisms, since it displays remarkable similarities to the mammalian system but is less complex and highly genetically tractable. Like other sensory systems, the olfactory system employs a spatio-temporal map to translate the variables in chemosensory space into neuronal activity patterns in the brain. This map emerges when the olfactory sensory neurons (OSNs) with the same chemosensory receptors converge into one exclusive glomerulus in the antennal lobe (AL) which represents the equivalent to the mammalian olfactory bulb [2,9-11]. Glomeruli, the functional and morphological units of the AL, are microcircuits comprising OSNs, multiglomerular local interneurons (LNs) and uniglomerular output neurons, so-called excitatory projection neurons (ePNs) [2,12] that convey the olfactory information to higher brain centers, as the mushroom body calyx (MBc) and the lateral horn (LH) [13]. The stringent spatial arrangement of OSNs and ePNs in the AL generates a spatial map containing characteristic combinatorial glomerular activity patterns for all odorants [14-17]. The MBc is involved in olfactory memory formation [4] and enables a contextualization of the odor space [18]. By exclusion, the LH is believed to be involved in innate olfactory behavior [19,20]. Excitatory PNs retain the sensory information encoded in the AL and form glomerulus-dependent, stereotypic axonal terminal fields in the LH [21-23]. Compartmentalization in the LH has been observed in form of a spatial segregation of ePNs innervating specific glomerular subgroups [23], fruit and pheromone odor information processing ePNs [20] as well as ammonia and amine versus carbon dioxide coding ePNs [24].

Like many other sensory networks, the olfactory circuit of the fly contains spatially distinct pathways to the higher brain, namely the inner, middle and outer antennocerebral tract (iACT, mACT and oACT) [25]. Notably, the mACT projects from the AL to the LH exclusively and consists of inhibitory PNs (iPNs), which exhibit also uniglomerular but mainly multiglomerular AL innervations [20,26-29]. Together, the PN populations processes information on dual olfactory pathways [29,30], as do processing mechanisms in other sensory modalities [8], and most likely accomplish different olfactory behaviors. The mainly multiglomerular AL pattern of iPNs suggests that these neurons extract characteristic stimulus features from the AL code and re-integrate this information into the LH to mediate innate odorant-guided behavior. This assumption is further supported by a recent study showing that LH neurons receive a biased input from AL glomeruli [31], while the connectivity in the MBc is rather probabilistic [18,32]. However, it still remains open if and how different odor features as hedonic valence or intensity are functionally integrated in the LH. In this study, we characterized and dissected the iPN olfactory processing pathway at morphological, functional and behavioral levels. Our results provide evidence for a feature-based, spatially segregated activity map in the LH and thus

expand its role as a center for integrating behaviorally relevant olfactory information.

2. Results

2.1. iPNs receive cholinergic input and provide feed-forward inhibition to the lateral horn

In order to unravel the role of iPNs within the olfactory circuitry, we first analyzed their morphological properties in comparison to ePNs. Notably, cell bodies of iPNs are exclusively located in the ventral cell cluster which consists of 50 iPNs [27] that project via the mACT to the LH, thereby bypassing the MBc [26] (Fig. 1A-B). In contrast, ePN somata are located anterodorsally and laterally of the AL, and their axons project through the iACT or oACT to the MBc and the LH [13,21,22,27]. We labeled iPNs and ePNs simultaneously *in vivo* using GH146-GAL4 and MZ699-GAL4 that label the majority of ePNs (60%) and iPNs (86%), respectively [27]. Double-labeling shows that both PN populations innervate overlapping regions in the AL and the LH, while a small posterior-lateral LH area is targeted only by ePNs (Fig. 1A and S1A). In GH146-positive (GH146+) PNs, immunolabeling reveals GABA production in all 6 PNs of the ventral cell cluster [33], whereas ePNs of this line are exclusively cholinergic [34]. For the 45 MZ699-positive (MZ699+) iPNs [27], GAD1 (glutamic acid decarboxylase) *in situ* hybridizations imply GABA synthesis [28], which we verified via immunostaining (Fig. S1B-B).

To determine the polarity of both PN populations, we expressed UAS-Dα7:mcherry to tag postsynaptic input sites by labeling acetylcholine receptors (AChR) (Fig. 1C-C), and UAS-Syt:HA to label presynaptic terminals (Fig. 1D-D). Both neuronal populations reveal dense Dα7:mcherry fluorescence in the AL, indicating the AL as their cholinergic input site. In the LH, the AChR-reporter was detected only in putative third-order LH neurons while it was absent in both PN types. An analysis of the output site revealed a dense distribution of presynaptic terminals for both PN populations in the LH. Interestingly, while ePNs possess output sites in the AL, we did not observe any presynaptic terminals of iPNs indicating a lack of feedback inhibition [28]. All observations were verified using the presynaptic reporter UAS-brp:mcherry and the postsynaptic marker DenMark (data not shown).

2.2. Dendrites of iPNs innervate two-thirds of olfactory glomeruli

Since both PN subtypes receive OSN input, we analyzed the precise glomerular innervation to unravel how selectively iPNs acquire information in the AL (Fig. 2A). To allow glomerulus identification *in vivo*, we generated a transgenic fly carrying elav-n-synaptobrevin:DsRed (END1-2) to express the presynaptically targeted fusion protein under the control of the neuron-specific elav promotor (Fig. S2A). The reconstruction and identification of all AL glomeruli provided 53 glomeruli, of which 75% were innervated by MZ699+ iPNs (40) while 70% (37) were covered by GH146+ ePNs (Fig. 2B, and S2B). 55% of all glomeruli were innervated by both lines. Notably, dendritic MZ699 innervation density was not homogeneous. Certain glomeruli were densely innervated (e.g. DM2, DM4 and DM5), while others did not reveal any postsynaptic sites (e.g. DL1, DL4 and DL5). Hence MZ699+ iPNs target specific glomerular subsets selectively, which suggests that these neurons have a particular function within the olfactory network.

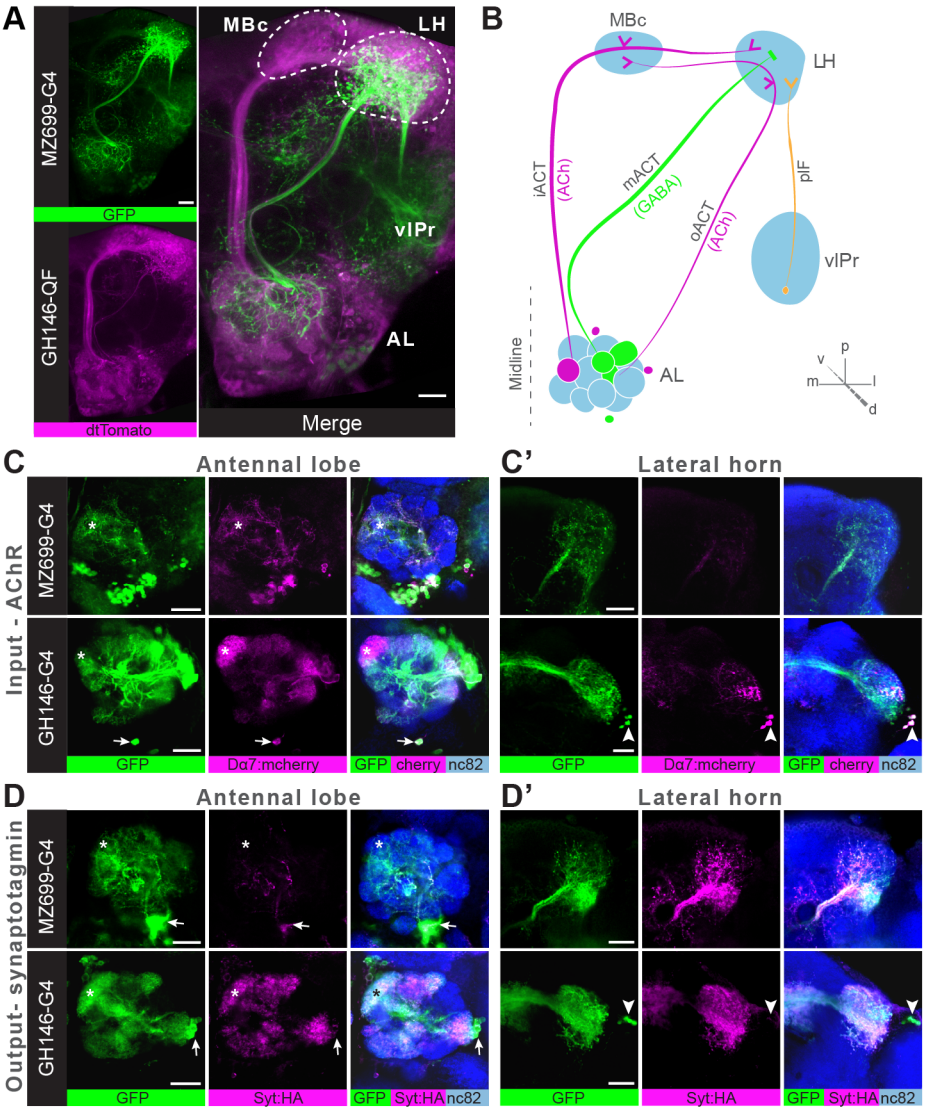

Figure 1: **Anatomical characterization of excitatory and inhibitory projection neurons.** (A) The simultaneous labeling of inhibitory projections neurons (iPNs, labeled by MZ699-GAL4;G-CaMP) and excitatory projection neurons (ePNs, labeled by GH146-QF;dtTomato) in vivo reveals distinct projections to the lateral horn (LH). All iPNs bypass the mushroom body calyx (MBc) and innervate the LH exclusively. The MZ699 line labels a few ventrolateral protocerebral neurons (vlPr neurons) projecting via the posterior lateral fascicle (plF) from the ventrolateral protocerebrum (vlPr) to the LH. (B) Schematic of the PN connectivity relay from the antennal lobe (AL) to higher brain centers (ePNs in magenta, iPNs in green, and vlPr neurons in orange). (C-C) Whole-mount and vibratome immunostainings in flies carrying UAS-Dα7:mcherry as a marker for acetyl choline receptors, G-CaMP as a neuronal marker and nc82 as a general neuropil marker in MZ699-GAL4 (top) or GH146-GAL4 (bottom), in the AL (C) and the LH (C). Asterisk denotes the DA1 glomerulus and arrowheads point to somata of ventral PNs at the AL and the LC1 cluster of third order neurons in the LH, respectively. (D-D) Immunostainings in flies carrying UAS-Syt:HA as a presynaptic marker in MZ699-GAL4 (top) or GH146-GAL4 (bottom), in the AL (D) and the LH (D). Scale bar, 20μm.

2.3. Calcium signals in the lateral horn spatially segregate into distinct response domains

Probabilistic synaptic density maps of GH146+ PNs predicted a regionalized neuronal activity in the LH [20]. Do iPNs functionally segregate in a comparable way? To address this

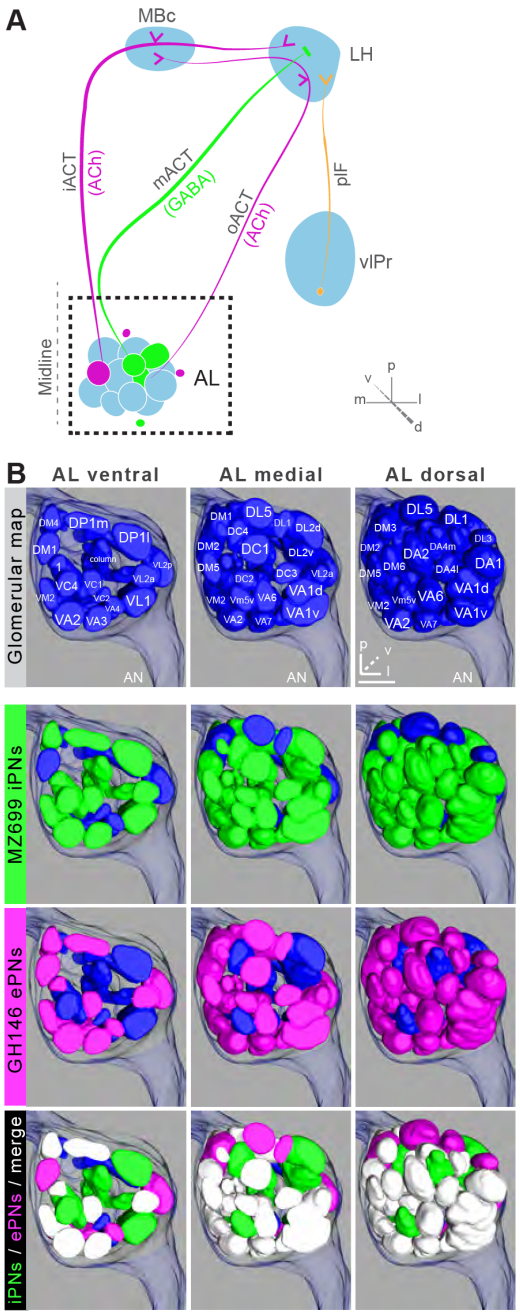

Figure 2: **Detailed glomerular innervations of excitatory and inhibitory projection neurons in the AL.** (A) Schematic of the olfactory circuit with the investigated area highlighted. (B) Above, complete glomerular assignment of the AL neuropil (right AL), labeled with elav-n-synaptobrevin:DsRed (END1-2). Below, glomerular innervations of both PN populations related to in vivo images in Fig. S2A. Depicted are the ventral level ($\approx -40\mu m$), the medial level ($\approx -20\mu m$) and the dorsal view onto the AL. Color annotation: blue glomeruli are not innervated by any of the used GAL4-lines; green glomeruli are innervated by MZ699+ iPNs and magenta by GH146+ ePNs; white glomeruli are innervated by both enhancer trap lines. Scale bar, $20\mu m$.

question, we expressed the Ca^{2+}-sensitive reporter G-CaMP3.0 [35,36] in iPNs using MZ699-GAL4 and performed functional imaging in the LH (Fig. 3A-C). We initially tested three of the most relevant odors for *Drosophila* at different concentrations: acetoin acetate, an attractive byproduct of the yeast fermentation process, balsamic vinegar, an attractive natural odor mixture, and benzaldehyde, a well-known fly repellant [37-39]. We observed that odor evoked Ca^{2+} responses separate in certain regions of the LH in an odor-specific and concentration-dependent manner (Fig. 3C). Acetoin acetate and balsamic vinegar evoked Ca^{2+} activity in spatially similar regions. At higher concentrations, an additional region was recruited. Benzaldehyde elicited no response at very low concentrations, but induced clear activity at median and high concentrations in a third region, which was completely separate from the regions activated by the other two odors. Observed patterns were reproducible and stereotypic, as shown for the stimulation with the odor 1-octen-3-ol (Fig. 3D).

Due to the lack of morphological landmarks in the LH, functional data were analyzed using the pattern recognition algorithm Non-Negative Matrix Factorization (NNMF) [40], which automatically extracts spatial areas possessing a common distinct time-course, further termed LH odor response domains (ORDs). The NNMF analysis extracted three clearly reproducible and spatially robust ORDs (Fig. 3E). Notably, ORDs occupying common temporal kinetics exhibited highly stereotypic spatial patterns. We termed the ORDs LH-PM (LH-posterior-medial), LH-AM (LH-anterior-medial) and LH-AL (LH-anterior-lateral) according to their anatomical positions. To validate our observations, we extended our stimulus array to 11 additional odorants and applied each at three concentrations. Odorants were chosen according to chemical classes, hedonic valence and biological value. Hence, the odor set included acids, lactones, terpenes, aromatics, alcohols, esters, ketones and the natural blend, balsamic vinegar. Remarkably, analysis of the additional odorants revealed neuronal activity exclusively within the three described ORDs (Fig. 3F). Furthermore, median NNMF-extracted Ca^{2+} response traces with indicated statistical quartiles illustrate very low variability and highly reproducible LH signals. The LH-PM area chiefly revealed constant odor-evoked responses across concentrations, while the LH-AM and LH-AL were mainly activated at very high odor concentrations by distinct odorants. The global responsiveness within separate ORDs in the LH substantiates our anatomical finding of a broad cholinergic AL input to MZ699+ iPNs which converges into three spatially

Figure 3 *(following page)*: **Odors evoke specific and stereotypic calcium responses in the LH subdivided into three distinct odor response domains.** (A) Schematic of the olfactory circuit with the investigated area highlighted. (B) RAW image of the LH (top picture) depicting the recorded area of figures (C-E) and the false color image (bottom picture) during the solvent application. The $\Delta F/F$ scale bar applies for all false color-coded pictures; the alpha-bar for the pixel participation x_k of the indicated colors applies for (E-F). (C) Representative LH Ca^{2+} responses ($\Delta F/F$ %) of acetoin acetate, balsamic vinegar and benzaldehyde at three concentrations. Numbers in the lower right corner indicate individual maxima. (D) Odor-evoked Ca^{2+} responses (F/F %) are exemplary depicted for 1-octen-3ol at three concentrations in four animals. (E) NNMF-extracted LH odor response domains (ORD) of four representative animals: three LH ORDs were fully reproducible after being extracted from all measured animals. Domains classified as identical are similarly color-coded: the green ORD is located in the posterior-medial region of the LH (LH-PM); blue, in the anterior-medial (LH-AM), and red in the anterior-lateral LH area (LH-AL). The alpha-bar for green, blue and red shades is placed in (B). (F) Left, schematic outlines of the LH with indicated ORDs. Right, median activity traces of all odors at three concentrations are depicted for each colored ORD. Shadows represent lower and upper quartiles ($n = 6 - 7$).

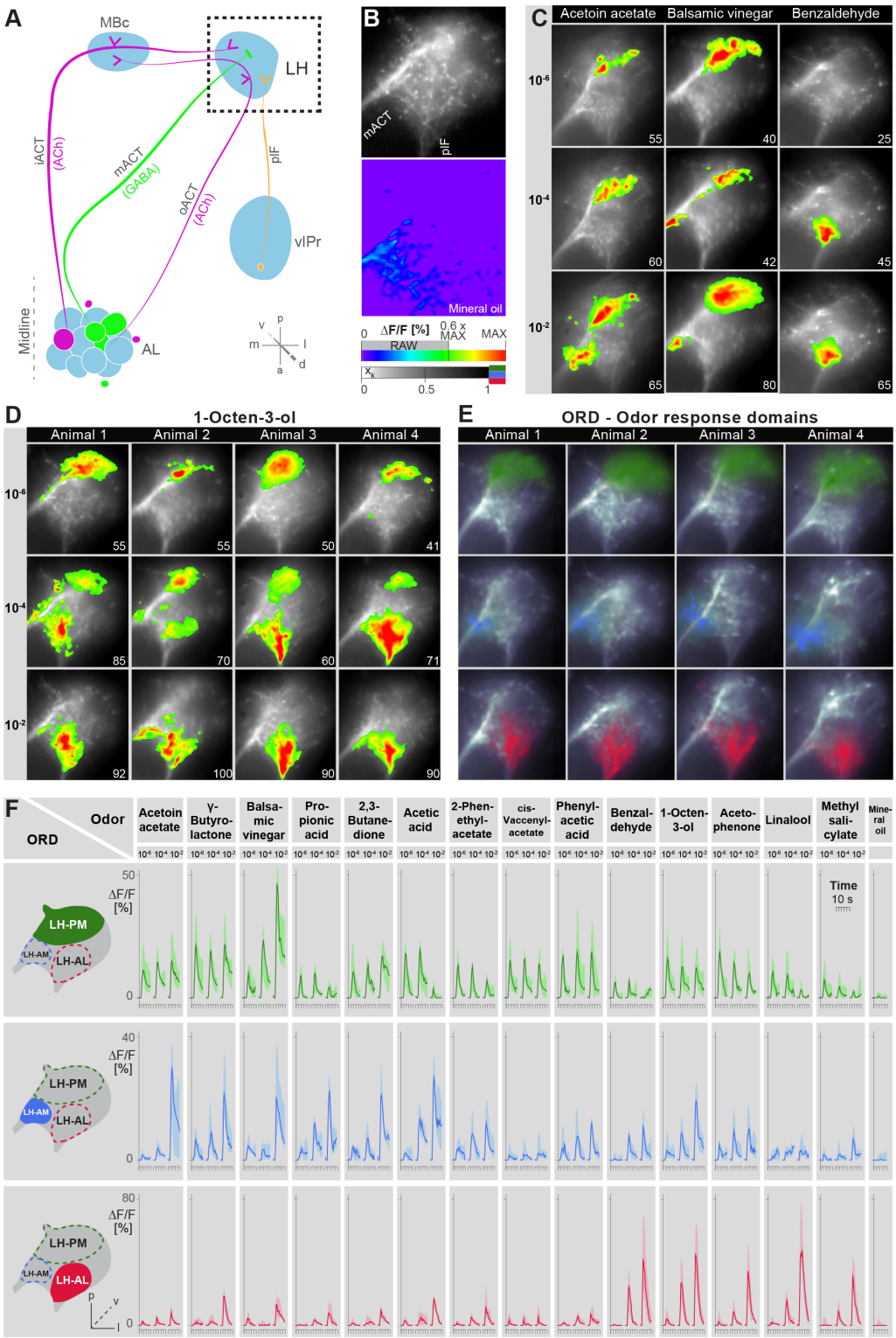
A
MBc
LH
iACT
(ACh)
mACT
(GABA)
oACT
(ACh)
lPF
vlPr
Midline
AL
B
mACT
lPF
Mineral oil
ΔF/F [%]
RAW
MAX
C
Acetoin acetate
Balsamic vinegar
Benzaldehyde
D
1-Octen-3-ol
Animal 1
Animal 2
Animal 3
Animal 4
E
ORD - Odor response domains
F
ORD
Odor
Acetoin acetate
γ-Butyro-lactone
Balsa-mic vinegar
Pro-pionic acid
2,3-Butane-dione
Acetic acid
2-Phen-ethyl-acetate
cis-Vaccenyl-acetate
Phenyl-acetic acid
Benzal-dehyde
1-Octen-3-ol
Aceto-phenone
Linalool
Methyl sali-cylate
Mine-ral oil
ΔF/F [%]
Time
10 s
LH-PM
LH-AM
LH-AL

regionalized and stereotypic LH activity domains.

2.4. iPNs can be divided into two morphological classes

We next investigated if the spatially regionalized odor-evoked response patterns are reflected in the axonal terminal fields of MZ699+ iPNs in the LH. To analyze these neurons at the single neuron level, we performed neural tracing by employing a genetically encoded photoactivatable GFP (PA-GFP) [41-43]. The photoconversion of all MZ699+ neurons leaving the AL confirmed the homogeneous distribution of iPN neurites in the LH and the sparse innervation of the posterior-lateral region as mentioned above (Fig. 4A). Next we illuminated PA-GFP in single somata to selectively label individual MZ699+ iPNs from the soma up to the farthest axonal terminals in the LH. Individual iPNs were reconstructed and transformed into a reference brain using the END1-2 background to align neurons of different individuals. Interestingly, MZ699+ iPNs could be assigned to two morphological classes based on their innervation pattern in the LH (Fig. 4B-C). As expected from the extracted ORDs, one iPN group diverged to the LH-PM (n=7 in 21 neuronal recontructions), while a second group extended their axonal terminations within the LH-AM (n=7 in 21 neuronal recontructions). Since the MZ699-GAL4 line labels also neurons connecting the LH and the ventrolateral protocerebrum (vlPr) [26,29], we illuminated a small fraction of the posterior lateral fascicle (plF) to target these putative third-order neurons (Fig. 4A). The plF comprised axons of ventrolateral protocerebral neurons (vlPr neurons), which bifurcated within the LH-AL (Fig. 4D). Combinations of all registered neuron types within the assigned zones revealed that iPNs of the LH-AM and vlPr neurons of the LH-AL region intermingle (Fig. 4E-F).

We did not observe any clear panglomerular innervations of individual MZ699+ iPNs that spanned the entire AL. Instead, MZ699+ iPNs develop mainly oligoglomerular patterns innervating on average 5 ± 4 glomeruli (mean±SD), which are not necessarily in close proximity. After classifying all registered neurons according to their LH zones along with their glomerular innervations, we noted a spatial subdivision of MZ699+ iPN dendritic fields in the AL (Table S1). Whereas LH-PM iPNs extended dendrites mainly into glomeruli from the ventro- or dorsomedial area of the AL (e.g. DM4, DM2, VM7, VM5d), iPNs targeting the LH-AM zone innervated glomeruli ranging from the ventro- and dorsoanterior to the dorsocentral region (e.g. DC3, VC1, VA6, VL1). We observed that a glomerulus is typically innervated by only LH-PM iPNs or LH-AM iPNs. However, we also found a few cases where a glomerulus can be innervated

Figure 4 *(following page)*: **iPNs can be classified according to their projection pattern in three distinct LH zones.** (A) Complete population of MZ699+ iPNs labeled using PA-GFP (left image), the posterior-lateral LH region is encircled, arrowhead indicates the final common projection point of iPN axons. Middle image: photoactivation of all vlPr neurons of the MZ699-GAL4 line that project from the LH to the vlPr via the plF. Right image: exemplary single iPN, labeled by photoconverting PA-GFP in a single soma (arrow). Scale bar, $20\mu m$. (B) Framed images: neuronal reconstruction of all iPNs projecting to the LH-PM zone with outlined olfactory neuropils. View from dorsal (left) and lateral (right). Right part represents two exemplary registered individual iPNs. (C) Neuronal reconstruction of all iPNs projecting into the LH-AM zone, images are arranged as in (B). (D) Neuronal reconstruction of vlPr neurons projecting through the plF to the LH-AL zone. (E) Combination of all registered neurons. (F) Dual combinations of all registered neurons with their projections in the LH.

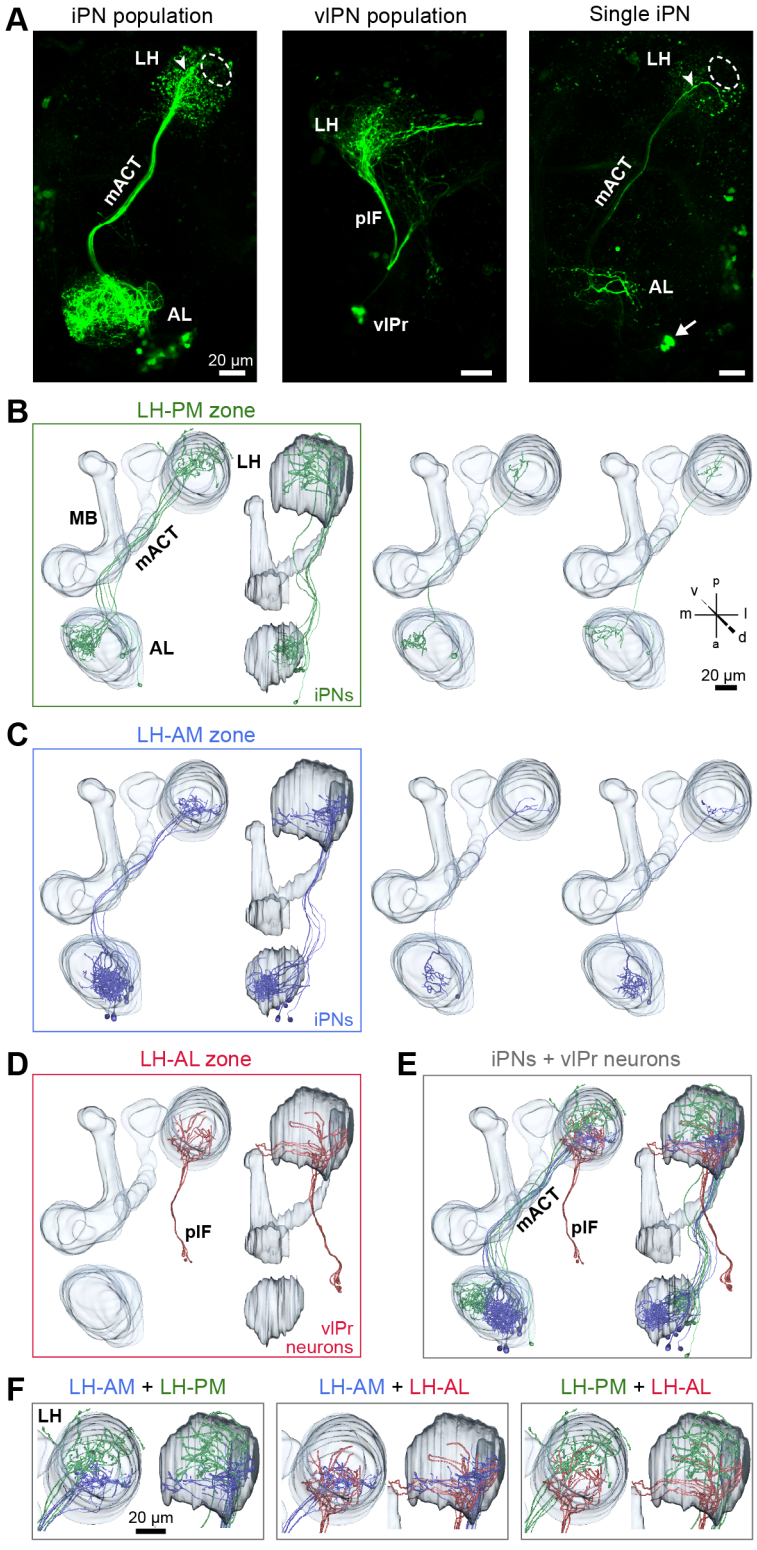
A
iPN population
vlPN population
Single iPN
LH
mACT
AL
20 µm
LH
plF
vlPr
LH
mACT
AL
B
LH-PM zone
MB
mACT
LH
AL
iPNs
P
V
m
l
a
d
20 µm
C
LH-AM zone
iPNs
D
LH-AL zone
plF
vlPr
neurons
E
iPNs + vlPr neurons
mACT
plF
F
LH-AM + LH-PM
LH-AM + LH-AL
LH-PM + LH-AL
LH
20 µm

by both iPN types (e.g. glomeruli D and DC2). In addition we observed a few uniglomerular MZ699+ iPNs innervating glomeruli DA1 and VL1 (n=4 in 21 neuronal reconstructions), confirming previous studies [27], which target the LH-AM region (Table S1). Moreover, we identified three MZ699+ iPNs that did not innervate the AL and sent their axons to the LH and/or the MBc.

2.5. Odor response domains contain the activity of distinct neuronal populations

To illustrate higher-order connectivity, we labeled the three major neuron types, i.e. MZ699+ iPNs, GH146+ ePNs and vlPr neurons, targeting the LH within the olfactory circuitry using PA-GFP (Fig. 5A). Since our observed Ca^{2+} responses in the LH-AL region might reflect activity from vlPr neurons rather than iPNs, we dissected the neuronal contributions within each extracted ORD by conducting transection experiments using two-photon laser-mediated microdissection (Fig. 5B). By transecting the mACT, we aimed at abolishing LH-responses deriving from MZ699+ iPNs, while cutting the plF connection should eliminate potential odor-evoked vlPr neuron activity. To achieve unambiguous and comparable results, functional imaging was performed in both brain hemispheres simultaneously. Immediately after the intact brain areas were imaged, the tracts were selectively transected on one brain side each (Fig. 5C) and the imaging procedure was repeated. We applied a reduced odor set that elicited activity in all ORDs and performed NNMF for pre- and post-lesion recordings. Transecting the mACT significantly reduced responses in the LH-PM and LH-AM region, whereas LH-AL responses were significantly abolished by plF-ablation (Fig. 5D). Notably, we observed that LH-AL responses to some odors were significantly increased after mACT transection as a consequence of the suppression of iPN inhibition of vlPr neurons according to Liang et al. [29]. Hence, activity in the LH-PM and LH-AM domain can be assigned to MZ699+ iPNs, while LH-AL activity is mainly evoked by vlPr neurons (Fig. 5E).

Figure 5 *(following page)*: **Distinct odor response domains in the LH constitute neuronal activity of iPNs and vlPr neurons.** (A) Representation of all ePNs (magenta) and iPNs (green) labeled by GH146-GAL4 and MZ699-GAL4 using PA-GFP, respectively. Photoactivation of vlPr neurons (orange, MZ699-GAL4) connecting the LH and the vlPr via the plF. The overlay image depicts a pseudo-merge image of the different GAL4 driver lines. (B) Schematic of the olfactory circuit with integrated layout of the transection experiment. After simultaneous Ca^{2+} imaging of bilateral LHs, the ipsilateral plF and contralateral mACT was transected (red zigzag line) with an infrared laser (dashed red arrow). (C) Projection images of a $7\mu m$ stack of the LH area prior and post transection. Left images, mACT transected; right image, plF transected. The ablated region is indicated by the dashed red arrow. Scale bar, $20\mu m$. (D) Median time traces displaying percental change of $\Delta F/F$ values for indicated ORDs prior to post transection of the mACT (green, left) and the plF (orange, right) for different odorants. Significant changes of odor-evoked Ca^{2+} signals due to transection are shown in the column SIG difference. Differences were tested with a two-tailed paired Students t-test ($p < 0.05$). Color codes are indicated by the corresponding scale bar below, $n = 4 - 5$. Transecting the mACT eliminates Ca^{2+} signals in the LH-PM and LH-AM domain, while lesioning the plF significantly abolishes LH-AL responses. Notably, the LH-AL domain is significantly stronger activated after mACT transection following application of 1-octen-3-ol and γ-butyrolactone. (E) Summarized cartoon of the neuron populations contributing to ORD activity prior and post transection of axons of iPNs or vlPr neurons.

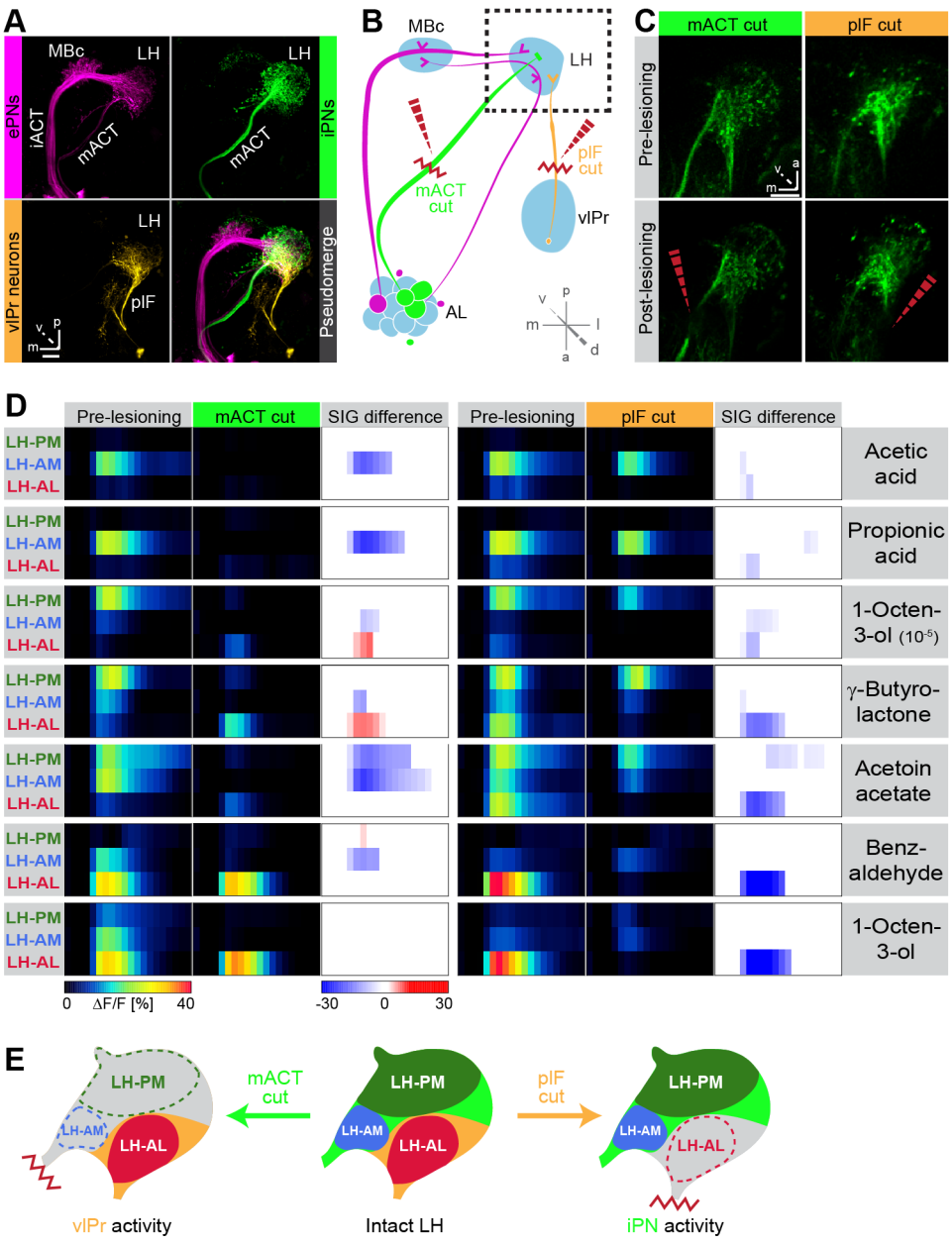
A
ePNs
iACT
MBc
LH
mACT
LH
mACT
iPNs
vlPr neurons
LH
plF
Pseudomerge
B
MBc
LH
mACT cut
plF cut
vlPr
AL
C
mACT cut
plF cut
Pre-lesioning
Post-lesioning
D
Pre-lesioning
mACT cut
SIG difference
Pre-lesioning
plF cut
SIG difference
LH-PM
LH-AM
LH-AL
Acetic acid
Propionic acid
1-Octen-3-ol (10-5)
γ-Butyro-lactone
Acetoin acetate
Benz-aldehyde
1-Octen-3-ol
0 ΔF/F [%] 40
-30 0 30
E
LH-PM
LH-AM
LH-AL
mACT cut
plF cut
vlPr activity
Intact LH
iPN activity

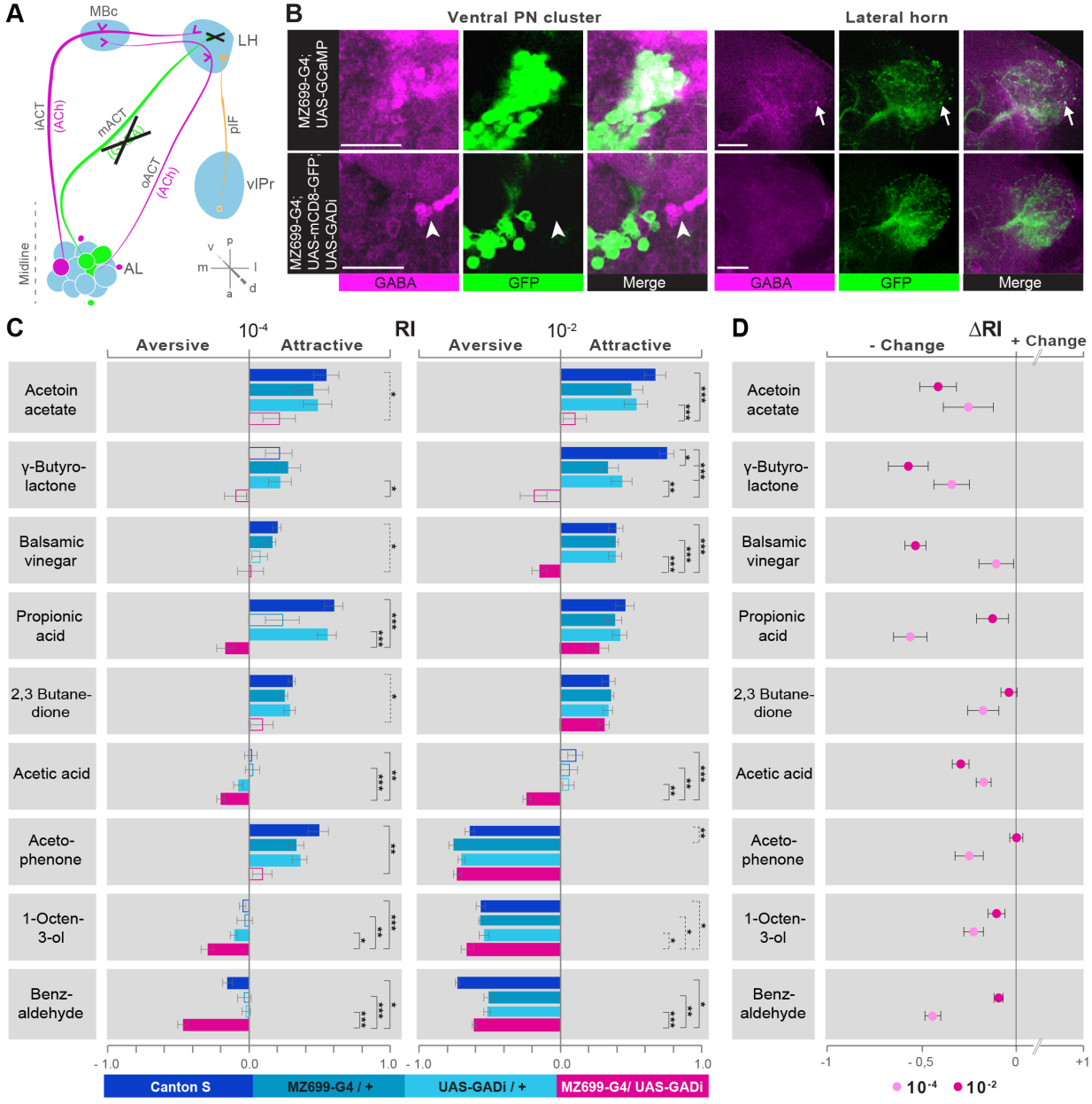

Figure 6: **iPN GABA release in the LH mediates odor attraction behavior.** (A) Experimental layout: iPN GABA production was selectively silenced via GADi expression in MZ699+ iPNs; ePN and vlPr neuron activity remained unaffected. (B) Immunostaining against GABA and GFP within AL somata (left) and LH neurites (right) of iPNs with intact (top) and silenced GABA production (bottom). GADi flies show GABA signals in somata of iPNs labeled by GH146 only (arrowhead). The arrow points to an exemplary GABA-positive bouton in the LH. Scale bar, 20μm. (C) Averaged response indices (RIs) for wild-type flies (dark blue), parental controls (light blue) and experimental animals (magenta) for 9 odorants at two concentrations. Empty boxes display no response (Wilcoxon signed-rank test). Deviation of the RI against controls was tested with Dunn's Multiple Comparison (solid line) or Dunn's selected Pairs (dashed line). Error bars represent SEM. (D) RI differences between GADi flies and averaged parental controls. RI differences are negative for all but one odor indicating that GADi expression shifts odor-guided behavior towards aversion. Error bars indicate SEM.

2.6. iPN activity in the lateral horn mediates flies attraction to odors

We next addressed the behavioral relevance of MZ699+ iPN activity in the LH for innate odor-guided behavior. To precisely target iPN function, we expressed an RNAi construct against glutamic acid decarboxylase 1 (GADi) to selectively knock-down the GABA synthesis in MZ699+ iPNs (Fig. 6A). We confirmed the reduction in GABA production via immunostaining (Fig. 6B). Since vlPr neurons are not GABAergic, they were not affected by the RNAi expression (data not shown) [29,44]. Using wild-type flies and parental controls, we conducted T-maze assays [45,46] with 9 of the odorants applied in functional imaging experiments at medium and high concentrations. Notably, flies with silenced MZ699+ iPN GABA production revealed a neutral or aversive behavioral response to attractive odors, while repellent odors evoked an even stronger aversion (Fig. 6C). To compare the T-maze data more accurately, we calculated the average change of behavioral response indices (RIs) between GADi flies and parental controls (Fig. 6D). Indeed, all responses changed in a negative direction, indicating MZ699+ iPNs play a crucial role in mediating attraction behavior. The sole exception involved high concentrations of the most repulsive odor, acetophenone, since this odor had already induced maximum aversion. For some odors, the control flies revealed a different preference for the two concentrations tested, manifested in distinct behavioral responses (e.g. 1-octen-3ol, Fig. 6C). The interruption of MZ699+ iPN GABA-synthesis led to similar responses to both tested concentrations, suggesting that perception of odor intensity was impeded. Overall, these experiments reveal a crucial function of MZ699+ iPNs in mediating attraction behavior and intensity perception by releasing GABA in the LH.

2.7. iPNs integrate positive hedonic valence and odor intensity into separate domains

The behavioral effect of the iPN knock-down suggests that MZ699+ iPNs encode positive hedonic valences as well as odor intensity. To correlate the complete ORD pattern array with innate behavioral preferences, we assigned behavioral RIs for all odors at median and high odor concentrations (Fig. 7A). Since extremely low concentrations rarely evoked any behavioral response, we excluded the 10^{-6} concentration in this analysis. When we plotted median odor-evoked activity in a three-dimensional space defined by the three ORDs, we saw a clear

Figure 7 *(following page)*: **Integration of hedonic valence and odor concentration into ORDs.** (A) Response indices of wild type flies for all odors at median and high concentrations. Odors are sorted from highly aversive (-1, red) to highly attractive (+1, green). (B) 3D-scatter plot of median Ca2+ responses of all odors based on the three ORDs. Odor-dots are labeled due to their RI shown in (A). Same odors at different concentrations are connected with a line: the dot at the end depicts 10^{-2}, the centered dot 10^{-4}, and the end of the line 10^{-6}. Attractive and aversive odor representations form separate clusters. (C-D) Left, schematic LH outlines with colored ORDs corresponding to data on the right. Correlation score r (upper right corner) between median activity and measured RI in T-maze experiments or odor concentration, respectively, with significance denoted below. Students t-test, $*p < 0.05$, $**p < 0.001$. (E) Complete correlation matrices for Ca^{2+} response patterns of OSNs in the AL (left) and iPNs in the LH (right). The odors are arranged according to single linkage clustering of the LH activity patterns. Heatmap color-code refers to the correlation distance scale bar on the right. Correlation distance is defined as 1-r, where r is the Pearson correlation coefficient between the response patterns of two odorants. Odor letters are color-coded according to hedonic valence; 10^{-6} RI values are labeled in grey (complete list right hand).

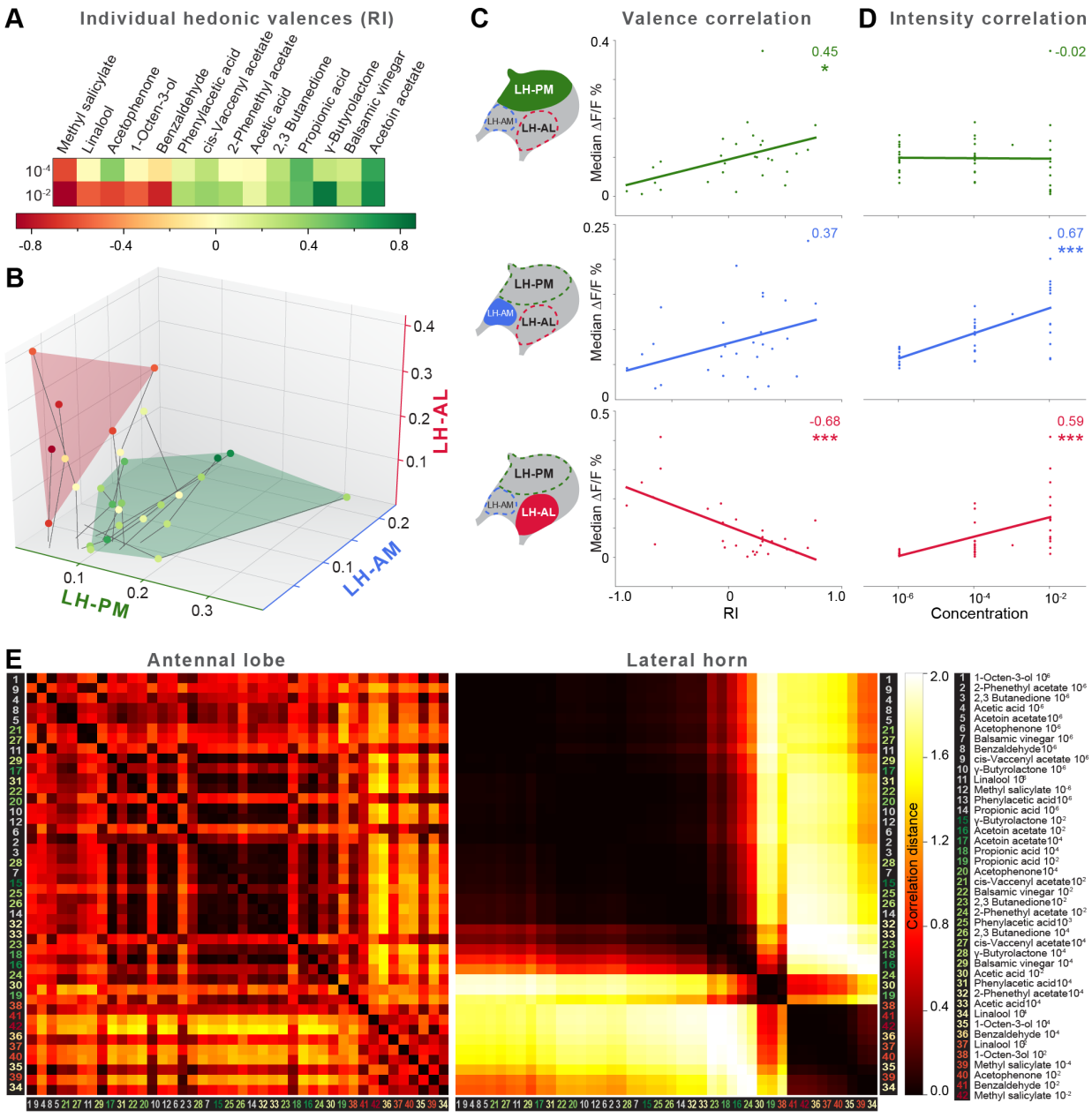
A
Individual hedonic valences (RI)
Methyl salicylate
Linalool
Acetophenone
1-Octen-3-ol
Benzaldehyde
Phenylacetic acid
cis-Vaccenyl acetate
2-Phenethyl acetate
Acetic acid
2,3 Butanedione
Propionic acid
γ-Butyrolactone
Balsamic vinegar
Acetoin acetate
10-4
10-2
-0.8
-0.4
0
0.4
0.8
B
LH-PM
LH-AL
LH-AM
C
Valence correlation
Median ΔF/F %
RI
0.45
*
0.37
***
-0.68
***
D
Intensity correlation
-0.02
0.67
***
0.59
***
Concentration
E
Antennal lobe
Lateral horn
Correlation distance

clustering of responses evoked by aversive and attractive odorants (Fig. 7B). The LH-AL domain, constituted mainly by vlPr neurons, is coding aversive odors, while attractive odors activated only the LH-PM and LH-AM domains that derive from MZ699+ iPNs. This result is in accordance with our finding that iPNs mediate odor attraction.

We next correlated ORD activity to odor valence separately for all ORDs. This evaluation enabled us to analyze iPN and vlPr neuron coding properties apart from each other (Fig. 7C). As expected, the analysis revealed a significant correlation between positive valence and the LH-PM domain, whereas Ca^{2+} responses in the LH-AL were strongly negatively correlated to hedonic valence. The LH-AM domain exhibited a positive but not significant correlation for odor valence. Remarkably, activity within the LH-PM was totally independent of concentration, whereas activity in both anterior domains was significantly correlated to odor intensity (Fig. 7D). Hence, MZ699+ iPNs integrate odor attraction information into the LH-PM domain independent of odor intensity, confirming behavioral experiments. Intensity coding is in turn conducted separately by distinct iPNs within the LH-AM domain. In contrast, putative third-order vlPr neurons projecting into the LH-AL area code both negative valence and odor intensity.

Finally, we wondered if this valence-specific LH representation is already reflected at the primary level of olfactory processing. The odor-evoked responses in iPNs are generally similar to those in OSNs [30], indicating a straight forward transduction of cholinergic OSN responses as reflected in the dense AChR immunoreactivity in iPN dendrites (Fig. 1C). We therefore performed functional imaging of odor-evoked Ca^{2+} dynamics at the AL input level by expressing G-CaMP in OSNs using Orco-GAL4 [47] (Fig. S3). In order to compare the activity patterns at both processing levels, we calculated correlation distances for all pair-wise combinations of odor-evoked response patterns and plotted these with respect to maximal ORD pattern similarity in the LH (Fig. 7E). As expected, odor representations in the LH clearly clustered within three separated parts of the matrix, reflecting our observed ORDs. However, this coding similarity could not predict AL activity patterns, even if the correlation matrix was sorted with respect to pattern similarity in the AL (data not shown).

3. Discussion

We augment our present understanding of the *Drosophila* olfactory circuitry by elucidating a parallel and behaviorally relevant higher-order processing pathway to the LH. Morphological, functional and behavioral approaches provide strong evidence for a functional subdivision of iPNs into neurons coding either odor attraction or odor intensity. Inhibitory properties of iPNs are necessary for innate odor-guided attraction and configure odor-intensity perception. In addition, we characterize a third neural pathway coding odor repellence.

We initially investigated if MZ699+ iPNs fulfill anatomical requirements to constitute a distinct processing channel in addition to ePNs. Both neuronal PN populations receive cholinergic input in the AL. However, in contrast to GH146+ ePNs, which possess presynapses in the AL, MZ699+ iPNs reveal a strict unidirectional polarity and therefore accomplish a feed-

forward inhibition in the LH confirming recent studies [29,44]. A remarkable anatomical feature of MZ699+ iPNs is their glomerular innervation pattern in the AL. Whereas GH146+ ePNs are uniglomerular and retain the topographic code in their axonal arrangement [20-22], most MZ699+ iPNs possess oligoglomerular innervations suggesting that these neurons might not convey precise odor-identity information. In addition, MZ699+ iPNs in the AL diverge only into specific glomerular subsets, and so might be pre-determined to selectively extract common features of distinct odors. We have previously shown that the AL map at the PN level exhibits a spatial segregation of valence representation [48]. Certain glomeruli, which have been classified as aversion coding at the GH146+ ePN level, are omitted by MZ699+ iPNs, whereas most glomeruli classified as attraction coding are particularly densely innervated. These results suggest that within the MZ699+ iPN population, mainly positive odor traits are extracted, whereas the odor information of negative valence is neglected. This conclusion is consistent with the recent finding that one type of LH neurons is receiving input from PNs that mainly innervate glomeruli coding fruity-smelling acetates [31] which represent attractive odor cues [48]. We furthermore demonstrate that the MZ699+ iPN population is split into two morphological classes that possess some degree of spatial segregation in the AL which is strictly maintained within the LH. It has to be kept in mind that we do not cover all iPNs by using MZ699-GAL4. Further experiments characterizing the ~ 6 missing MZ699- iPNs, which are labeled by GH146-GAL4 [27,33], will elucidate if our assumptions apply for the whole iPN population.

So far only a handful neuroanatomical studies targeting GH146+ ePNs have dealt with the question of how olfactory information is integrated and read out by higher brain structures, in particular the LH [20-23]. A recent study that traced the projection pattern of PNs coding ammonia and amines as attractive stimuli and carbon dioxide and acids as repulsive signals suggests that sensory stimuli of opposing valence are represented in spatially distinct areas within the LH [24]. In addition the study by Liang et al. [29] showed that MZ699+ iPNs selectively suppress the activity of vlPr neurons to food odors, while pheromone responses were not affected verifying the assumption that different odor features are processed separately. However, functional evidence for a feature-based, spatially segregated activity map in the LH was so far missing.

To unravel the coding properties of MZ699+ iPNs within the LH, we conducted Ca^{2+} imaging experiments of MZ699+ iPNs in the LH to odorants having different hedonic valences and intensities, and could classify the LH into three functional ORDs. Our neuronal tracing and transection experiments validated the LH segmentation into two medial domains that derive from MZ699+ iPNs, and the LH-AL domain formed by vlPr neurons. In line with our observations are morphological studies on ePNs and third-order LH neurons revealing a similarly tight constriction into three zones within the LH [23], while single-cell labeling combined with image registration resulted in five ePN target zones [20]. However, the ePN terminal zones do not necessarily correspond to the target domains of iPNs, since it has recently been shown that MZ699+ iPNs do not inhibit odor responses of GH146+ ePNs [29] and that the presynaptic site of iPNs are spatially separated from those of ePNs [30]. Hence both PN populations represent

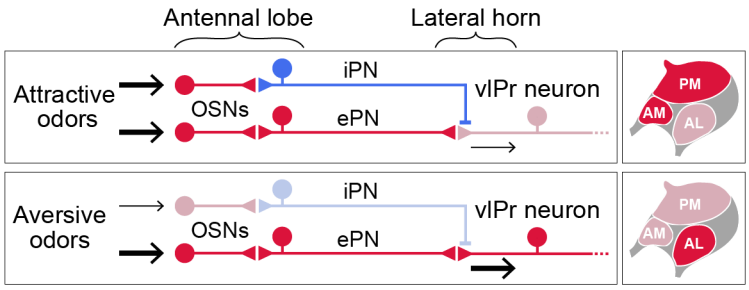

Figure 8: **Model of neural circuit encoding attractive and aversive odors.** Attractive odors activate both, iPNs and ePNs in the AL. iPNs suppress via feedforward inhibition the excitatory input from ePNs onto vlPr neurons. Hence, attractive odors activate mainly the LH-AM and LH-PN domains in the LH which derive from iPN activity. Aversive odors hardly activate iPNs, but ePNs. Since vlPr neurons are therefore not inhibited by iPNs, they will be activated by ePNs. The result is an activity of the LH-AL domain in the LH which reflects vlPr neuronal activity.

parallel processing pathways that most likely accomplish distinct processing tasks.

Silencing MB function revealed that the LH alone is sufficient for basic olfactory behavior [19,49,50]. Our behavioral results demonstrate that selectively silencing MZ699+ iPNs severely reduced the flies' odor attraction behavior. In addition, manipulated flies revealed an altered preference to different odor intensities. Hence our results suggest that MZ699+ iPNs are capable of extracting both features from the combinatorial code emerging in the AL. Interestingly, Parnas et al. [44] did not observe any general effect on odor preference when the synaptic transmission was blocked via shibire expression in MZ699-GAL4. However, since not only iPNs but also vlPr neurons are likewise impaired by this manipulation, the coding of both attractive as well as aversive odors was affected. A behavioral study revealed that silencing MBc neurons impairs odor attraction but not repulsion [51]. The authors drew the conclusion that the LH is involved in mediating innate repulsion rather than attraction. These results are not necessarily contradictory to ours since some ePNs might activate the LH-AL domain exclusively (i.e. vlPr neurons). On the other hand, Wang et al. [51] did not include highly concentrated attractive odors. Therefore it is possible that in their experiments, the odor detection threshold was simply reduced, so that only highly concentrated odors, which induced odor aversion, could be distinguished. Our behavioral results, in contrast, revealed the constant influence of the MZ699+ iPNs in mediating attraction for odorants over a range of concentrations.

Our data suggests that odors with opposing hedonic valences are encoded by an interplay of distinct processing pathways as summarized as a network model in Figure 8. The study by Liang et al. [29] showed that GABA release from MZ699+ iPNs directly inhibits responses of vlPr neurons to food odors as mentioned above. This finding fits well to our observations that iPNs are activated mainly by attractive odors while vlPr neurons are not, likely due to the inhibitory input from iPNs. VlPr neurons are, on the other hand, almost solely activated by repellent odors, which do hardly activate iPNs and therefore do not induce a strong inhibition to vlPr neurons. Repellent odors most likely activate vlPr neurons via ACh release of ePNs which is supported by our immunostainings with pre- and postsynaptic markers indicating that

vlPr neurons receive cholinergic input in the LH, while the vlPr represents their major output region (data not shown) [44]. The vlPr is supposedly also a target of visual neurons from the optic lobe [23] implying that a certain integration of different sensory modalities takes place at this central processing relay. Given that iPNs are inhibitory neurons, the underlying mechanism of odor attraction behavior might therefore be an inhibition of aversive neuronal circuits from the LH to the vlPr that are mainly composed of vlPr neurons. However, this assumption needs to be verified with further experiments elucidating if vlPr neurons are sufficient and necessary to mediate odor repellency.

Our study provides an important step in unraveling higher olfactory processing mechanisms that are crucial for mediating innate behaviors in *Drosophila*. We provide functional evidence for a feature-based spatial arrangement of the LH decoding opposing hedonic valences and odor intensity. The role of the LH as a center for integrating biological values towards innate decisions by computing conveyed information of two processing pathways is thus expanded.

4. Material and Methods

4.1. Drosophila stocks

All fly stocks were maintained on conventional cornmeal-agar-molasses medium under L:D 12:12, RH = 70% and 25°C. For wild-type controls *D. melanogaster* of the Canton-S strain was used. Transgenic lines were obtained from Bloomington Stock Center and Vienna RNAi stock center (http://www.vdrc.at). Other fly stocks were kindly provided by: Kei Ito (MZ699-GAL4), Stefan Sigrist (UAS-Dα7:mcherry), Hiromu Tanimoto (UAS-Syt:HA, UAS-mCD8:GFP) and Maria Luisa Vasconcelos (UAS-C3PA). The fly construct P[END1-2] (elav n-synaptobrevin-DsRed 1-2) was generated using a modified pCaST-elav-GAL4AD vector (plasmid 15307, addgene). The GAD domain present in the original vector was excised using NotI and FspAI enzymes; the FspAI recognition site was located within the DsRed coding sequence. A DNA oligonucleotide containing a modified n-synaptobrevin-coding ORF (n-syb) [52], upstream to a sequence identical to the excised DsRed-fragment, and a *Drosophila* Kozak site (caaaATG) and recognition sites for NotI and FspAI, were synthesized and inserted into the vector. The n-syb construct contains one silent mutation at position (C168T) to eliminate a FspAI-recognition site within the fragment. Excision, synthesis and ligation were performed by MWG Eurofins (Germany). The resulting plasmid was amplified in *E. coli* (One Shot®Top10 *E. coli*, Invitrogen) and purified using a Qiagen midi-prep kit (Qiagen). Embryo transformation to generate transgenic lines was performed by Aktogen (Cambridge, UK).

4.2. Immunohistochemistry

Whole-mount (wm) and vibratome (vt) immunofluorescence staining was carried out as described [11,53]. Initially brains were dissected in Ringer's solution (130 mM NaCl, 5 mM KCl, 2 mM $MgCl_2$, 2 mM $CaCl_2$, 36 mM saccharose, 5 mM HEPES, [pH 7.3]) [54] and fixed in 4% PFA in PBS-T (PBS, 0,2-1% Triton-X). After washing with PBS-T (wm) or PBS (vt) brains were blocked with PBS-T, 2% bovine serum albumin (BSA) or PBS-T, 5% normal goat serum

(NGS). Vt-sections were blocked using 5% NGS and 5% normal donkey serum (NDS). Primary antibodies were diluted in blocking solution or PBS-T and incubated at 4°C for 2-3 days (vt). Secondary antibody incubation lasted 1-2 days. Brains were mounted in VectaShield^{TM} (Vector Laboratories). The following primary antibodies were used: rabbit α-GABA (1:500) (Sigma), mouse α-GFP (1:500) or chicken α-GFP (1:1000) or rabbit α-GFP (1:500) (all Invitrogen), mouse monoclonal α-ChAT (1:500) (DSHB), mouse α-Nc82 (1:30) (DSHB) or rabbit α-Nc82 and guinea pig α-Nc82 (1:500), kindly provided by Stefan Sigrist, rabbit α-RFP (1:500) and mouse α-HA (1:1000) (both Abcam). The following secondary antibodies were used: Alexa Fluor® 488, goat anti-mouse IgG (1:500); Alexa Fluor® 488, goat anti-rabbit (1:500); Alexa Fluor® 546, goat anti-rabbit (1:500); Alexa Fluor® 633, goat anti-mouse (1:200), Fluor® 594 chicken anti mouse (1:200), Alexa Fluor® 488 donkey anti-chicken 1:200 (all IgG Invitrogen).

4.3. Functional imaging

Fly preparation and functional imaging of the AL was conducted as previously described [55,56]. LH imaging was conducted similarly, except for the higher resolution achieved with a 60x water immersion objective (LUMPlanFl 60x / 0.90 W, Zeiss). The optical plane was $\sim$30μm below the most dorsal entrance point of the iPN tract into the LH. Binning on the CCD-camera chip resulted in a resolution of 1 pixel = 0.4 x 0.4μm. For bilateral LH imaging during transection a 20x water immersion objective (NA 0.95, XLUM Plan FI, Olympus) was employed. All recordings lasted 10 s with a frame rate of 4 Hz. Odors included acids (propionic acid, acetic acid), lactones (-butyrolactone), terpenes (linalool), aromatics (acetophenone, methyl salicylate, benzaldehyde, phenylacetic acid), alcohols (1-octen-3-ol), esters (acetoin acetate, cis-vaccenyl acetate, 2-phenethyl acetate), ketones (2,3 butanedione) and balsamic vinegar diluted in mineral oil (all from Sigma Aldrich). Odors were applied during frame 814 (i.e. after 2 s, lasting for 2 s). Flies were imaged for up to one hour, with a minimum inter-stimulus interval of one minute. We selected conventional widefield Ca^{2+} imaging as the method of choice, since we were able to obtain single bouton resolution with this technique.

4.4. Imaging data analysis

Calcium imaging data of AL were analyzed with custom-written IDL software (ITT Visual Information Solutions) provided by Mathias Ditzen as previously described [55,56]. Regarding the Ca^{2+} imaging data in the LH, we repeated recordings of each odor at each concentration two to three times to ensure the reliability of the extracted domain information. To execute NNMF analysis (see below), at least 6-7 valid measurements, i.e. animals with repeated identical recordings, were collected for each odor and employed for the analysis. Individual odor measurements were aligned using ImageJ (Fiji) to correct movement artifacts. Fluorescence changes (ΔF/F) for each odor were calculated in relation to background fluorescence using frames 0-6 (i.e. 2- 0.5 s before odor application). A Gaussian low-pass filter (σ=1px) was applied to compensate for remaining movement artifacts and pixel noise. To reduce the computational load, the frame rate was averaged by two consecutive frames, and recordings were spatially down-sampled by a fac-

tor of two. The resulting concatenated time-series of the recordings is denoted as measurement matrix $\mathbf{Y}$ with element $\mathbf{Y}_{\mathrm{t,p}}$ being the t^{th} observed value of pixel p.

4.5. NNMF Non-Negative Matrix Factorization

In contrast to the AL, which consists of highly ordered glomerular subunits, the LH comprises a mainly homogenous neuropil which does not provide spatial or functional landmarks. Therefore, we used the automatic method NNMF to extract Ca^{2+} signals that exhibit common spatial or temporal features. NNMF, like other matrix factorization techniques (e.g. Principal Component Analysis (PCA) and Independent Component Analysis (ICA)), decompose the measurement matrix $\mathbf{Y}$ into k components, $\mathbf{Y} = \sum_k x_k \cdot a_k^T + \mathbf{R}$. The time-course a_k of each component contains a common underlying time-courses of all pixels and each pixel participation x_k declares how strongly each pixel is involved in this time-course. The residual matrix $\mathbf{R}$ contains the unexplained data. In order to perform NNMF, we implemented the HALS algorithm in Python including a spatial smoothness constraint ($\alpha_{sm} = 0.1$) [57] and an additional spatial decorrelation constraint ($\alpha_{de} = 0.1$) [58].

In PCA decomposition is performed such that either timecourses a_k or pixel participation x_k are uncorrelated, whereas ICA aims for timecourses (temporal ICA) or pixel participation (spatial ICA) to be independent. Although spatial ICA is able to segregate signals into functional similar neuropils [59], we chose the NNMF approach, because it is known to achieve even a better parts-based representation compared to the more holistic results of PCA or ICA [40]. In contrast to PCA and ICA, NNMF constrains both the extracted time-courses and pixel participations to be positive. Positive pixel participation enabled us to make a straightforward physiological interpretation, reading the participation values as the contribution strength of an underlying physiological domain. The restriction to positive time-courses reflects the fact that we did not observe any significant decrease of fluorescence in response to an odor in the original measurement data. For each animal we performed decomposition into k=5 components. This was sufficient to explain most of the data's variance (88% $\pm$ 8%, error is standard deviation across individuals). The remaining variance in the residual matrix $\mathbf{R}$ contained no additional domains but rather reflected remaining movement artifacts of the measurements (data not shown). Of the five components extracted by NNMF, three stood out prominently: First, they were extracted in all animals at very clearly defined anatomical positions. Second, their responses to stimuli repetitions were highly reproducible in contrast to the other two components, i.e. they exhibited a significant ($p < 2 \cdot 10^{-8}$, t-test) higher trial-to-trial correlation of 0.72 ± 0.20 in contrast to 0.52 ± 0.26 for the remaining components; and third, the odorant spectra of their responses were characteristic across animals.

Though we cannot completely rule out that the remaining components of the factorization are ORDs of their own, there are several indications that they are not. On the one hand, they exhibit a lower trial-to-trial correlation than the three selected components. Second, those components did not consistently appear at similar anatomical position. Instead of independent ORDs, these regions might convey fluorescence change independent of odor stimulation or an overlapping region of two of the reliable ORDs. A validation of our NNMF-based results

with spatial ICA yielded very similar, but slightly worse results. Whereas the three reliable ORDs from NNMF were also extracted in spatial ICA, the two remaining components exhibited much higher variability than when obtained with NNMF. Hence, we conclude that the LH area comprising MZ699+ neurons is made up of three ORDs. We labeled those three components according to the anatomical position of their pixel participation within the LH.

4.6. Statistical analysis of imaging data

To determine the coding properties of extracted odor response domains (ORDs), we calculated the mean response of each animal within a time window of 1-4 s after stimulus onset. Hence, median responses over all animals defined the standard stimulated response r^o_{ORD} of an ORD to an odor o. Initially, regions were evaluated individually, and correlations were calculated between standard response spectra and the behavioral response index (RI), or odor concentration, respectively, using the linregress function of the Python scipy.stat module. To analyze the combined ORD representations of odor patterns $p_o = (r^o_{\mathrm{PM}}, r^o_{\mathrm{AM}}, r^o_{\mathrm{AL}})$ we calculated for all odor pairs the pattern similarity as correlation distance $d_{o1,o2} = 1 - \mathrm{corr}(p_{o1}, p_{o2})$. In order to visualize the correlation matrix in a comprehensible way, we then arranged odors according to the single linkage clustering of the Python scipy.cluster.hierarchy module. To compare the representation in the LH to those of the AL, we applied the same procedure to the dorsal glomerular odor activation pattern.

4.7. 2-Photon photoactivation

For *in vivo* photoactivation experiments, 1-6 day old flies (Genotype: END1-2,UAS-C3PA;MZ699-GAL4) were dissected as in the imaging experiments except that tracts of the salivary glands were cut to prevent movement. Photoactivation was accomplished via continuous illumination with 760 nm for 15-25 min. After a 5-minute break to permit full diffusion of the photoconverted molecules, 925nm z-stacks of the whole brain were acquired and subsequently used for neuronal 3D-reconstruction. For all 3D reconstructions, the segmentation software AMIRA 5.3.3 (Mercury Computer Systems) was used. Neurons of different individuals were embedded into the reference brain using a labelfield registration as previously described [60]. Briefly, segmented labels of brain neuropils (AL, MBc, LH) were registered onto a reference brain image using affine registration followed by elastic warping. In a second step, the calculated transformation matrix was applied to the respective neuron morphology that was then aligned to the reference brain image.

4.8. 2-Photon-mediated transection

Transections of either the plF tract or the mACT were conducted in one brain hemisphere, each of the same fly. The target area was monitored with 925 nm and chosen to be close to the LH but distant enough not to affect neurites ramifying in the LH neuropil. For both tracts, lesioned areas had an average size of 34 μm and were illuminated with short pulses of 710 nm every 40 ms for 250 ms in 60 (plF) 80 (mACT) cycles in a single focal plane. After a fast z-stack with 925 nm to confirm complete lesion, a 5-minute neuronal recovery interval followed before continuing the imaging procedure. Data were analyzed using NNMF.

4.9. Image acquisition

Photoactivation and transection procedures as well as image acquisition following immunohistochemistry were accomplished with a 2-photon confocal laser scanning microscope (2PCLSM, Zeiss LSM 710 meta NLO) equipped with a 40x (W Plan-Apochromat 40x/1.0 DIC M27) or 20x (W N-Achroplan 20x/0.5 M27). The 2PCLSM was placed on a smart table UT2 (Newport Corporation, Irvine, CA, USA) and equipped with an infrared Chameleon Ultra^{TM} diode-pumped laser (Coherent, Santa Clara, CA, USA). Z-stacks were performed with argon 488 nm and helium-neon 543 nm laser or the Chameleon Laser 925 nm (BP500-550 for G-CaMP and LP555 for DsRed/Tomato) and had a resolution of 1024 or 512 square pixels. The maximum step size for immuno-preparations or single neuron projections was 1 μm and for AL reconstructions 2 μm.

4.10. Behavioral Assay

Flies carrying P[GAD1-RNAi];P[MZ699-GAL4] were crossed just before the experiment to prevent dosage compensation effects. T-maze experiments were performed as described [61]. WT, parental controls (P[GAD1-RNAi] or P[MZ699-GAL4]) and test flies carrying both insertions were tested separately under identical conditions. The response index (RI) was calculated as (O-C)/T, where O is the number of flies in the odor arm, C is the number of flies in the control arm, and T is the total number of flies used in the trial. Hence, the RI ranges from -1 (complete avoidance) to 1 (complete attraction). Each experiment was carried out on 30 flies and was repeated 12 times. RIs were compared with Dunn's Multiple Comparison or Dunn's Selected Pairs and tested against 0 (no response) by the Wilcoxon-rank-sum test.

Acknowledgments

We thank Silke Trautheim, Regina Stieber, Linda Gummlich and Sascha Bucks for excellent technical assistance, Stefan Sigrist for providing the Dα7:mcherry strain and antibodies and Emily Wheeler for editorial assistance.

Author contributions

A.S. and S.S. together conceived the study. A.S. planned all experiments, carried out functional imaging of iPNs, generated transgenic fly line and performed immunohistochemistry with help of J.R and A.B. V.G. performed functional imaging of OSNs and analyzed glomerular innervation patterns. A.B. performed PA-GFP experiments and neuronal reconstructions of iPNs. A.F. performed behavioral experiments. J.S. analyzed the imaging data using NNMF. M.K. supervised A.F. and M.S. supervised J.S. B.S.H. provided intellectual and financial support. A.S. and S.S. interpreted the results, prepared the figures and wrote the paper.

Funding

This work was supported by a BMBF grant (Federal Ministry of Research and Education) to S.S., A.S. and V.G. and the Max Planck Society. The funders have no role in study design, data collection and analysis, decision to publish, or preparation of the manuscript.

References

1. Manni E, Petrosini L (2004) A century of cerebellar somatotopy: a debated representation. Nat Rev Neurosci 5: 241-249.
2. Vosshall LB, Stocker RF (2007) Molecular Architecture of Smell and Taste in *Drosophila*. Annu Rev Neurosci 30: 505-533.
3. Sanes JR, Zipursky SL (2010) Design Principles of Insect and Vertebrate Visual Systems. Neuron 66: 15-36.
4. Heisenberg M (2003) Mushroom body memoir: from maps to models. Nat Rev Neurosci 4: 266-275.
5. Pasternak T, Greenlee MW (2005) Working memory in primate sensory systems. Nat Rev Neurosci 6: 97-107.
6. Bausenwein B, Dittrich AP, Fischbach KF (1992) The optic lobe of *Drosophila melanogaster*. II. Sorting of retinotopic pathways in the medulla. Cell and Tissue Research 267: 17-28.
7. Livingstone M, Hubel D (1988) Segregation of form, color, movement, and depth: anatomy, physiology, and perception. Science 240: 740-749.
8. Nassi JJ, Callaway EM (2009) Parallel processing strategies of the primate visual system. Nat Rev Neurosci 10: 360-372.
9. Hildebrand JG, Shepherd GM (1997) Mechanisms of olfactory discrimination: Converging evidence for common principles across phyla. Annual Review of Neuroscience 20: 595-631.
10. Axel R (1995) The molecular logic of smell. Sci Am 273: 154-159.
11. Vosshall LB, Wong AM, Axel R (2000) An olfactory sensory map in the fly brain. Cell 102: 147-159.
12. Wilson RI, Mainen ZF (2006) Early events in olfactory processing. Annu Rev Neurosci 29: 163-201.
13. Stocker RF, Heimbeck G, Gendre N, de Belle JS (1997) Neuroblast ablation in *Drosophila* P[GAL4] lines reveals origins of olfactory interneurons. J Neurobiol 32: 443-456.
14. Couto A, Alenius M, Dickson BJ (2005) Molecular, anatomical, and functional organization of the *Drosophila* olfactory system. Curr Biol 15: 1535-1547.
15. Fishilevich E, Vosshall LB (2005) Genetic and functional subdivision of the *Drosophila* antennal lobe. Curr Biol 15: 1548-1553.
16. Wang JW, Wong AM, Flores J, Vosshall LB, Axel R (2003) Two-photon calcium imaging reveals an odor-evoked map of activity in the fly brain. Cell 112: 271-282.
17. Fiala A, Spall T, Diegelmann S, Eisermann B, Sachse S, et al. (2002) Genetically expressed cameleon in *Drosophila melanogaster* is used to visualize olfactory information in projection neurons. Curr Biol 12: 1877-1884.
18. Caron SJC, Ruta V, Abbott LF, Axel R (2013) Random convergence of olfactory inputs in the *Drosophila* mushroom body. Nature 497: 113-117.
19. de Belle JS, Heisenberg M (1994) Associative odor learning in *Drosophila* abolished by chemical ablation of mushroom bodies. Science 263: 692-695.
20. Jefferis GSXE, Potter CJ, Chan AM, Marin EC, Rohlfing T, et al. (2007) Comprehensive Maps of *Drosophila* Higher Olfactory Centers: Spatially Segregated Fruit and Pheromone Representation. Cell 128: 1187-1203.
21. Marin EC, Jefferis GSXE, Komiyama T, Zhu H, Luo L (2002) Representation of the glomerular olfactory map in the *Drosophila* brain. Cell 109: 243-255.
22. Wong AM, Wang JW, Axel R (2002) Spatial representation of the glomerular map in the *Drosophila* protocerebrum. Cell 109: 229-241.
23. Tanaka NK, Awasaki T, Shimada T, Ito K (2004) Integration of chemosensory pathways in the *Drosophila* second-order olfactory centers. Curr Biol 14: 449-457.

24. Min S, Ai M, Shin SA, Suh GSB (2013) Dedicated olfactory neurons mediating attraction behavior to ammonia and amines in *Drosophila*. Proceedings of the National Academy of Sciences 110: E1321E1329.
25. Stocker RF, Lienhard MC, Borst A, Fischbach KF (1990) Neuronal architecture of the antennal lobe in *Drosophila melanogaster*. Cell Tissue Res 262: 9-34.
26. Ito K, Sass H, Urbach J, Hofbauer A, Schneuwly S (1997) GAL4-responsive UAS-tau as a tool for studying the anatomy and development of the *Drosophila* central nervous system. Cell and Tissue Research 290: 1-10.
27. Lai S-L, Awasaki T, Ito K, Lee T (2008) Clonal analysis of *Drosophila* antennal lobe neurons: diverse neuronal architectures in the lateral neuroblast lineage. Development 135: 2883-2893.
28. Okada R, Awasaki T, Ito K (2009) Gamma-aminobutyric acid (GABA)-mediated neural connections in the *Drosophila* antennal lobe. The Journal of Comparative Neurology 514: 74-91.
29. Liang L, Li Y, Potter CJ, Yizhar O, Deisseroth K, et al. (2013) GABAergic Projection Neurons Route Selective Olfactory Inputs to Specific Higher-Order Neurons. Neuron 79: 917-931.
30. Wang K, Gong J, Wang Q, Li H, Cheng Q, et al. (2014) Parallel pathways convey olfactory information with opposite polarities in *Drosophila*. Proceedings of the National Academy of Sciences 111: 3164-3169.
31. Fisek M, Wilson RI (2014) Stereotyped connectivity and computations in higher-order olfactory neurons. Nat Neurosci 17: 280-288.
32. Murthy M, Fiete I, Laurent G (2008) Testing Odor Response Stereotypy in the *Drosophila* Mushroom Body. Neuron 59: 1009-1023.
33. Wilson RI, Laurent G (2005) Role of GABAergic inhibition in shaping odor-evoked spatiotemporal patterns in the *Drosophila* antennal lobe. J Neurosci 25: 9069-9079.
34. Shang Y, Claridge-Chang A, Sjulson L, Pypaert M, Miesenbck G (2007) Excitatory local circuits and their implications for olfactory processing in the fly antennal lobe. Cell 128: 601-612.
35. Tian L, Hires SA, Mao T, Huber D, Chiappe ME, et al. (2009) Imaging neural activity in worms, flies and mice with improved GCaMP calcium indicators. Nat Meth 6: 875-881.
36. Nakai J, Ohkura M, Imoto K (2001) A high signal-to-noise Ca(2+) probe composed of a single green fluorescent protein. Nat Biotechnol 19: 137-141.
37. Keene AC, Stratmann M, Keller A, Perrat PN, Vosshall LB, et al. (2004) Diverse odor-conditioned memories require uniquely timed dorsal paired medial neuron output. Neuron 44: 521-533.
38. Magee RJ, Kosaric N (1987) The Microbial Production of 2,3-Butanediol. Advances in Applied Microbiology 32: 89-161.
39. Semmelhack JL, Wang JW (2009) Select *Drosophila* glomeruli mediate innate olfactory attraction and aversion. Nature 459: 218-223.
40. Lee DD, Seung HS (1999) Learning the parts of objects by non-negative matrix factorization. Nature 401: 788-791.
41. Datta SR, Vasconcelos ML, Ruta V, Luo S, Wong A, et al. (2008) The *Drosophila* pheromone cVA activates a sexually dimorphic neural circuit. Nature 452: 473-477.
42. Patterson GH, Lippincott-Schwartz J (2002) A photoactivatable GFP for selective photolabeling of proteins and cells. Science 297: 1873-1877.
43. Ruta V, Datta SR, Vasconcelos ML, Freeland J, Looger LL, et al. (2010) A dimorphic pheromone circuit in *Drosophila* from sensory input to descending output. Nature 468: 686-690.
44. Parnas M, Lin Andrew C, Huetteroth W, Miesenbck G (2013) Odor Discrimination in *Drosophila*: From Neural Population Codes to Behavior. Neuron 79: 932-944.
45. Tully T, Quinn WG (1985) Classical conditioning and retention in normal and mutant *Drosophila melanogaster*. J Comp Physiol [A] 157: 263-277.
46. Chakraborty TS, Goswami SP, Siddiqi O (2009) Sensory Correlates of Imaginal Conditioning in *Drosophila melanogaster*. Journal of Neurogenetics 23: 210-219.
47. Larsson MC, Domingos AI, Jones WD, Chiappe ME, Amrein H, et al. (2004) Or83b encodes a broadly expressed odorant receptor essential for *Drosophila* olfaction. Neuron 43: 703-714.

48. Knaden M, Strutz A, Ahsan J, Sachse S, Hansson BS (2012) Spatial Representation of Odorant Valence in an Insect Brain. Cell Reports 1: 392-399.
49. Heimbeck G, Bugnon V, Gendre N, Keller A, Stocker RF (2001) A central neural circuit for experience-independent olfactory and courtship behavior in *Drosophila melanogaster*. Proceedings of the National Academy of Sciences 98: 15336-15341.
50. Connolly JB, Roberts IJ, Armstrong JD, Kaiser K, Forte M, et al. (1996) Associative learning disrupted by impaired Gs signaling in *Drosophila* mushroom bodies. Science 274: 2104-2107.
51. Wang Y, Chiang AS, Xia S, Kitamoto T, Tully T, et al. (2003) Blockade of neurotransmission in *Drosophila* mushroom bodies impairs odor attraction, but not repulsion. Curr Biol 13: 1900-1904.
52. DiAntonio A, Burgess RW, Chin AC, Deitcher DL, Scheller RH, et al. (1993) Identification and characterization of *Drosophila* genes for synaptic vesicle proteins. J Neurosci 13: 4924-4935.
53. Laissue PP, Reiter C, Hiesinger PR, Halter S, Fischbach KF, et al. (1999) Three-dimensional reconstruction of the antennal lobe in *Drosophila melanogaster*. J Comp Neurol 405: 543-552.
54. Estes PS, Roos J, van der Bliek A, Kelly RB, Krishnan KS, et al. (1996) Traffic of Dynamin within Individual *Drosophila* Synaptic Boutons Relative to Compartment-Specific Markers. The Journal of Neuroscience 16: 5443-5456.
55. Stkl J, Strutz A, Dafni A, Svatos A, Doubsky J, et al. (2010) A Deceptive Pollination System Targeting Drosophilids through Olfactory Mimicry of Yeast. Curr Biol 20: 1846-1852.
56. Strutz A, Voeller T, Riemensperger T, Fiala A, Sachse S (2012) Calcium Imaging of Neural Activity in the Olfactory System of *Drosophila*. In: Martin J-R, editor. Genetically Encoded Functional Indicators. New York, NY, USA: Springer Science+Business Media, LLC. pp. 43-70.
57. Cichocki A, Phan A (2009) Fast local algorithms for large scale nonnegative matrix and tensor factorizations. IEICE TRANSACTIONS on Fundamentals of Electronics, Communications and Computer Sciences E92-A: 1-14.
58. Chen Z, Cichocki A (2005) Nonnegative matrix factorization with temporal smoothness and/or spatial decorrelation constraints. Signal Processing.
59. Reidl J, Starke J, Omer DB, Grinvald A, Spors H (2007) Independent component analysis of high-resolution imaging data identifies distinct functional domains. NeuroImage 34: 94-108.
60. Rybak J, Kuss A, Hans L, Zachow S, Hege H-C, et al. (2010) The digital bee brain: integrating and managing neurons in a common 3D reference system. Frontiers in Systems Neuroscience 4.
61. Stensmyr MC, Dweck HKM, Farhan A, Ibba I, Strutz A, et al. (2012) A Conserved Dedicated Olfactory Circuit for Detecting Harmful Microbes in *Drosophila*. Cell 151: 1345-1357.

Supplemental material

Supplemental figure S1

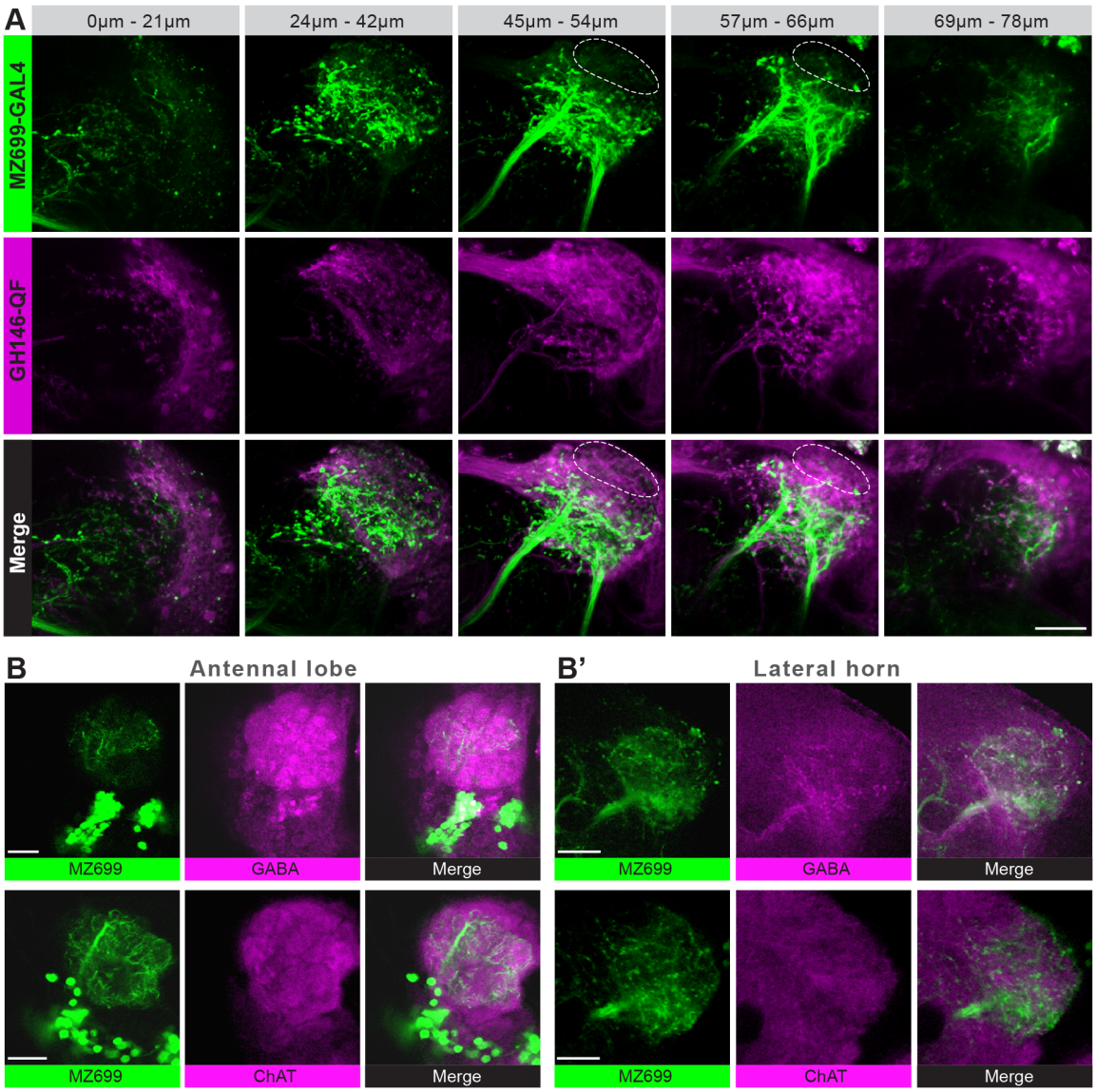

Characterization of excitatory and inhibitory projection neurons. (A) Overlap of ePNs (QUAS-Tomato) and iPNs (UAS-GCaMP3.0) in the LH area. The circle indicates the posterior lateral region, which is sparsely innervated by iPNs and dominated by ePN axonal terminal fields. (B) GABA vs. ChAT Immuno in the AL and LH (B). Somata and LH neurites of MZ699 iPNs are GABA-positive and ACh-negative. Scale bar, 20μm.

Supplemental figure S2

A *In vivo* double labelings

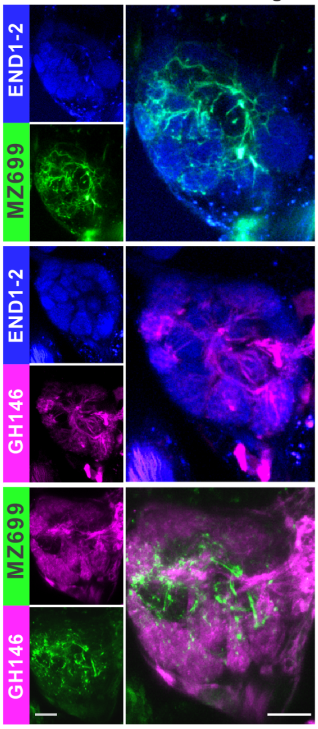

B

Glomerulus	MZ699	GH146	Merge
"column"			
"arm"			
D			X
DA1			X
DA2			X
DA3			X
DA4l			X
DA4m			
DC1			X
DC2			X
DC3			X
DC4			
DL1			
DL2d			
DL2v			
DL3			
DL4			X
DL5			
DM1			
DM2			X
DM3			X
DM4			X
DM5			X
DM6			X
DP1l			
DP1m			X
V			
VA1d			X
VA1v			X
VA2			X
VA3			X
VA4			
VA5			X
VA6			X
VA7l			X
VA7m			X
VC1			X
VC2			
VC3			
VC4			
VC5			
VL1			
VL2p			
VL2a			X
VM1			
VM2			X
VM3			X
VM4			
VM5d			
VM5v			
VM6			
VM7			X
1			X
53	**40**	**37**	**29**
	75.47 %	**69.81 %**	**54.72 %**

Glomerular innervations of ePNs an iPNs. (A) Representative in vivo images of glomerular innervations. MZ699 and GH146 lines have been reconstructed with END1-2 background (two upper planes) and dual labeling via the Q-system and the GAL4-UAS expression system (lowest plane). Scale bar, 20 m. (B) Detailed glomerular AL innervation. Green filled cells indicate innervation by MZ699-GAL4, magenta GH146-GAL4 innervation, respectively and grey, no innervation by the indicated line. Bottom rows, total number of innervated glomeruli with percentage share indicated below. Merge column: white filled with x indicates glomeruli innervated by both lines, grey only one line. Blue filled rows are glomeruli labeled by none of the enhancer trap lines.

Supplemental figure S3

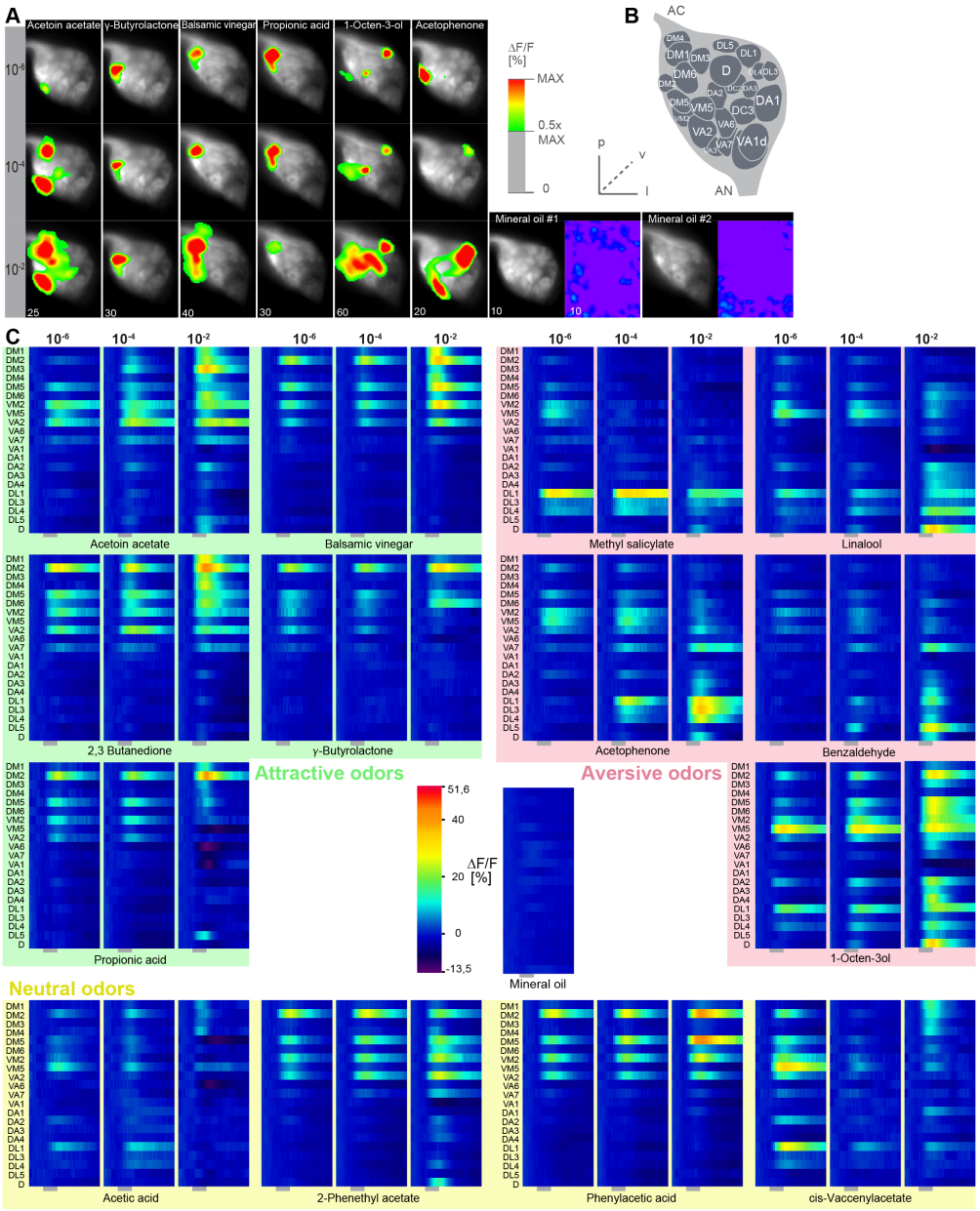

Calcium responses of OSNs. (A) Representative glomerular Ca2+-responses of OSNs for a subset of odorants at three concentrations. Scale bar to the right. Control (mineral oil) recordings are shown additionally as full false-color coded images. (B) Glomerular AL atlas used for glomerular identification. (C) Median Ca2+-activity traces of all glomeruli for all odorants at the three indicated concentrations. Scale bar and control measurement in the center. Odor application is indicated by the grey bar below the heatmaps (n=6-7).

Supplemental table S1

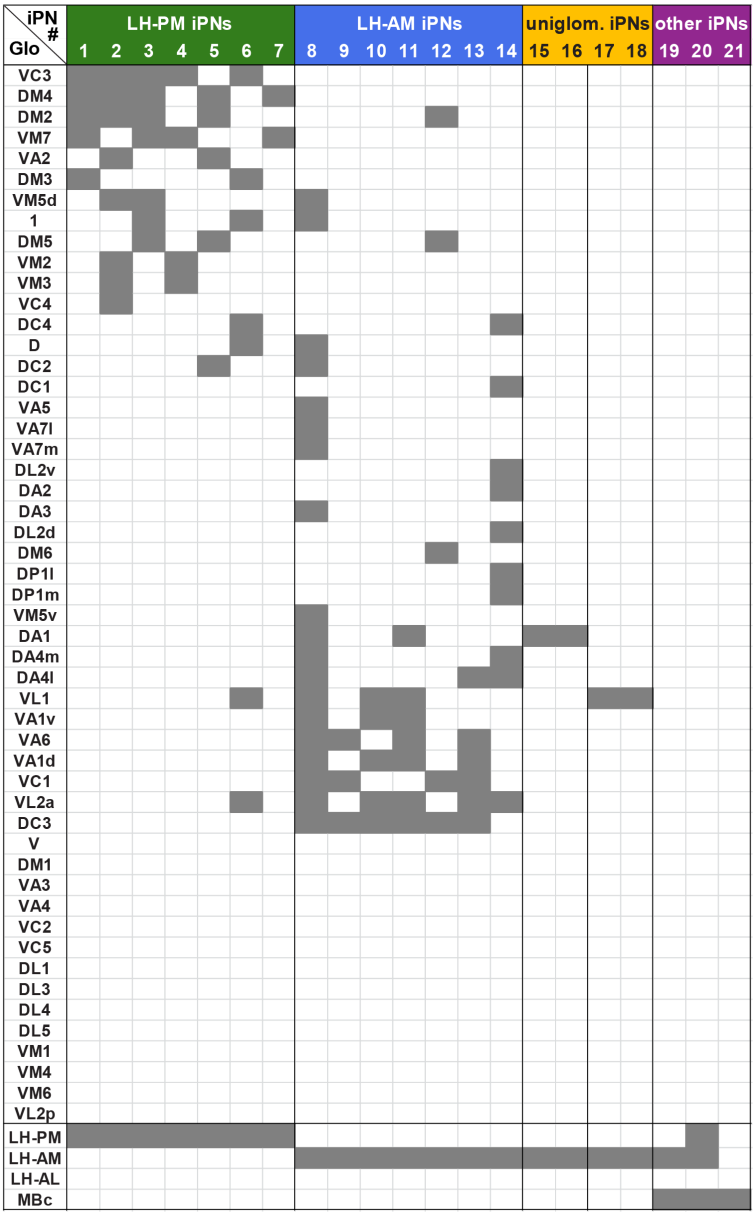

Calcium responses of OSNs. (A) Representative glomerular Ca2+-responses of OSNs for a subset of odorants at three concentrations. Scale bar to the right. Control (mineral oil) recordings are shown additionally as full false-color coded images. (B) Glomerular AL atlas used for glomerular identification. (C) Median Ca2+-activity traces of all glomeruli for all odorants at the three indicated concentrations. Scale bar and control measurement in the center. Odor application is indicated by the grey bar below the heatmaps (n=6-7).

General discussion

6.1 Summary

From an anatomical point of view, the olfactory systems of both mice and *Drosophila* show a clear topographic structure. In both species the olfactory relay center (Olfactory Bulb and Antennal Lobe, respectively) allocates the receptor activation on a stereotypical sensory map. This map is the substrate of local circuits in higher olfactory centres and, especially in mice, for lateral and centrifugal modulation within the relay center itself. Despite this clear anatomical structure, any underlying functional organization of this topography remains vague.

Therefore this thesis elaborates on this topic. First two techniques have been introduced which facilitate this investigation: For one the extraction of functional units in neuronal imaging data by regularized non-negative matrix factorization (rNMF) in chapter 2. And second the characterization of olfactory receptive fields by physico-chemical models in chapter 3. In chapter 4 these methods are utilized to gain additional evidence for the hypothesis that glomeruli in the mouse olfactory relay center (OB) are mainly arranged according to their tuning similarity, i.e. their receptive field overlap. And chapter five demonstrates, again utilizing the power of rNMF to extract functional domains, that a topographic read-out of the *Drosophila* olfactory relay center (AL) results in a map of innate valence in a higher olfacory center, the Lateral Horn.

6.2 Computational methods

6.2.1 Segmentation of imaging data

Functional Imaging is a commonly used technique to study neural ensembles [Grienberger and Konnerth, 2012; Pain et al., 2011]. It allows for simultaneous recording of neural activity within the full ensemble. In general one can analyse the recorded images as a whole, e.g. by calculating pixel-wise correlations between response patterns [Roussel et al., 2014]. But disaggregating them into functional components yields insights into individual contributions to the ensemble representation.

In this thesis I introduced rNMF as a general tool to obtain such a disaggregation. It purely relies on the functional data and thus does not require any additional anatomical knowledge. Therefore rNMF proved to be useful in extracting glomeruli from IOS recordings. Even though

in general anatomical outlines of glomeruli can be obtained, this information is not present in IOS recordings and it would therefore require substantially more experimental effort to acquire them (see also chapter 2). In contrast, in Calcium Imaging of the LH anatomical information is already present via the resting fluorescence. But in this case the neuropil does not show a clear anatomical compartmentalization per se, which could only be revealed via rNMF disaggregation or tracing studies.

6.2.2 Physico-chemical receptive fields

Given the enormous number of possible odorous molecules [Ruddigkeit et al., 2014] it is intractable to obtain the full listing of all odour responses for olfactory receptors. Here physico-chemical receptive field models offer a loophole as they provide a quantitative relation between molecular properties and receptor activation. First of all, assuming high accuracy, they allow to reliably interpolate unobserved odour responses. But even with low accuracy they prove to be useful as their predictions generate measurement suggestions which are in general much more informative than arbitrary chosen stimuli [Boyle et al., 2013]. Such a procedure of hypothesis driven stimulus choice is generally known as adaptive stimulus sampling and an upcoming technique in investigating receptive fields [Benda et al., 2007; DiMattina and Zhang, 2013].

In this thesis physico-chemical activation models have been derived both for *Drosophila* receptors as well as for the mouse MOR18-2 glomerulus. In both cases it was shown that the models exhibit predictive power for unmeasured odours, but still are too imprecise to be considered as high accuracy models. In case of *Drosophila* receptors a final measurement of the model predictions showed that in best cases about 40-50% of the response spectrum variance had been already anticipated by the models. Unfortunately in case of the MOR18-2 glomerulus a final biological validation of model prediction is still missing, but bootstrap validation indicated that also in this case about 40% of the response spectrum variance has been anticipated by the model.

Interestingly, augmentation of the commonly used physico-chemical eDragon descriptors [Haddad et al., 2008] by additional vibrational mode descriptors (EVA) [Ferguson et al., 1997] did not increase predictive power of the models for the *Drosophila* receptors, although this was the case for the MOR18-2 glomerulus. A simple explanation could be that the assessed molecules in the *Drosophila* study show a large variety in terms of chemical composition, whereas the enriched measurement set of MOR18-2 is heavily biased towards its most prominent ligands, namely short esters. Thus, in case of MOR18-2 a much more accurate outline of the physico-chemical receptive field was necessary. This was possibly enhanced by the EVA descriptors. On the other hand the different performance of descriptor sets could also indicate that *Drosophila* and mice receptors differ in how molecular properties are converted into neural activity. To this end it would be interesting to obtain physico-chemical activation models for both species with a very similar measurement set. But it also has to be mentioned that ligand based models in general do not offer mechanistic explanations for biological activations. They only describe which odours are similar to a receptor, but not why. This is also the reason that this study

neither supports nor denies any hypothesis on the heavily disputed mechanism of olfactory receptor activation [Hettinger, 2011].

6.3 Olfactory neural maps

6.3.1 Olfactory relay centres

This research provides further evidence that in the olfactory relay center of mice (OB) nearby glomeruli form tunotopic clusters, i.e. they exhibit overlapping molecular response spectra [Ma et al., 2012; Matsumoto et al., 2010]. A similar tendency is observed in the olfactory relay center of *Drosophila* (AL) [Galizia et al., 2010]. But currently this interpretation is based on fragmentary knowledge of individual receptive ranges or, as in the case of this research, with extended knowledge of the receptive range of only a single glomerulus. In the end a definite affirmation of the tunotopic hypothesis will only be obtained if the receptive fields of many glomeruli are sufficient well known.

Nonetheless the tunotopic hypothesis seems to be quite plausible. Many theoretical models for the emergence of sensory feature maps are derived from the general principle that neurons which 'fire together wire together' [Buonomano and Merzenich, 1998]. Thus in olfaction this principle seems to be modified to 'glomeruli which fire together cluster together'. And indeed, at least in mice, neural activity of the sensory neurons is inevitable in order to obtain the topographic map [Imai et al., 2010].

Regarding this hypothesis one could even speculate that the glomerular arrangement does not only reflect the overlap of mono-molecular response spectra but rather the overall co-activation probability of the response spectra in natural odour blends. Eventually shared ligands would be a major fraction to glomerular co-activation, but also different odours with a common emitter would add to the glomerular co-activation and therefore shape the topographic lay-out. For example, such an observation has been recently made in the accessory olfactory bulb, where glomeuli are clustered predominantly with respect to of their source (i.e. juvenile/adult male/female urine) [Hammen et al., 2014].

6.3.2 Secondary olfactory centres

The topography of the olfactory relay centres (OB/AL) is in particular conserved in areas associated with internal valence evaluation (amygdala respectively LH) (see Introduction).

This study (chapter 5) demonstrated that in *Drosophila* the topographic projection results in a compartmentalization of the LH with respect to the received olfactory information from PNs of the mlALT. Such a compartmentalization of olfactory information transfer is also observed in the PNs of other tracts, with the response profiles of different areas being associated to attractive or aversive innate behaviour [Min et al., 2013] or a more general behavioural context (e.g. feeding vs. mating behaviour) [Jefferis et al., 2007; Grosjean et al., 2011]. Furthermore for *Drosophila* larvae it was shown that a circuit of the LH mediates feeding behaviour in response to appetitive odours [Wang et al., 2013]. Taken together this indicates that the LH

might evaluate the external context and provides a switchboard for different innate behaviours [Galizia, 2014].

This hypothesis neatly connects to the hypothesis that olfactory relay centres are arranged according to co-occurrence probability of response spectra in the natural environment. Such an arrangement eventually means that glomeruli which are responsive in the same environmental context are grouped together. Thus a topographic aggregation of stimulus responses, as seen in the projections to the LH, would represent the combined evidence for distinct environmental contexts.

This thesis does not investigate the role of topography in the secondary olfactory centres associated with learning (PC respectively MBc). In fact other research shows that in there the topography of the olfactory relay centres does not directly governs the response patterns of third order neurons [Caron et al., 2013; Bekkers and Suzuki, 2013]. Nonetheless also these centres might be influenced by a tunotopic layout of olfacory relay centres as a result of lateral inhibition. In general it is supposed that a major role of lateral inhibition in sensory coding is the transformation of previously statistically dependent receptive fields to an efficient independent representation optimized for pattern recognition [Schwartz and Simoncelli, 2001]. This mechanism is also discussed for olfactory systems [Luo et al., 2010; Giridhar et al., 2011] but with the limitation that there is so far negligible knowledge on natural odour statistics.

6.4 Conclusion and outlook

As typical for science this thesis rather raises new questions than giving final answers. But it also contributes to the refinement of two computational methods which may empower future research on those topics: rNMF for a reliable and automatic extraction of functional modules in neuroimaging and physico-chemical activation models for a better assessment olfactory receptive fields.

Based on accumulated evidence on olfactory topography, this thesis results in a final hypothesis to be further investigated: Glomerular arrangement reflects the environmental statistics of odour occurrence and thus builds a substrate for both an effective environmental context evaluation and an efficient representation of environmental regularities for pattern recognition.

References

John M Bekkers and Norimitsu Suzuki. Neurons and circuits for odor processing in the piriform cortex. *Trends in neurosciences*, 36(7):429–438, 2013.

Jan Benda, Tim Gollisch, Christian K Machens, and Andreas VM Herz. From response to stimulus: adaptive sampling in sensory physiology. *Current opinion in neurobiology*, 17(4):430–436, 2007.

Sean Michael Boyle, Shane McInally, and Anandasankar Ray. Expanding the olfactory code by in silico decoding of odor-receptor chemical space. *Elife*, 2, 2013.

Dean V Buonomano and Michael M Merzenich. Cortical plasticity: from synapses to maps. *Annual review of neuroscience*, 21(1):149–186, 1998.

Sophie JC Caron, Vanessa Ruta, LF Abbott, and Richard Axel. Random convergence of olfactory inputs in the drosophila mushroom body. *Nature*, 497(7447):113–117, 2013.

Christopher DiMattina and Kechen Zhang. Adaptive stimulus optimization for sensory systems neuroscience. *Frontiers in neural circuits*, 7, 2013.

Allan M. Ferguson, T Heritage, P Jonathon, SE Pack, L Phillips, J Rogan, and PJ Snaith. Eva: A new theoretically based molecular descriptor for use in qsar/qspr analysis. *Journal of computer-aided molecular design*, 11(2):143–152, 1997.

C Giovanni Galizia. Olfactory coding in the insect brain: data and conjectures. *European Journal of Neuroscience*, 39(11):1784–1795, 2014.

C Giovanni Galizia, Daniel Münch, Martin Strauch, Anja Nissler, and Shouwen Ma. Integrating heterogeneous odor response data into a common response model: a door to the complete olfactome. *Chemical senses*, 35(7): 551–563, 2010.

Sonya Giridhar, Brent Doiron, and Nathaniel N Urban. Timescale-dependent shaping of correlation by olfactory bulb lateral inhibition. *Proceedings of the National Academy of Sciences*, 108(14):5843–5848, 2011.

Christine Grienberger and Arthur Konnerth. Imaging calcium in neurons. *Neuron*, 73(5):862–885, 2012.

Yael Grosjean, Raphael Rytz, Jean-Pierre Farine, Liliane Abuin, Jérôme Cortot, Gregory SXE Jefferis, and Richard Benton. An olfactory receptor for food-derived odours promotes male courtship in drosophila. *Nature*, 478(7368):236–240, 2011.

Rafi Haddad, Rehan Khan, Yuji K Takahashi, Kensaku Mori, David Harel, and Noam Sobel. A metric for odorant comparison. *Nature methods*, 5(5):425–429, 2008.

Gary F Hammen, Diwakar Turaga, Timothy E Holy, and Julian P Meeks. Functional organization of glomerular maps in the mouse accessory olfactory bulb. *Nature neuroscience*, 2014.

Thomas P Hettinger. Olfaction is a chemical sense, not a spectral sense. *Proceedings of the National Academy of Sciences*, 108(31):E349–E349, 2011.

Takeshi Imai, Hitoshi Sakano, and Leslie B Vosshall. Topographic mapping—the olfactory system. *Cold Spring Harbor perspectives in biology*, 2(8):a001776, 2010.

Gregory SXE Jefferis, Christopher J Potter, Alexander M Chan, Elizabeth C Marin, Torsten Rohlfing, Calvin R Maurer Jr, and Liqun Luo. Comprehensive maps of¡ i¿ drosophila¡/i¿ higher olfactory centers: Spatially segregated fruit and pheromone representation. *Cell*, 128(6):1187–1203, 2007.

Sean X Luo, Richard Axel, and LF Abbott. Generating sparse and selective third-order responses in the olfactory system of the fly. *Proceedings of the National Academy of Sciences*, 107(23):10713–10718, 2010.

Limei Ma, Qiang Qiu, Stephen Gradwohl, Aaron Scott, Q Yu Elden, Richard Alexander, Winfried Wiegraebe, and C Ron Yu. Distributed representation of chemical features and tunotopic organization of glomeruli in the mouse olfactory bulb. *Proceedings of the National Academy of Sciences*, 109(14):5481–5486, 2012.

Hideyuki Matsumoto, Ko Kobayakawa, Reiko Kobayakawa, Takuya Tashiro, Kenji Mori, Hitoshi Sakano, and Kensaku Mori. Spatial arrangement of glomerular molecular-feature clusters in the odorant-receptor class domains of the mouse olfactory bulb. *Journal of neurophysiology*, 103(6):3490–3500, 2010.

Soohong Min, Minrong Ai, Seul A Shin, and Greg SB Suh. Dedicated olfactory neurons mediating attraction behavior to ammonia and amines in drosophila. *Proceedings of the National Academy of Sciences*, 110(14): E1321–E1329, 2013.

F Pain, B L'heureux, and H Gurden. Visualizing odor representation in the brain: a review of imaging techniques for the mapping of sensory activity in the olfactory glomeruli. *Cellular and Molecular Life Sciences*, 68(16): 2689–2709, 2011.

Edith Roussel, Julie Carcaud, Maud Combe, Martin Giurfa, and Jean-Christophe Sandoz. Olfactory coding in the honeybee lateral horn. *Current Biology*, 24(5):561–567, 2014.

Lars Ruddigkeit, Mahendra Awale, and Jean-Louis Reymond. Expanding the fragrance chemical space for virtual screening. *Journal of cheminformatics*, 6(1):27, 2014.

Odelia Schwartz and Eero P Simoncelli. Natural signal statistics and sensory gain control. *Nature neuroscience*, 4(8):819–825, 2001.

Yonghua Wang, Yuhan Pu, and Ping Shen. Neuropeptide-gated perception of appetitive olfactory inputs in¡ i¿ drosophila¡/i¿ larvae. *Cell reports*, 3(3):820–830, 2013.